AD NUMBER:	AD0883047

LIMITATION CHANGES

TO:

Approved for public release; distribution is unlimited.

FROM:

Thia document is subject to special export controls; 16 Feb 1971, and each transmittal to foreign goverments or foreign nationals may be made only with prior approval of Naval Ordnance Laboratory, White Oak, MD, 20910.

AUTHORITY

ST-A NOL LTR, 15 NOV 1971

2

NOLTR 71-27

SHOCK INTERACTION SURFACE PRESSURES FOR HEMISPHERICAL AND CONICAL BODIES

By
Frank P. Baltakis

16 FEBRUARY 1971

NOL

NAVAL ORDNANCE LABORATORY, WHITE OAK, SILVER SPRING, MARYLAND 20910

ATTENTION

This document is subject to special export controls and each transmittal to foreign governments or foreign nationals may be made only with prior approval of NOL.

NOLTR 71-27

118

SHOCK INTERACTION SURFACE PRESSURES FOR HEMISPHERICAL AND CONICAL BODIES

Prepared by:
Frank P. Baltakis

ABSTRACT: Transient pressures, induced by wind-tunnel simulated head-on blast wave interactions, have been measured on a hemisphere and on cones of 9-, 15- and 30-degree semivertex angles. Blast wave Mach numbers of 1.6 to 2.2, 2.2 to 5.85 and 2.7 to 4.4 were simulated at the free-stream Mach numbers of 3.1, 5.1 and 7, respectively. Measured pressure-time histories for the hemisphere were compared and found in agreement with histories predicted by McNamara's FLAME code. Peak overpressures for the cones were found to be in agreement with values predicted by a simple theoretical method in which an assumption is made that the blast wave forms a Mach stem moving along the surface at a velocity whose axial component equals the velocity of the main blast wave. The effects of angle of attack and of nose blunting were also investigated with the nine-degree cone at a free-stream Mach number of 5.1.

NAVAL ORDNANCE LABORATORY
WHITE OAK, MARYLAND

NOLTR 71-27

16 February 1971

SHOCK INTERACTION SURFACE PRESSURES FOR HEMISPHERICAL AND CONICAL BODIES

This study was conducted to provide experimental shock interaction data required in development of re-entry vehicles. Funding for this study was provided by the Defense Atomic Support Agency under Task Number NOL 814/DASA (DASA MIPR 528-67 and 504-68).

The contributions of Mary E. Falusi, who performed numerical computations for the hemisphere, are gratefully acknowledged.

GEORGE G. BALL
Captain, USN
Commander

Leon H. Schindel
LEON H. SCHINDEL
By direction

CONTENTS

TABLES

ILLUSTRATIONS

ILLUSTRATIONS (Cont'd)

ILLUSTRATIONS (Cont'd)

BLANK PAGE

INTRODUCTION

Shock interaction studies were undertaken in anticipation that large magnitude, shock-induced pressures might occur on the surface of a re-entry vehicle. Such pressures were considered potentially detrimental to the guidance system and to the structural integrity of the vehicle. Reference (1) contains a thorough review of the analytical methods of the shock-on-shock interaction studies. The numerical techniques which evolved subsequently are reviewed in Reference (2). Experimental data, suitable for a quantitative verification of the analytical methods, were not previously available. Difficulties in environmental simulation and in instrumentation have severely limited the experimental studies both in scope and in quality of the obtainable data.

This report describes an experimental study of pressures induced by head-on blast wave interactions on hemispherical and conical bodies. The objective of the study was to provide experimental data of peak overpressures on cones of different vertex angles and detailed pressure-time histories on the surface of a hemisphere. Environmental simulation, encompassing free-stream Mach numbers of 3, 5 and 7 at blast wave Mach numbers ranging from 1.6 to 5.8 (see Table 1 for the test matrix), was achieved in a wind-tunnel-shocktube facility.

SYMBOLS

M_1	free-stream Mach number
M_s	blast wave Mach number
P	model surface pressure
$P_{initial}$, P_i	model surface pressure prior to shock interaction
P_p	shock interaction induced peak pressure
α	angle of incidence, degrees
θ_c	cone semivertex angle, degrees
ϕ	peripheral (or model roll) angle, degrees

TEST APPARATUS

TEST FLOW CONDITIONS

Tests were performed in the Naval Ordnance Laboratory's Supersonic Tunnel No. 1. This tunnel operates on air which is drawn in at the atmospheric pressure and temperature and is discharged into a 52-foot-diameter vacuum sphere. For this experiment the tunnel was fitted with three conical nozzles, a matched diffuser and a shocktube. The shocktube (a 1.5-inch I.D. by 12-foot-long steel tube) was installed in the settling chamber and aligned coaxially with the nozzles. The discharge end of the driven tube was positioned about four inches upstream of the main nozzle throat and was always open. The driver section contained air or helium. Pressure differential was provided by aluminum diaphragms, ranging from 0.02 to 0.07 inch in thickness. To facilitate reloading of the shocktube, the diaphragm section was positioned outside of the tunnel reservoir by making a 70-degree bend over a 34-inch radius into the driven section. Figure 1 illustrates the test setup schematically.

Free-stream flow conditions, to which the models were exposed prior to blast wave impingement, are given in Table 2. The table lists Mach number values at the nozzle exit and, since the nozzles were conical, the measured axial Mach number gradients for the test section. The air supply pressure and temperature for all three nozzles were 14.6 psia and 70°F (±5°F). The air dew temperature ranged from -25°F to -50°F.

Table 3 lists the preblast surface pressure coefficients for the test models. For the hemisphere and for the 15- and 30-degree cones these coefficients were obtained from References (4) and (5), respectively. For the nine-degree cone at various angles of attack the pressure coefficients were determined experimentally at the free-stream conditions of the shock interaction tests.

Flow quality behind the blast wave was of particular interest and was investigated analytically and experimentally. In theory, the flow parameters depend on the nozzle geometry and the intensity of the blast wave. Figure A-1-A (Appendix), for example, shows the calculated pressure and Mach number variations for the Mach 5 nozzle of this experiment. It shows that for the blast wave intensities of this study ($M_s \leq 6$) the static pressure decreases at a rate of less than one percent per microsecond. The indicated decrease rate for the flow Mach number is less than 1/10 percent per microsecond. (The method of Ref. (6) was used for these calculations.)

Calibration measurements indicated that at low intensities ($M_s \leq 2$) the Pitot and the static pressures were essentially constant. At higher intensities the pressures decreased with time approximately as predicted theoretically. Figure A-1-B illustrates typical calibration traces taken with a small (0.13-inch diameter) Pitot probe. (The initial peak on the photographs is due to the blast wave interaction with the bow wave of the Pitot probe.) Calibration shadowgraphs showed that, at certain flow conditions, secondary waves were close behind or were coalescing with the main wave in the test region. The presence of such disturbances could be detected also on the pressure-time traces. These traces, together with the shadowgraphs, were used to screen out the test runs with disturbances close to the main blast wave. The effects of wave curvature (some curvature occurred at higher wave intensities) were minimized by placing the instrumentation close to the tunnel centerline. Additional data on the wind-tunnel - shocktube facility and its calibration may be found in Reference (3).

TEST MODELS

The test models included a hemisphere and three cones of 9-, 15- and 30-degree semivertex angles. The 9-degree cone was provided with two removable nose tips; one sharp and one spherically blunted to a 3/16-inch radius. All the models were machined of brass and had a smooth surface finish. Use of small diameter transducers and some transducer contouring after installation assured good surface continuity at the transducer ports. A photograph of the models is shown in Figure 2. Figure 3 shows model geometry and transducer port location data. Flow conditions and attitudes at which each model was tested are given in Table 1.

INSTRUMENTATION

Pressure transducers used in this experiment were developed and produced at NOL. A small (0.093-inch diameter by 0.06-inch thick) crystal was utilized in these transducers to achieve a highly localized measurement and a response time of less than one microsecond. The crystal was supported on an acoustically matched slender rod to ensure a measuring period length of approximately 20 microseconds. Figure A-2 (Appendix) illustrates the transducer design; Figure A-3 shows typical calibration traces under the reflected and the incident shock calibration conditions. Additional transducer design and performance information may be found in Reference (7).

Optical measurements were made with a two-spark shadowgraph system. This system provided shock wave patterns as well as wave velocity data. As shown in Figure 1 the sparks for photography were generated by two pairs of electrodes located along a common optical axis. The light from the sparks was reflected from a parabolic mirror through the test section onto a large (11 x 14 in.) photographic plate where the wave patterns were recorded. A phototube and a time interval meter (Berkeley counter with a 1/10-microsecond count) were used to measure the time interval between the two sparks.

TEST RESULTS AND ANALYSIS

CONES

PRESSURE DATA. Cone tests were concerned primarily with the peak values of the shock-interaction-induced surface overpressures. These overpressures were measured at the surface stations as indicated in Figure 3 and are tabulated as peak-to-preblast steady-state ratios in Tables 4 to 8. Variation of the measured pressure versus different parameters is illustrated on Figures 4 to 9.

In Tables 4 to 8 the ratios are listed versus blast wave Mach number with the run number included for reference. In some instances the same run number is repeated, indicating that the overpressure was measured with more than one transducer simultaneously. The spatial locations of these transducers were not significantly different, as may be seen in Figure 3.

The peak overpressures were obtained from pressure-time traces recorded with Polaroid cameras. Typical examples of these traces are given in the Appendix on Figures A-4 to A-8 for cones and on Figure A-9 for the hemisphere. On Figure 4 some of the traces are replotted to scale. The traces on Figure 4 show that the peak value occurs with a delay which varies with the cone angle and with the blast wave intensity. As discussed in the Instrumentation section, the transducer sensing element was of 0.093-inch diameter, introducing a possible delay of about 2.3 microseconds at $M_s = 2$ and about 1.8 microseconds at $M_s = 4$ ($M_1 = 5$, $\theta_c = 9$-degree configuration). As indicated by the traces, the delay at low shock intensities is approximately two microseconds. At higher shock intensities this delay is considerable longer for the 9- and 15-degree cones. The traces also show that the pressure rise for the 9- and 15-degree cones is not continuous but is interrupted by a step. Both the step and the additional delay are conjectured to be caused by the blast wave interaction with the boundary layer. (Such interactions tend to cause a bifurcation of the shock wave and the resultant two-step type pressure rise.)

The traces also suggest that the finite rise time, coupled with the steep decrease in pressure immediately following the peak value, may cause the indicated peak pressure to be lower than actually experienced by the model. For the 9-degree and the 15-degree cones, for which the peaks are only moderately steep (and most of the delay is due to the boundary-layer effects) this difference is negligible. For the 30-degree cone the difference may be as high as 20 percent. No satisfactory method was available for this correction and the data are presented as measured.

The peak overpressure values for the 9-, 15- and 30-degree cones are shown plotted on Figure 5. Included on this figure are also the theoretically predicted values. The theoretical calculations were based on an earlier observation in the ballistics-range experiments (Ref. (8)) which indicated that the blast wave reflects at the surface as a Mach wave and that the stem of this wave travels at the velocity the axial component of which is virtually the same as the velocity of the main blast wave. For the 9-degree and the 15-degree cones this observation is confirmed by the optical data of this experiment and the correlation of the measured and calculated pressure peaks is good. For the 30-degree cone the optical data (which will be discussed later) show a regular rather than a Mach-type reflection. Nevertheless, the values computed by this method are in fair agreement with the experimental data.

On Figure 6 the data of Figure 5 have been crossplotted to illustrate the effect of the cone angle. The values corresponding to the zero-cone-angle points are pressure ratios across a normal shock of the indicated intensity.

Free-stream Mach number effects were investigated with the 9-degree cone at Mach number values of 3.1, 5.1 and 7. The results are listed in Table 4 and also plotted on Figures 5D and 5E. Figure 5D shows that at Mach 3.1 the pressures are slightly higher than predicted theoretically (optical observations also indicated that the Mach stem was advancing a little faster than the main blast wave). At Mach 7 (Fig. 5E) the measured pressures are slightly lower than predicted. Theoretical curves plotted on Figure 5E show the peak-to-preblast pressure ratio to decrease slightly with increasing free-stream Mach number.

The effects of nose blunting were investigated with the 9-degree cone at a free-stream Mach number of 5.1. The cone was blunted spherically to a 3/8-inch radius and the pressures were measured over a distance ranging from 3 to 6 nose radii downstream from the tip. The peak pressures, given in Table 7 and also in Figure 7, were found to be virtually the same as for the sharp cone. Pressure variations with time were found to be slightly different as may be seen by comparing Figures A-4B and A-5A of the Appendix.

The effects of angle of incidence were studied with the 9-degree cone at a free-stream Mach number of 5.1. Measurements were obtained on the windward, the 90-degree and the leeward surfaces at angles of incidence of 10 and 20 degrees and on the windward and the 90-degree surfaces at the 30-degree angle of incidence. The results are presented in Table 8 and also in Figure 8. The "predicted" variation curve on Figures 8A, 8B and 8C is the theoretical curve for a cone whose semivertex angle is equal to the test cone semivertex angle plus the angle of incidence. This curve is included for a qualitative comparison rather than for correlation.

In Figure 9 the values of Figure 8 are crossplotted to illustrate the variation with the incidence angle. The nonmonotonic pressure variation versus angle of incidence, indicated for the windward surface by Figure 9, is somewhat unexpected. However, a similar trend is also indicated by Figure 6 for pressure variation versus cone angle.

SHADOWGRAPHS. Shadowgraphs in this study provided two types of information: (1) shock interaction wave patterns, and (2) data for the blast wave intensity determination. In addition, shadowgraphs were also used for detecting nonuniformities in the flow behind the blast wave.

Photographs on Figure 10 illustrate shock interaction patterns for the 30-degree cone. These photographs were taken with a two-spark shadowgraph system (Fig. 1) and show the shock interaction wave pattern superimposed on the preblast flow field. The principal waves for this cone are quite distinct. The blast wave is refracted as it enters the model shock envelope and it forms a regular reflection (not a Mach reflection) at the surface. The model wave is refracted toward the surface. A contact surface formed at the blast wave - model shock wave interaction point is visible (although not very distinctly) as is the second reflection of the blast wave (reflection from the new model shock wave). On photograph A the boundary layer at the point of reflection seems virtually undisturbed, while on photograph B, because of a higher blast wave intensity, a thickening of the boundary layer occurs.

Photographs on Figure 11 show shock interaction patterns for the 15-degree cone. The blast wave is refracted as it enters the shock region but near the surface it forms a Mach stem. Interaction of the Mach wave with the boundary layer is clearly visible on photograph B. The model shock wave at a low shock intensity ($M_s = 2.4$, photograph A) is refracted towards the surface; at a higher shock intensity ($M_s = 3.8$, photograph B) it is virtually in line with the preblast wave until it coalesces with the reflected blast wave after which it bulges out away from the surface. Similar wave patterns may be recognized on Figure 12 for the 9-degree cone. However, because of low air density in the shock region the details are not very distinct. Additional shadowgraphs, for the majority of the pressure data runs, are given in the Appendix on Figures A-10 through A-18.

HEMISPHERE

PRESSURE DATA. Pressure measurements on the surface of a hemisphere were made at free-stream Mach numbers of 3.1 and 5.1. The blast wave Mach number range at the free-stream Mach number of 5.1 was 2.2 to 5.85. At Mach 3.1 this range was considerably narrower (1.68 to 1.88) because of the flow nonuniformities which were present close behind the blast wave at the higher wave intensities. Pressure measurements were made at the stagnation point and also at the 45-degree and the 90-degree points; however, because of lower pressures at the 45-degree and 90-degree points, spark interference and mechanical vibrations prevented obtaining data at these points for some of the test runs. The data, in the form of ratios of measured to the preblast surface pressure at the respective point, are presented in Figures 13 to 16. Typical Polaroid photographs of the pressure-time traces are given in the Appendix on Figure A-9.

On Figure 13 pressure-time variations are shown for the three model surface stations for various flow conditions. The variations are detailed reproductions of the original pressure-time traces recorded with the Polaroid cameras. These traces (and the traces on Fig. A-9) may contain some effects of transducer ringing and flow nonuniformities. Transducer ringing effects may be recognized, e.g., on the stagnation point traces. The ringing frequency is about one megacycle per second and the amplitude on Figures 13C and 13D is about ±4 percent of the total output. On Figures 13A, 13B and 13E, this amplitude in only about ±2 percent. Flow nonuniformities generally are of two types: discrete shocks and gradual deviations. Discrete shocks can be detected on flow shadowgraphs and the runs containing such disturbances close behind the blast wave were rejected. To detect gradual deviations, a small-diameter, fast-response Pitot probe was used. This probe, located in the test flow about three inches from the model centerline, monitored the

Pitot pressure of the flow behind the blast wave. Based on these measurements, the influence of gradual deviations on pressure data for the hemisphere tests is estimated to be less than 1/2 percent per microsecond for the duration of the overpressure at the stagnation point. (Typical Pitot probe traces may be seen in the Appendix on Figure A-1-B.)

The zero time on Figure 13 refers to the start of the pressure rise at the particular station. The pressure rise time of about 1/2 microsecond for the stagnation point is due to the transducer response characteristics. The rise time of about two microseconds for the 45-degree and the 90-degree stations is due primarily to the shock wave passage time across the face of the pressure transducer (0.093 inch, Fig. A-2).

Comparisons of measured and numerically predicted pressure-time histories are shown on Figures 14 to 16. The numerical histories were computed for a variety of flow conditions using McNamara's FLAME code (Ref. (9)). On Figure 14G an additional comparison with Taylor's PASS code prediction (Ref. (10)) is also included. The zero time on Figures 14 to 16 refers to the start of the measured overpressure; the computed history is shifted on the time scale to give the best overall agreement.

The stagnation point histories (Fig. 14) are in good overall agreement. The difference, which is the largest during the initial stages of interaction, is partly due to a slower predicted pressure-rise rate and partly due to a lower pressure magnitude predicted for the initial stages of the interaction as may be seen by comparing, for example, Figures 14A, 14E and 14H. The difference in pressure magnitude tends to increase with increasing blast wave intensity, and it is conjectured to be caused by the real gas effects which were not accounted for in the computations. The slower pressure-rise rate apparently is due to the spread of the discontinuities, which is a characteristic of the FLAME code. (The code uses a floating mesh which permits the model bow wave and the contact surface to be treated as discontinuities but it allows the blast wave to spread over a few mesh widths.)

At the 45-degree station (Fig. 15) the overall pressure magnitude is in good agreement, however, the numerically predicted pressure-rise and pressure-decay rates are considerably lower than measured experimentally. At the 90-degree station (Fig. 16) this difference is more pronounced particularly at the lower free-stream Mach number ($M_1 = 3.1$).

SHADOWGRAPHS. Figure 17 shows shadow photographs of the wave patterns at different stages of interaction. These photographs were taken with a two-spark system, with the first spark discharging prior to the interaction. Photograph A shows the interaction at an early stage. The blast wave is refracted in the model shock region and at the surface it forms a regular reflection. The reflected blast wave, in the model stagnation region, is moving upstream and is about halfway between the model surface and the new bow wave. Photograph B shows the wave pattern at a later stage of interaction. The reflection point is about 70 degrees from the stagnation point and the reflected blast wave has collided and reflected from the new bow wave. On photograph C the reflection point is over the cylindrical part of the model and the reflection mode has changed from the regular to the Mach-type reflection.

Detailed correlation of the events indicated by the shadow photographs and the pressure traces were not intended in this experiment. For a qualitative illustration of the interaction wave patterns at various flow conditions, photographs for most of the pressure data runs are given in the Appendix on Figure A-19.

CONCLUSIONS

Transient pressures induced by a head-on blast wave have been measured on a hemisphere and on cones of 9-, 15- and 30-degree semivertex angles. Flow conditions included free-stream Mach numbers of 3.1, 5.1 and 7 and the blast wave Mach numbers of 1.6 to 2.2, 2.2 to 5.85 and 2.7 to 4.4 at the free-stream Mach numbers of 3.1, 5.1 and 7, respectively. The effects of angle of attack and of nose blunting were also investigated with the 9-degree cone at a free-stream Mach number of 5.1.

Pressure-time histories at the stagnation point of the hemisphere were found to agree with histories predicted by the McNamara FLAME code to within about 15 percent. At the 45-degree and the 90-degree stations the pressure-rise rates predicted by the code were considerably lower than measured experimentally.

The measured peak overpressures for cones were found to agree well with values predicted by a simple theoretical method. This method is based on the assumption that the blast wave forms a Mach stem which moves along the surface at the velocity the axial component of which is equal to the velocity of the main blast wave.

Shock-induced overpressures for cones were found to be virtually nonexistent at low blast wave intensities ($M_s < 2$). At a blast wave Mach number of 4 the overpressure for the 9-degree cone was found to be about 10 percent and for the 30-degree cone about 40 percent of the new steady-state pressure. Because of the finite transducer diameter, the measured peak pressures for the 30-degree cone represent values which at the higher blast wave intensities ($M_s \geq 4$) may be as much as 20 percent too low.

Variation of the peak pressure with cone angle, when this pressure is expressed as a ratio to the preblast surface pressure, was found to be small.

Spherical blunting of the 9-degree cone was found to have no significant effect on the pressure magnitude at the flow conditions investigated ($M_1 = 5$, $M_s = 4$).

REFERENCES

Moran, J. P. and Ritter, A., "A Critical Survey of Shock-on-Shock Interaction Theory," Picatinny Arsenal, Technical Memorandum 1753, Oct 1965
Merritt, D. L., Williams, J. and Dawson, P., "Shock Interaction Handbook," NOL Technical Report to be published
Baltakis, F. P., Merritt, D. L. and Aronson, P. M., "Two Techniques for Simulating the Interaction of a Supersonic Vehicle with a Blast Wave," NOLTR 67-154 Oct 1967
Elliott, D. M., "Pressure Distributions on Sphere-Cones," Sandia SC-RR-64-1796, Jan 1965
Ames Research Staff, "Equations, Tables, and Charts for Compressible Flow," NACA Report 1135, 1953
Mirels, H. and Mullen, J. F., "Aerodynamic Blast Simulation in Hypersonic Tunnels," AIAA Journal, Vol 3, pp 2103-8, Nov 1965
Baltakis, F. P., "Development of a Fast-Response Pressure Transducer," NOLTR 69-158, Oct 1969
Merritt, D. L. and Aronson, P. M., "Experimental Studies of Shock-Shock Interactions on a 9° Cone," NOLTR 67-182, Jan 1968
McNamara, W., "Axisymmetric Interaction of a Blast Wave with the Shock Layer of a High-Speed Blunt Body," Massachusetts Institute of Technology, BSD TR 66-280 (ASRL TR 121-15), Feb 1966
Hudgins, H. E., Jr., "A Correlation of Pressure, Duration and Impulse Due to the Shock Interaction Transient on Supersonic Vehicles," Picatinny Arsenal, Technical Report 3474 (AMC 66-14), Feb 1967

Table 1

TEST CONFIGURATIONS

Model	Nose Shape	Angle of Incidence	Free-Stream Mach Number	Blast Wave Mach Number
9° Cone	Sharp	0	3.1	1.6 to 2.2
		0	7.0	2.7 to 4.4
		0	5.1	2.2 to 5.4
		10°	5.1	4.09 to 4.35
		20°	5.1	3.89 to 4.45
		30°	5.1	4.16 to 4.51
	Spherical	0	5.1	3.9 to 4.5
15° Cone	Sharp	0	5.1	2.4 to 4.9
30° Cone	Sharp	0	5.1	1.7 to 5.0
Hemisphere		0	3.1	1.68 to 1.88
		0	5.1	2.2 to 5.85

Table 2

NOZZLE GEOMETRY AND FLOW CHARACTERISTICS DATA

Mach Number (at nozzle exit)	Axial Mach Number Gradient (per inch)	Exit Diameter (inches)	Throat Diameter (inches)	Length (inches)	Reynolds Number (10^6 per foot)
3.05	0.025	9.25	4.12	60	2.20
5.03	0.029	12.5	2.27	60	0.89
6.92	0.050	12.5	1.30	60	0.47

Table 3

PREBLAST SURFACE PRESSURE DATA

Model	Nose Shape	Angle of Incidence	Station	Free-Stream Mach Number	Pressure Coefficient
9° Cone	Sharp	0		3.1	0.073
		0		7.0	0.057
		0		5.1	0.062
	Spherical	0		5.1	0.062
	Sharp	10	Windward	5.1	0.210
		10	90-Degree	5.1	0.048
		10	Leeward	5.1	0.019
		20	Windward	5.1	0.446
		20	90-Degree	5.1	0.058
		20	Leeward	5.1	-0.059
		30	Windward	5.1	0.745
		30	90-Degree	5.1	0.079
15° Cone	Sharp	0		5.1	0.153
30° Cone	Sharp	0		5.1	0.528
Hemisphere		0	Stagnation Pt.	3.1	1.760
		0	Stagnation Pt.	5.1	1.810
		0	45° Point	3.1	0.839
		0	45° Point	5.1	0.840
		0	90° Point	3.1	-0.017
		0	90° Point	5.1	0.031

Table 4

SHOCK-INDUCED PEAK-TO-PREBLAST PRESSURE RATIOS ON THE SURFACE OF A 9-DEGREE CONE

M_s	M_1	P_p/P_i	Run No.
2.21	5.03	5.67	277
2.25	5.05	5.39	178
2.28	5.03	5.95	276
2.32	5.03	5.34	236
2.34	5.03	5.34	237
2.48	5.00	6.40	418
2.62	5.00	6.68	421
3.67	5.05	15.6	719
3.80	5.06	16.4	718
3.81	5.05	16.0	721
3.88	5.05	16.1	723
3.91	5.05	17.2	727
3.97	5.03	16.4	280
4.08	5.05	17.9	725
4.32	5.06	19.4	736
4.59	5.06	21.4	737
4.62	5.00	22.4	432
4.76	5.03	22.4	287
4.99	5.03	24.9	283
5.37	5.05	31.6	190

M_s	M_1	P_p/P_i	Run No.
1.59	3.10	3.95	225
1.61	3.10	3.91	224
1.64	3.10	4.07	152
1.66	3.10	3.95	223
1.67	3.10	4.02	153
1.70	3.10	3.98	150
1.73	3.12	4.35	788
1.77	3.12	4.50	787
1.77	3.10	4.12	151
1.77	3.12	4.06	785
1.78	3.12	4.35	786
2.07	3.12	5.79	783
2.14	3.12	5.67	782
2.14	3.12	5.81	784
2.65	7.00	6.85	384
2.86	↓	7.75	399
2.93		8.32	383
3.03		8.02	381
3.05		8.32	376
3.43		10.4	382
4.20		14.2	379
4.40		17.1	378

Table 5

SHOCK-INDUCED PEAK-TO-PREBLAST PRESSURE RATIOS ON THE SURFACE OF A 15-DEGREE CONE

M_s	M_1	P_p/P_i	Run
2.40	5.07	5.89	332
2.42	5.07	6.11	349
2.42	5.07	6.25	350
2.44	5.07	6.34	333
3.80	5.07	14.4	337
3.92	5.07	15.2	338
3.97	5.07	14.8	342
4.33	5.07	19.7	346
4.43	5.12	20.5	771
4.44	5.08	19.9	343
4.45	5.12	20.6	772
4.48	5.08	19.7	669
4.49	5.07	20.7	345
4.64	5.12	21.4	770
4.70	5.12	21.9	773
4.81	5.12	22.2	768
4.84	5.08	21.1	672

Table 6

SHOCK-INDUCED PEAK-TO-PREBLAST PRESSURE RATIOS ON THE SURFACE OF A 30-DEGREE CONE

M_s	M_1	P_p/P_1	Run
1.70	5.07	4.25	358
1.97	5.07	5.08	363
2.20	5.07	6.15	359
3.77	5.07	16.7	367
3.86	5.08	16.5	656
3.87	5.07	18.5	372
3.96	5.12	18.3	776
3.97	5.07	16.4	366
4.02	5.07	18.3	370
4.03	5.08	17.3	651
4.11	5.08	17.3	678
4.14	5.08	18.5	650
4.20	5.12	20.8	775
4.27	5.08	18.3	667
4.58	5.12	22.7	778
4.64	5.08	19.9	659
4.78	5.08	21.4	679
4.82	5.08	21.5	657
4.89	5.08	22.6	661
5.00	5.08	24.2	663

Table 7

SHOCK-INDUCED PEAK-TO-PREBLAST PRESSURE RATIOS ON THE SURFACE OF A 9-DEGREE, SPHERICALLY BLUNTED CONE

M_s	M_1	P_p/P_i	Run
3.88	5.10	16.6	730
3.88	5.12	17.2	730
3.88	5.13	16.1	730
3.88	5.14	17.6	730
3.94	5.10	17.3	738
3.94	5.12	16.3	738
3.94	5.13	17.2	738
3.94	5.14	17.3	738
3.98	5.10	17.1	731
3.98	5.12	16.7	731
3.98	5.14	17.4	731
4.25	5.12	18.5	739
4.25	5.13	18.1	739
4.25	5.14	17.4	739
4.50	5.10	19.6	766
4.50	5.13	19.6	766
4.50	5.14	20.2	766

Table 8

SHOCK-INDUCED PEAK-TO-PREBLAST PRESSURE RATIOS ON THE SURFACE OF A 9-DEGREE CONE AT ANGLES OF ATTACK

α	ϕ	M_s	M_1	P_p/P_i	Run
10	0	4.09	5.10	19.3	740
		4.09	5.11	18.4	740
		4.22	5.10	20.9	744
		4.22	5.11	19.6	744
		4.27	5.10	19.6	741
		4.27	5.11	18.5	741
		4.30	5.10	20.7	743
		4.30	5.11	20.5	743
		4.34	5.10	20.4	742
		4.34	5.11	18.6	742
	90	4.09	5.12	22.8	740
		4.09	5.13	22.2	740
		4.14	5.12	21.8	760
		4.22	5.12	21.3	744
		4.22	5.13	21.6	744
		4.27	5.12	22.6	741
		4.27	5.13	22.2	741
		4.30	5.12	23.9	743
		4.30	5.13	22.6	743
		4.34	5.12	23.4	742
		4.34	5.13	22.6	742
	180	4.14	5.12	16.3	760
		4.14	5.13	15.5	760
		4.35	5.12	17.2	759
		4.35	5.13	16.4	759
20	0	4.16	5.11	23.0	749
		4.16	5.12	22.5	749
		4.19	5.11	25.8	748
		4.19	5.12	24.3	748
		4.21	5.11	24.9	761
		4.21	5.12	26.4	761
		4.26	5.11	24.7	763
		4.26	5.12	24.1	763
		4.37	5.11	25.5	747
		4.37	5.12	24.6	747

Table 8 (Cont.)

α	ϕ	M_s	M_1	P_p/P_1	Run
20	0	4.39	5.11	26.4	746
		4.39	5.12	24.9	746
		4.39	5.11	27.1	762
		4.39	5.12	27.6	762
		4.45	5.11	25.4	745
		4.45	5.12	25.9	745
	90	4.16	5.11	21.3	749
		4.16	5.12	21.7	749
		4.18	5.11	21.7	748
		4.18	5.12	21.6	748
		4.37	5.11	22.3	747
		4.37	5.12	21.9	747
		4.39	5.11	23.5	746
		4.39	5.12	22.5	746
		4.45	5.11	22.8	745
		4.45	5.12	22.5	745
	180	3.89	5.11	13.1	755
		3.96	5.11	13.6	754
		4.18	5.11	14.1	757
		4.25	5.11	15.0	756
30	0	4.16	5.10	23.3	750
		4.16	5.12	21.8	750
		4.40	5.12	24.1	751
		4.50	5.10	25.1	753
		4.50	5.12	25.4	753
		4.51	5.10	24.1	752
		4.51	5.12	23.3	752
	90	4.16	5.10	21.5	750
		4.16	5.12	20.4	750
		4.40	5.10	21.7	751
		4.40	5.12	20.9	751
		4.50	5.10	21.3	753
		4.50	5.12	20.2	753
		4.51	5.10	21.8	752
		4.51	5.12	21.0	752

α - Angle of Incidence
ϕ - 0 - Windward Surface
ϕ - 90 - 90-Degree Surface
ϕ - 180 - Leeward Surface

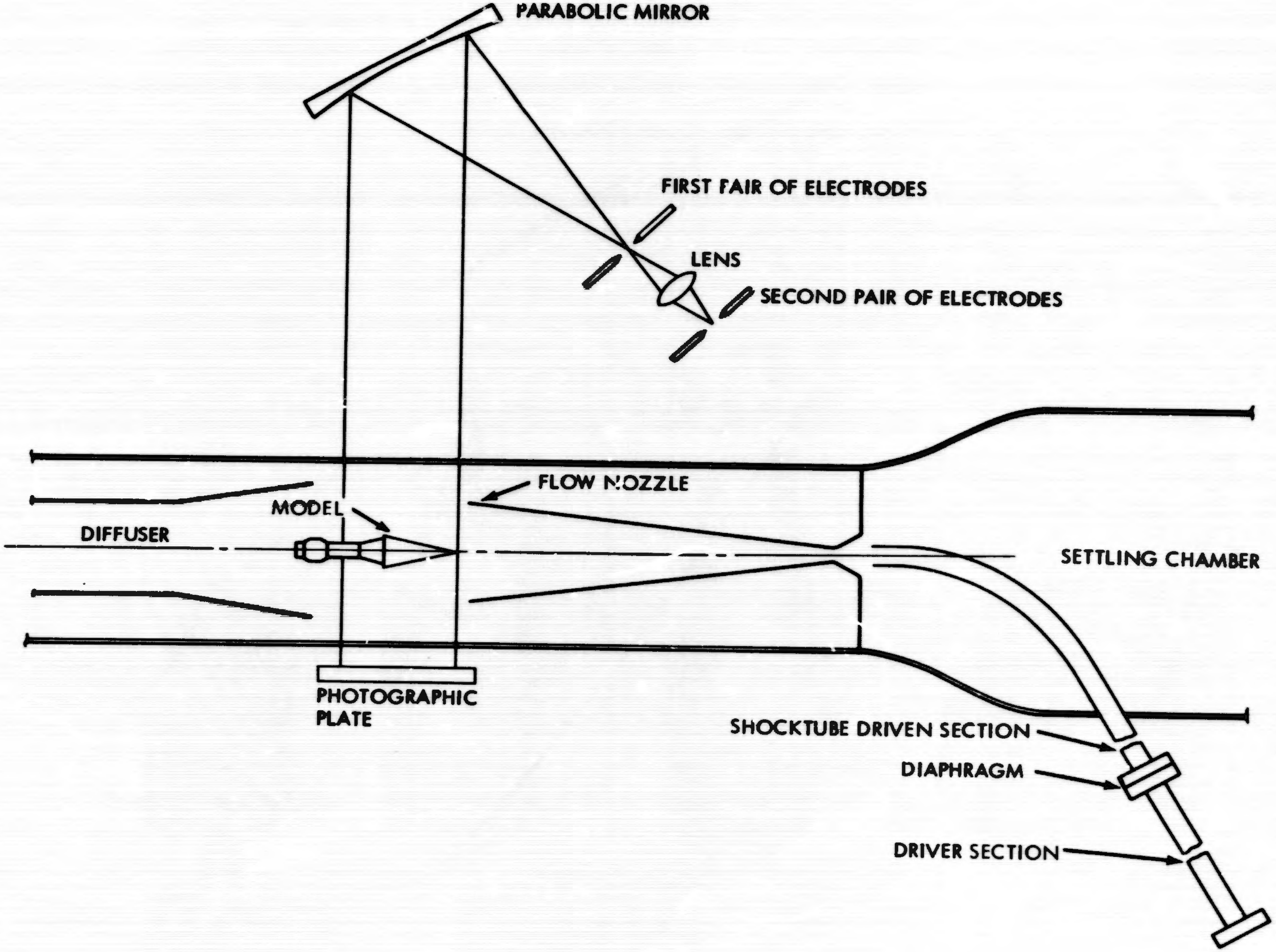

FIG. 1 SCHEMATIC ILLUSTRATION OF THE TEST SETUP

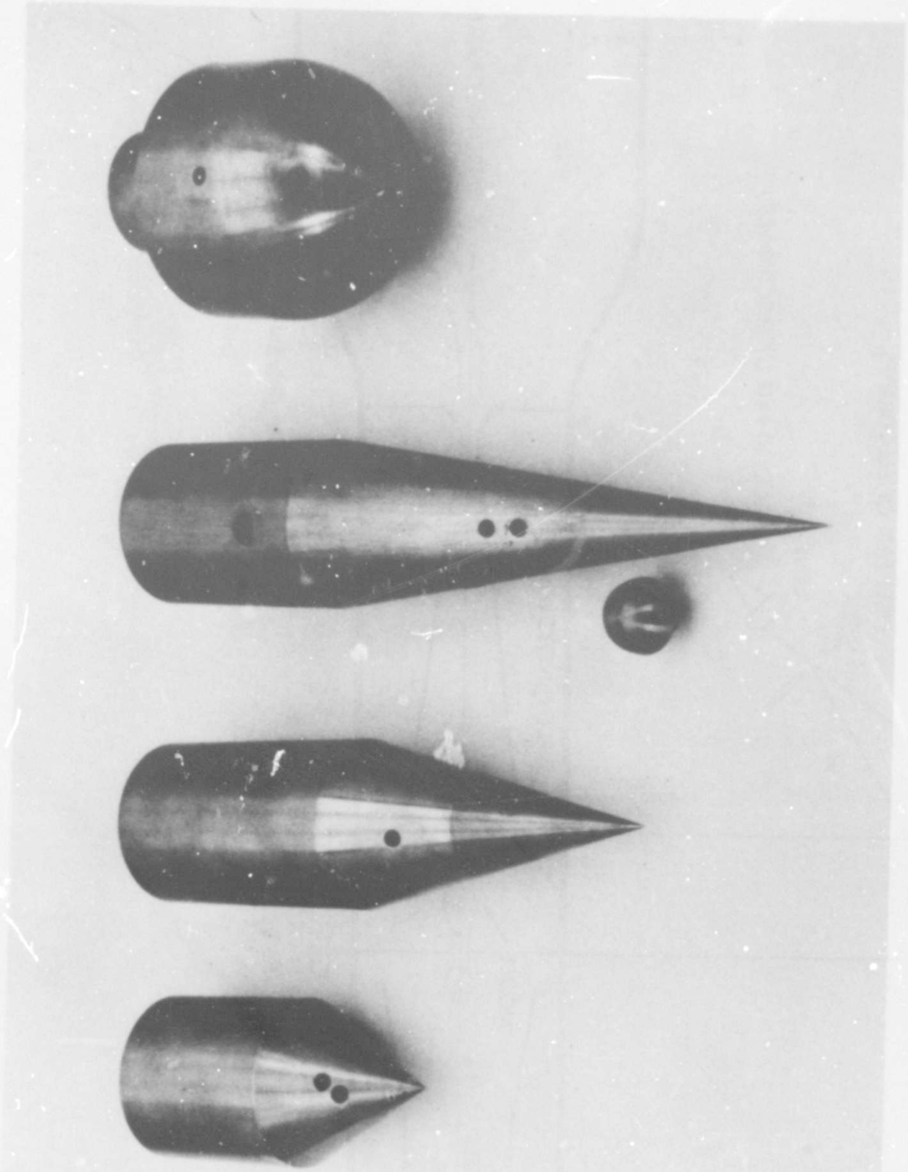

FIG. 2 PHOTOGRAPH OF THE TEST MODELS

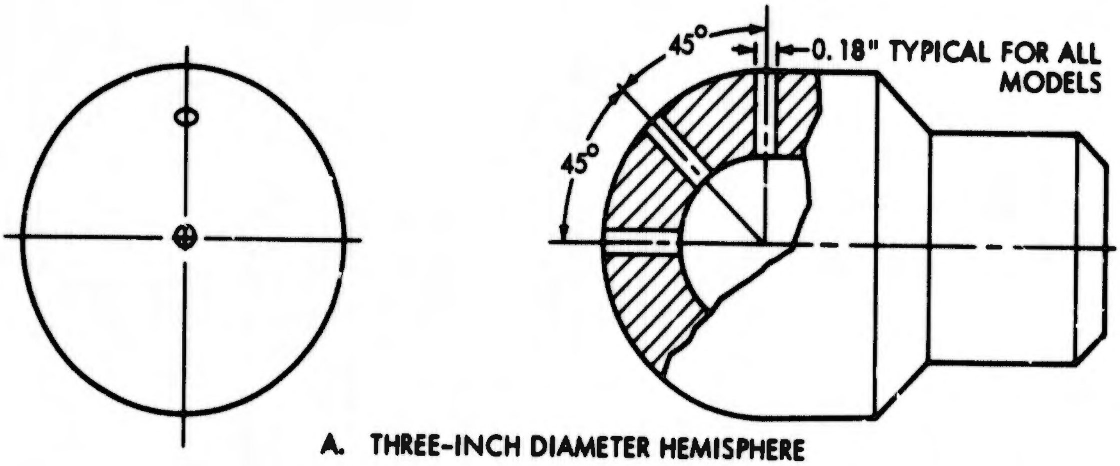

A. THREE-INCH DIAMETER HEMISPHERE

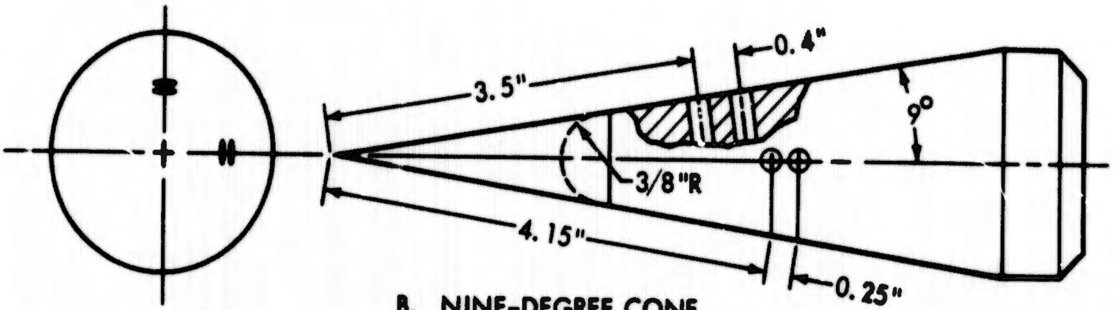

B. NINE-DEGREE CONE

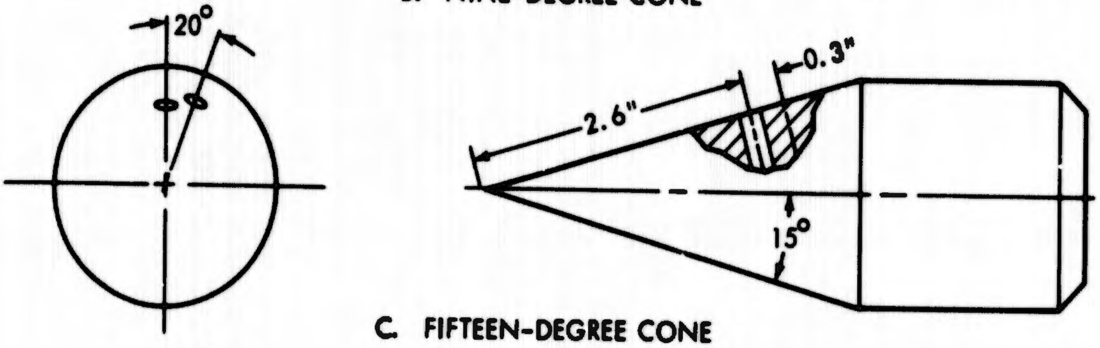

C. FIFTEEN-DEGREE CONE

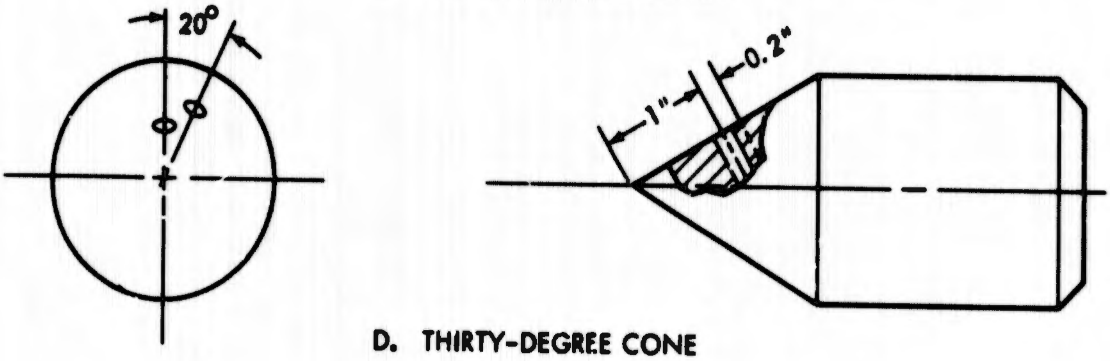

D. THIRTY-DEGREE CONE

FIG. 3 SCHEMATIC DRAWING OF THE TEST MODELS

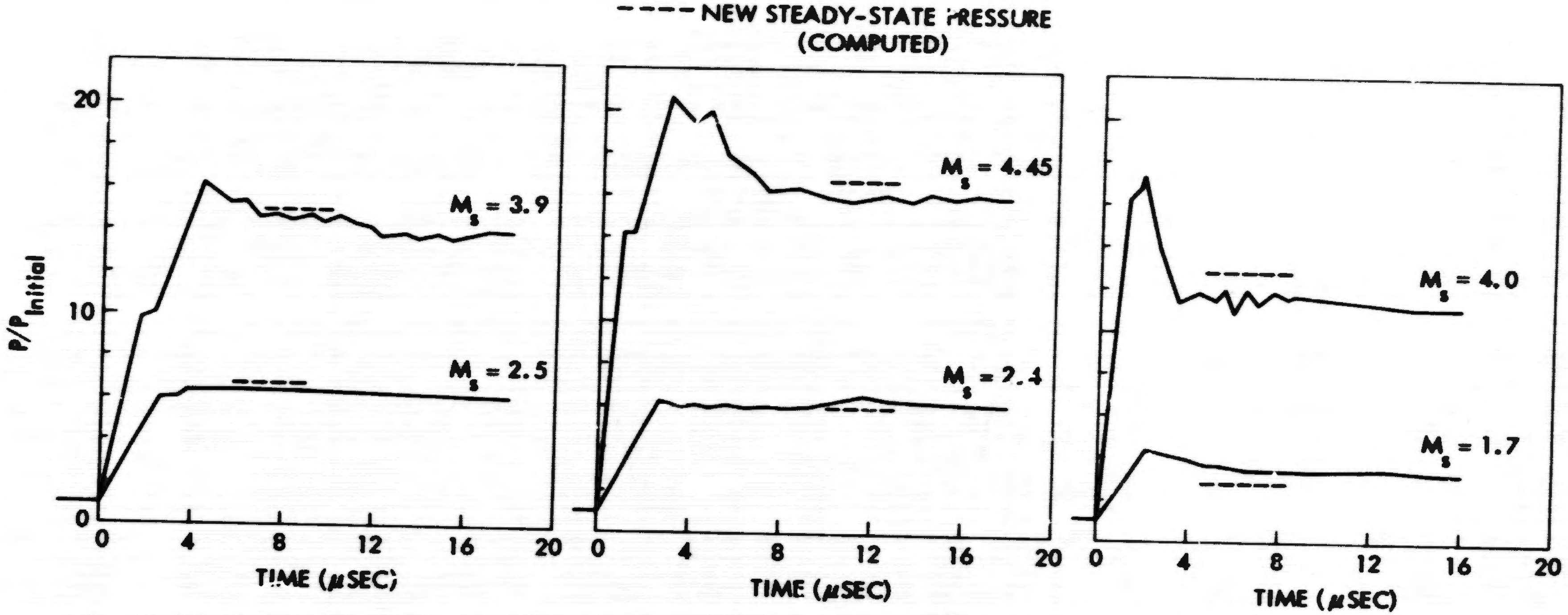

A. CONE SEMIVERTEX ANGLE, $\theta_c = 9°$ B. CONE SEMIVERTEX ANGLE, $\theta_c = 15°$ C. CONE SEMIVERTEX ANGLE, $\theta_c = 30°$

FIG. 4 TYPICAL PRESSURE-TIME HISTORIES FOR CONES OF DIFFERENT SEMIVERTEX ANGLES; FREE-STREAM MACH NUMBER, $M_1 = 5$ (NOMINAL)

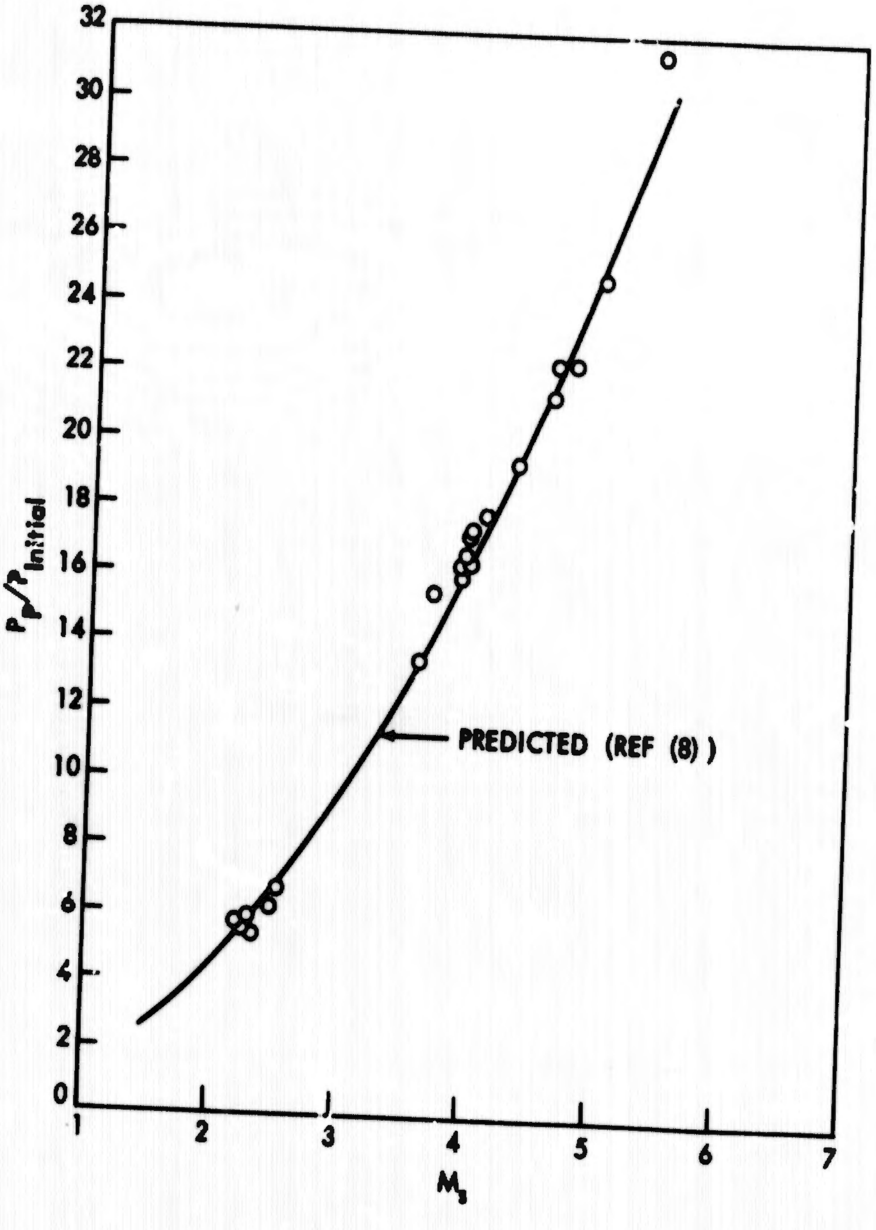

A. $\theta_c = 9^{\circ}$ $M_1 = 5.1$

FIG. 5 VARIATION OF SHOCK-INDUCED PEAK PRESSURE VS SHOCK INTENSITY

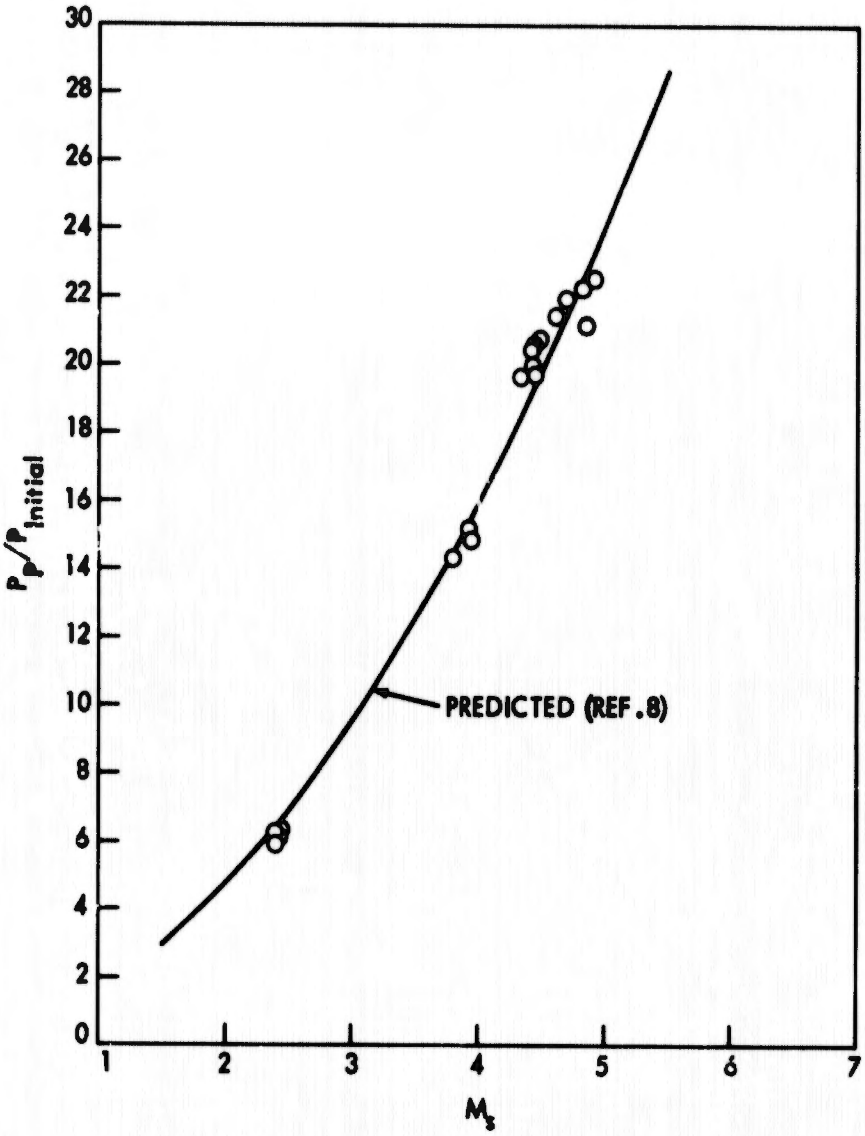

B. $\theta_c = 15^\circ$ $M_1 = 5.1$

FIG. 5 VARIATION OF SHOCK-INDUCED PEAK PRESSURE VS SHOCK INTENSITY (CONTINUED)

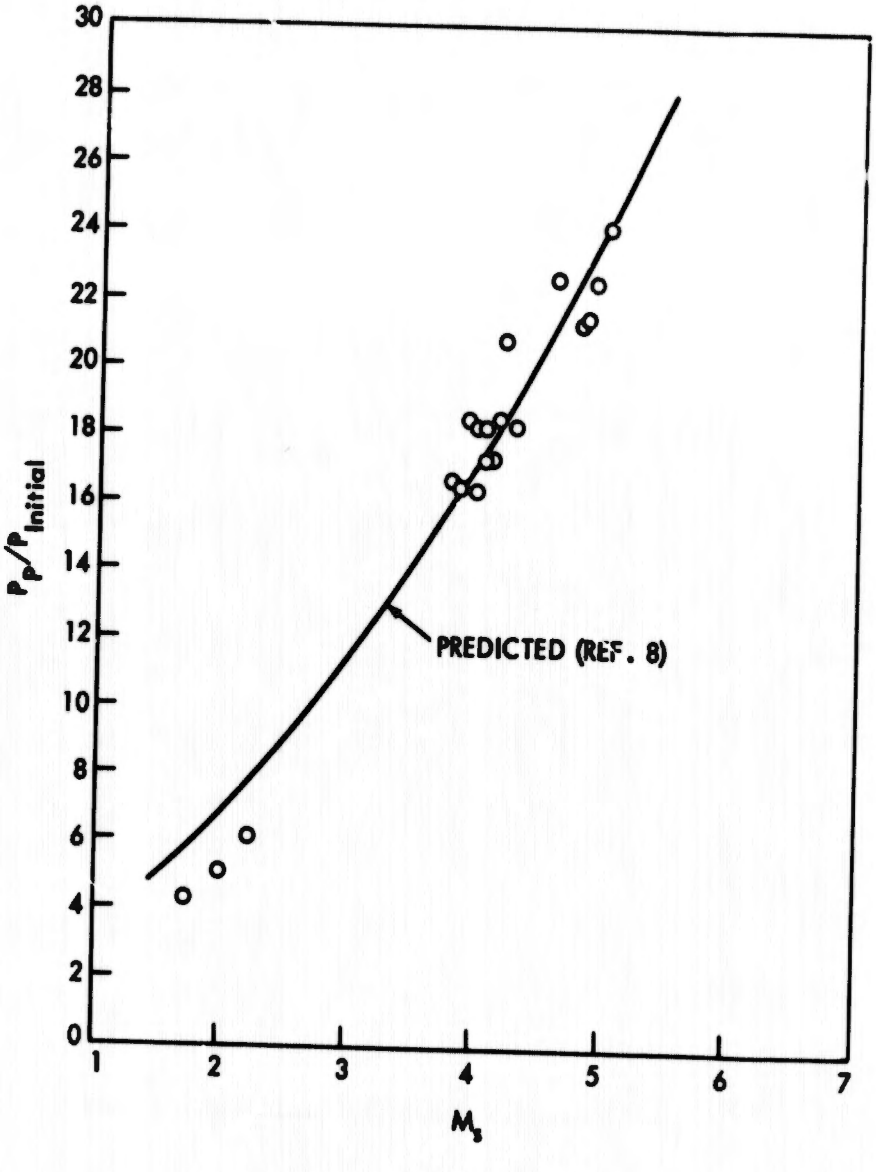

C. $\theta_c = 30^\circ$ $M_1 = 5.1$

FIG. 5 VARIATION OF SHOCK-INDUCED PEAK PRESSURE VS SHOCK INTENSITY (CONTINUED)

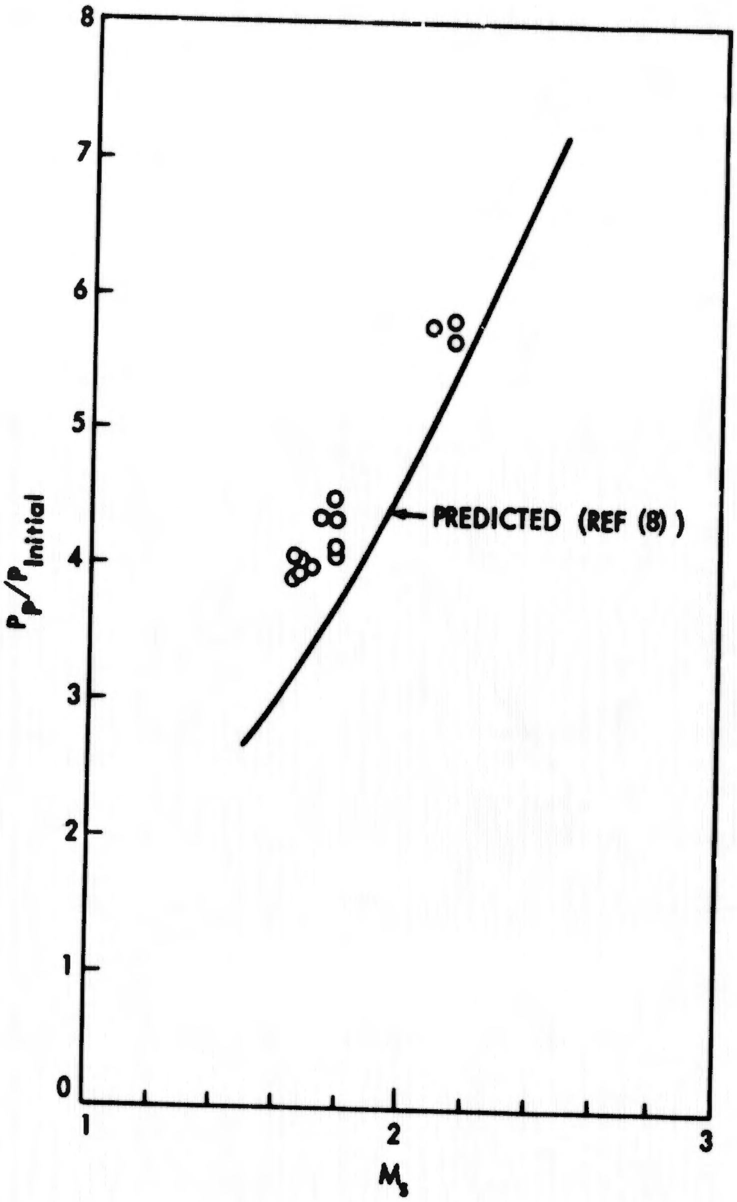

D. $\theta_c = 9^o$ $M_1 = 3.1$

FIG. 5 VARIATION OF SHOCK-INDUCED PEAK PRESSURE VS SHOCK INTENSITY (CONTINUED)

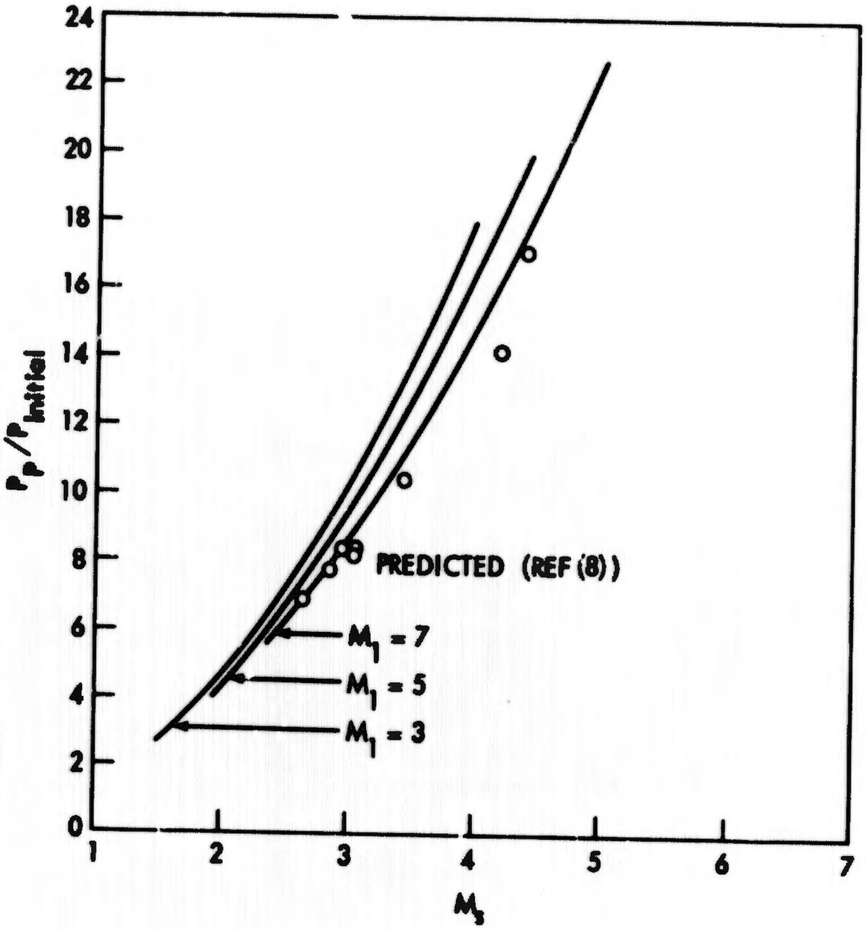

E. $\theta_c = 9°$ $M_1 = 7.0$

FIG. 5 VARIATION OF SHOCK-INDUCED PEAK PRESSURE VS SHOCK INTENSITY (CONTINUED)

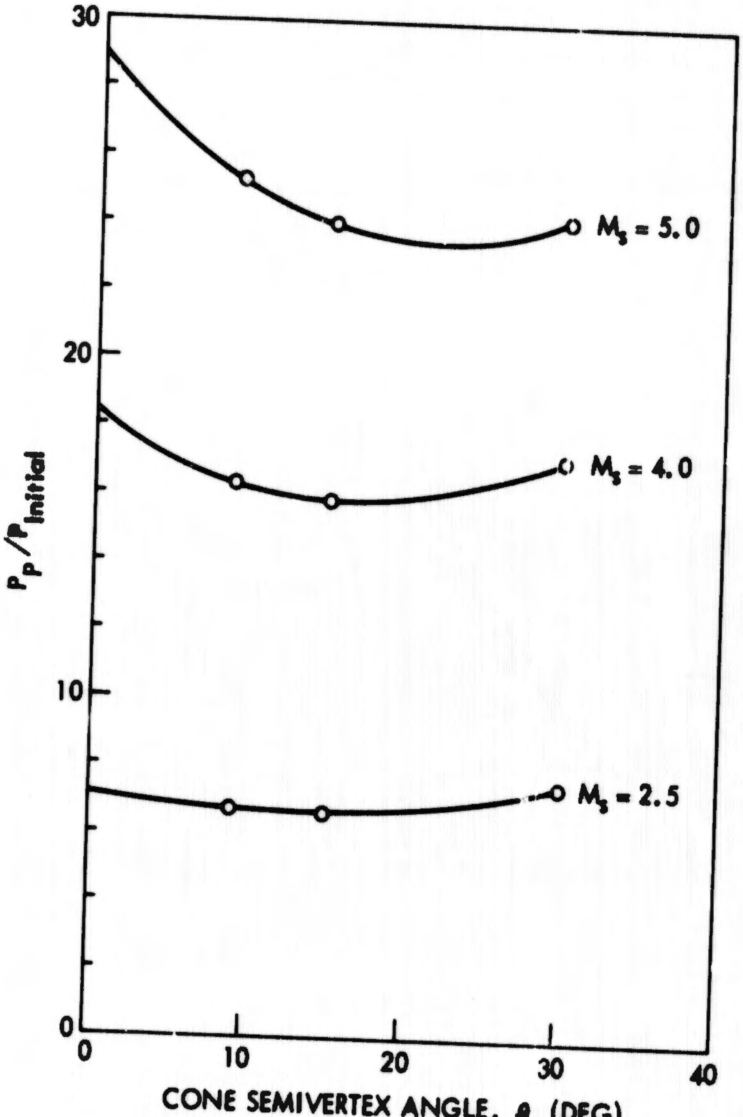

FIG. 6 VARIATION OF SHOCK-INDUCED PEAK PRESSURE WITH CONE ANGLE; FREE-STREAM MACH NUMBER, $M_1 = 5.1$

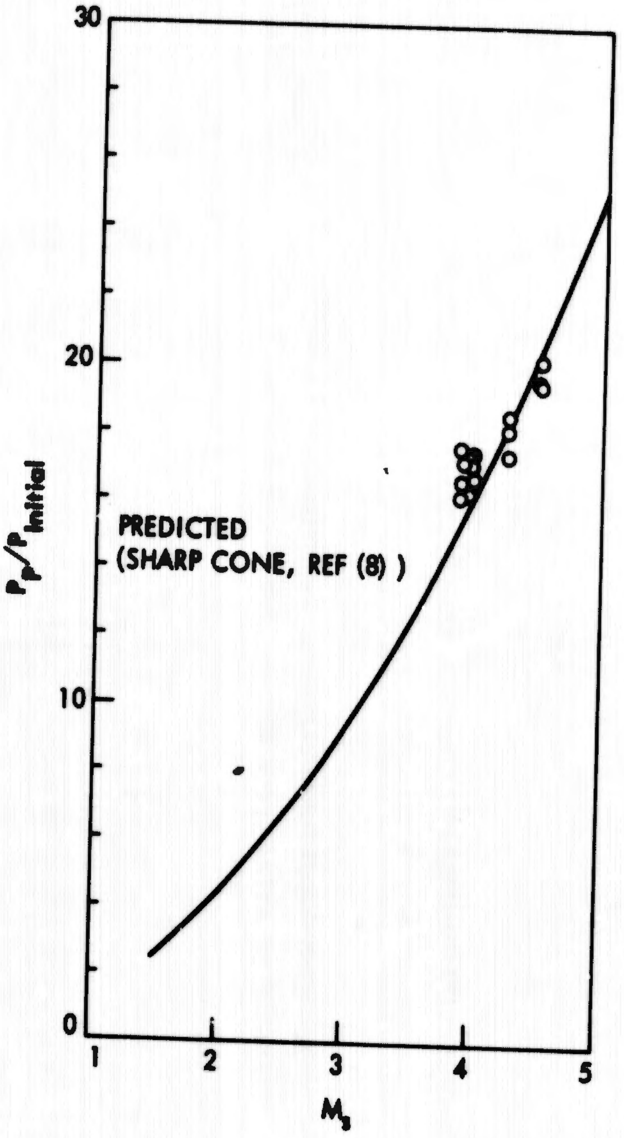

FIG. 7 SHOCK-INDUCED PEAK PRESSURE ON THE SURFACE OF A HEMISPHERICALLY BLUNTED 9° CONE; FREE-STREAM MACH NUMBER, M_1 = 5.1

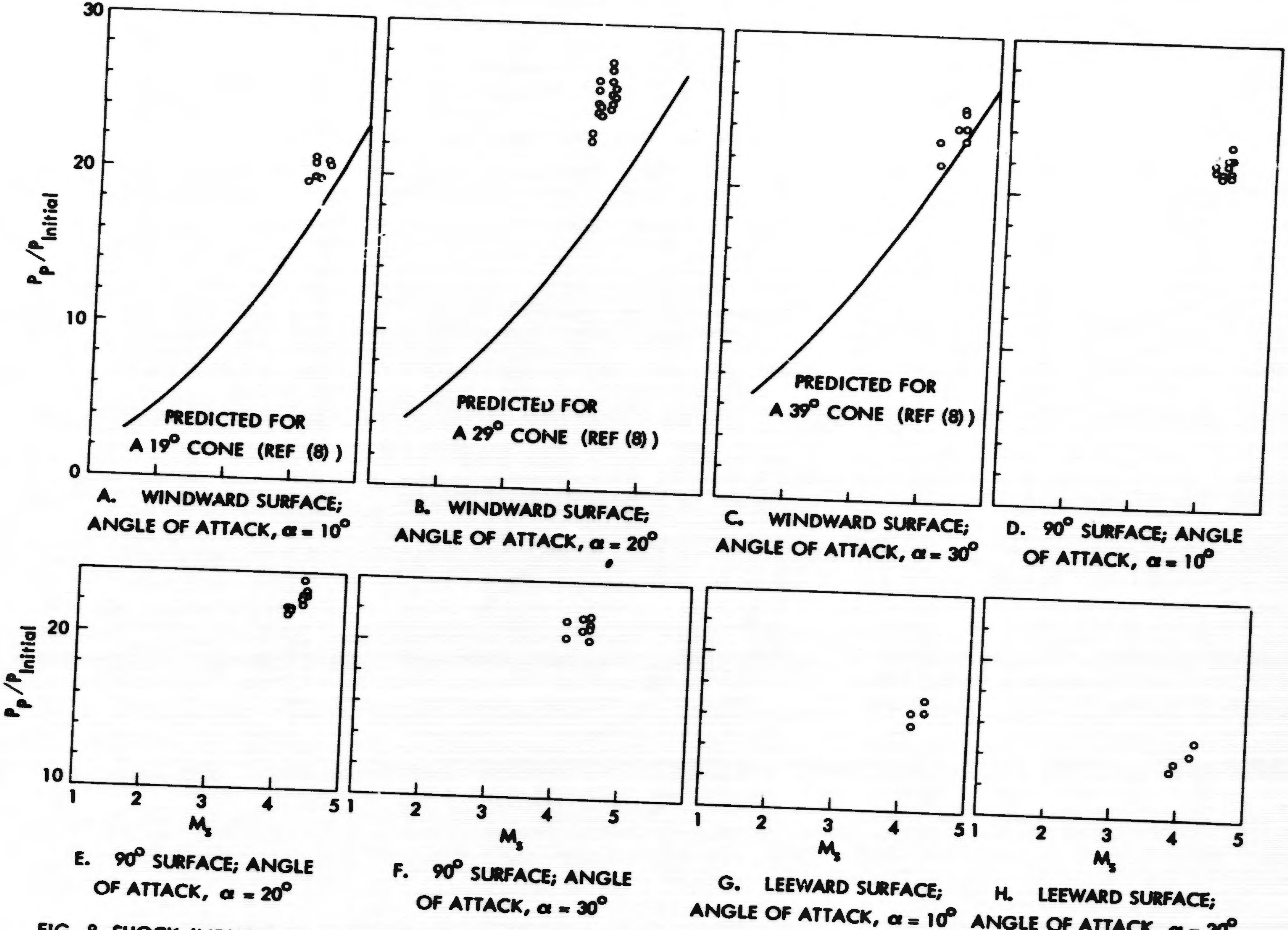

A. WINDWARD SURFACE; ANGLE OF ATTACK, $\alpha = 10°$

B. WINDWARD SURFACE; ANGLE OF ATTACK, $\alpha = 20°$

C. WINDWARD SURFACE; ANGLE OF ATTACK, $\alpha = 30°$

D. 90° SURFACE; ANGLE OF ATTACK, $\alpha = 10°$

E. 90° SURFACE; ANGLE OF ATTACK, $\alpha = 20°$

F. 90° SURFACE; ANGLE OF ATTACK, $\alpha = 30°$

G. LEEWARD SURFACE; ANGLE OF ATTACK, $\alpha = 10°$

H. LEEWARD SURFACE; ANGLE OF ATTACK, $\alpha = 20°$

FIG. 8 SHOCK-INDUCED PEAK PRESSURES FOR A 9° CONE AT ANGLES OF ATTACK; FREE-STREAM MACH NUMBER, $M_1 = 5.1$

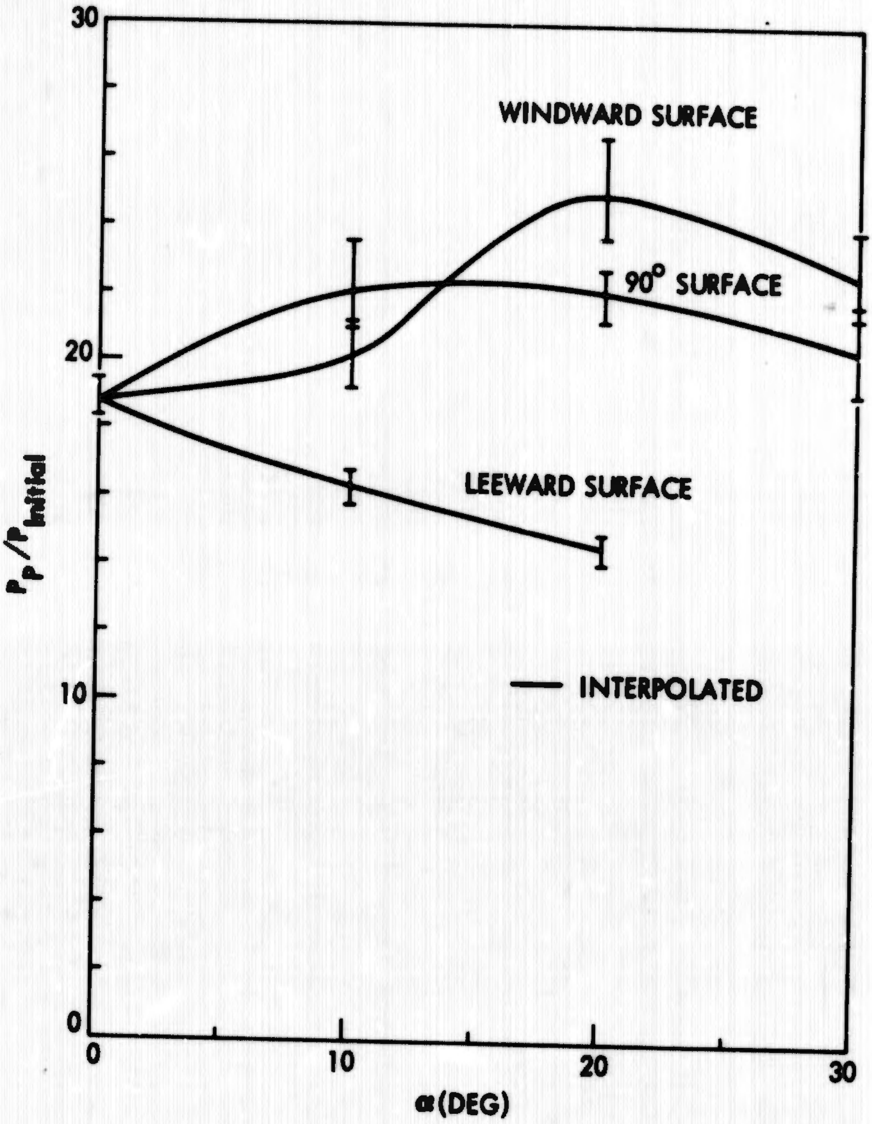

FIG. 9 VARIATION OF SHOCK-INDUCED PEAK PRESSURE WITH ANGLE OF ATTACK. FREE-STREAM MACH NUMBER, M_1 = 5.1; BLAST WAVE MACH NUMBER, M_s = 4.25.

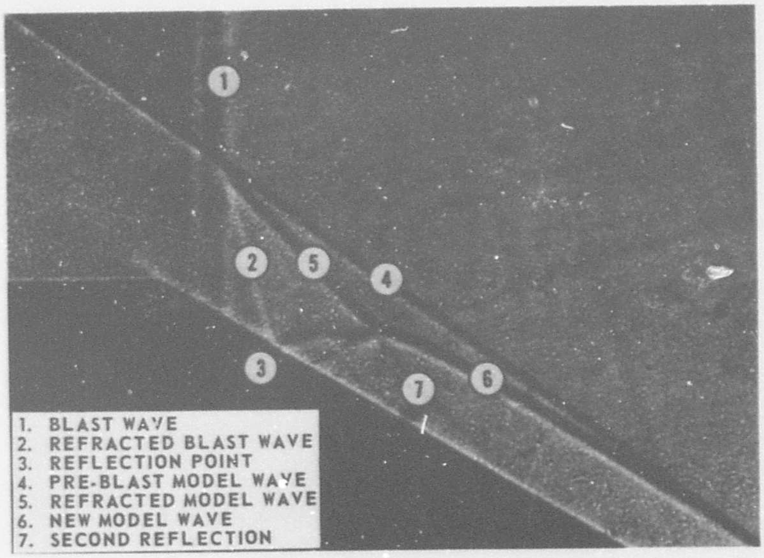

A. $M_1 = 5.07$ $M_s = 2.2$ (RUN 359)

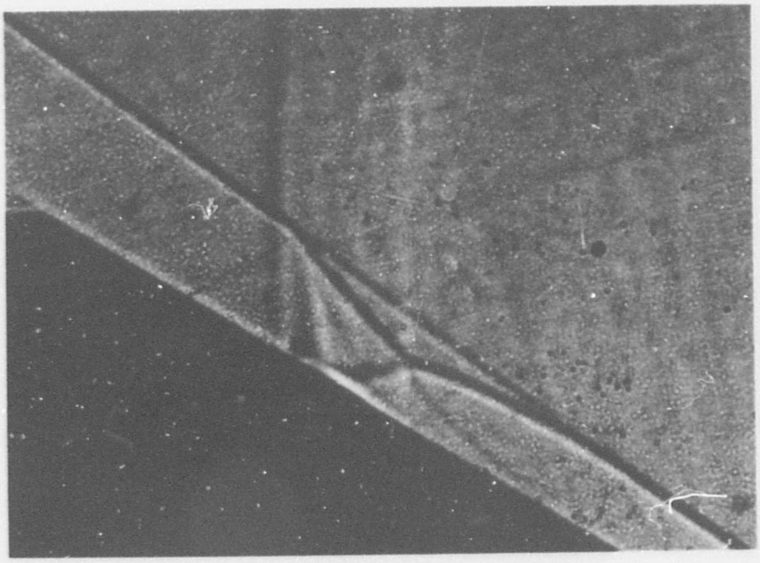

B. $M_1 = 5.07$ $M_s = 3.97$ (RUN 366)

FIG. 10 TWO-SPARK SHADOW PHOTOGRAPHS OF THE SHOCK INTERACTION FIELD ON THE SURFACE OF A 30° CONE

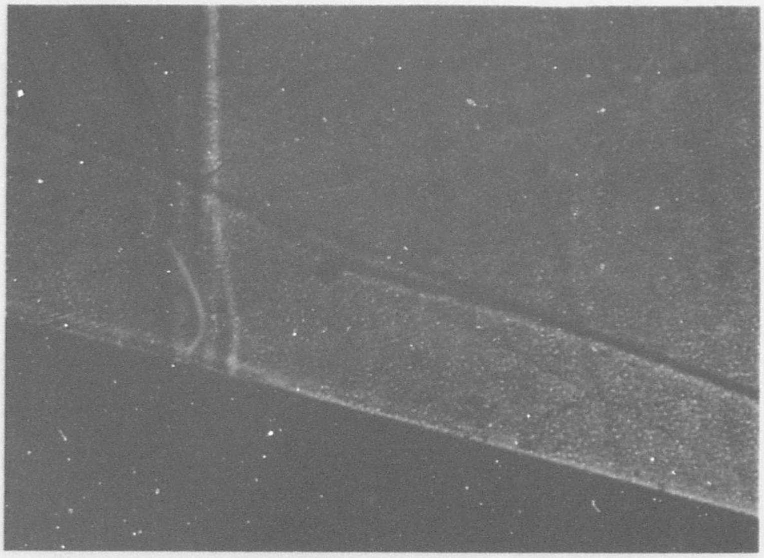

A. $M_1 = 5.07$ $M_s = 2.4$ (RUN 332)

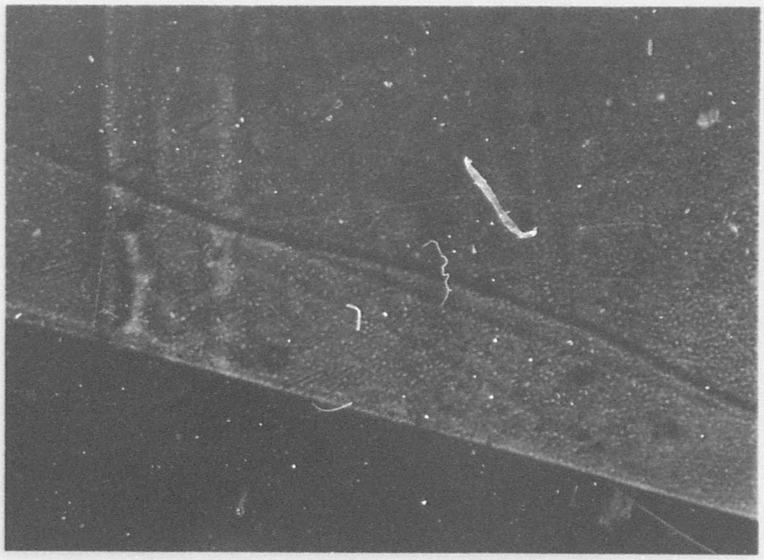

B. $M_1 = 5.07$ $M_s = 3.8$ (RUN 337)

FIG. 11 TWO-SPARK SHADOW PHOTOGRAPHS OF THE SHOCK INTERACTION FIELD ON THE SURFACE OF A 15° CONE

A. $M_1 = 5.0$ $M_s = 2.48$ (RUN 418)

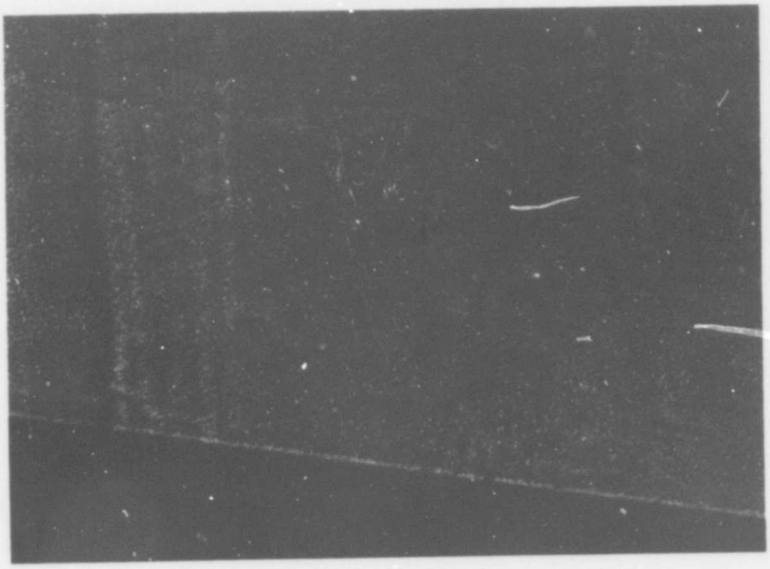

B. $M_1 = 5.03$ $M_s = 3.97$ (RUN 280)

FIG. 12 TWO-SPARK SHADOW PHOTOGRAPHS OF THE SHOCK INTERACTION FIELD ON THE SURFACE OF A 9° CONE

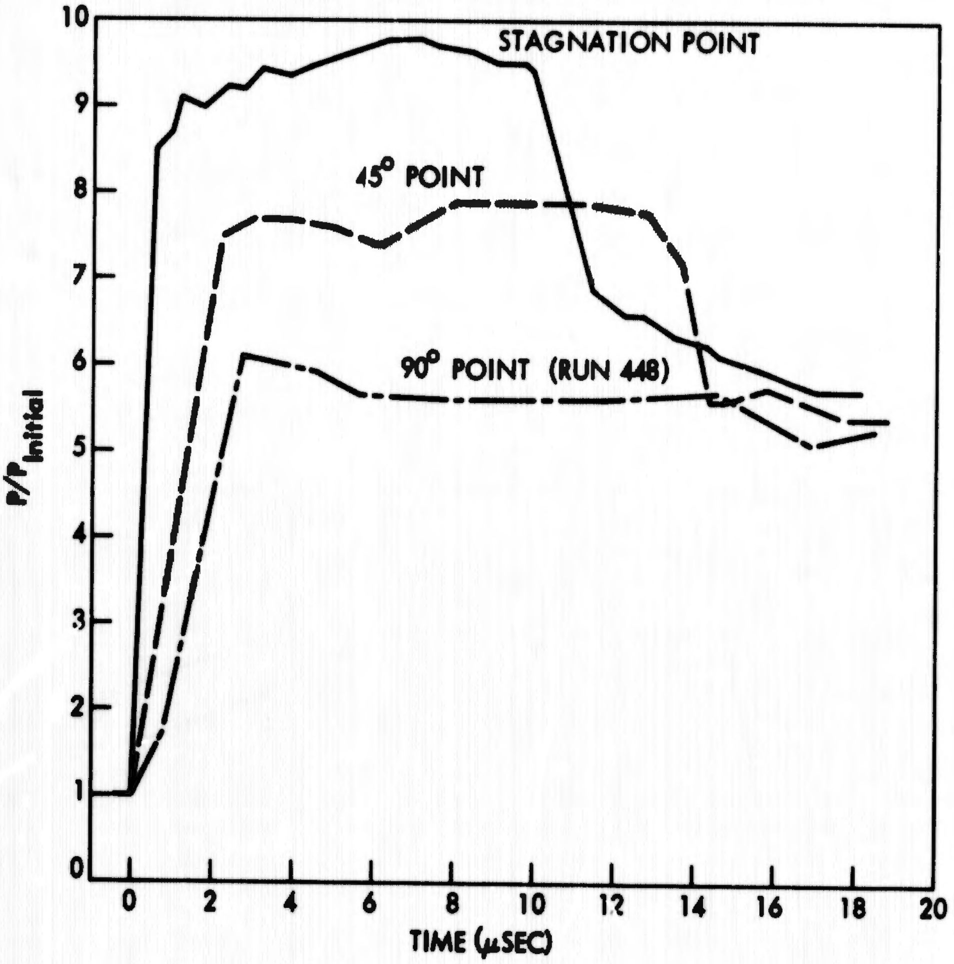

A. $M_1 = 5.07$, $M_s = 2.50$ (RUN 505)

FIG. 13 SHOCK-INDUCED PRESSURE-TIME VARIATIONS ON THE SURFACE OF A 3-INCH DIAMETER HEMISPHERE

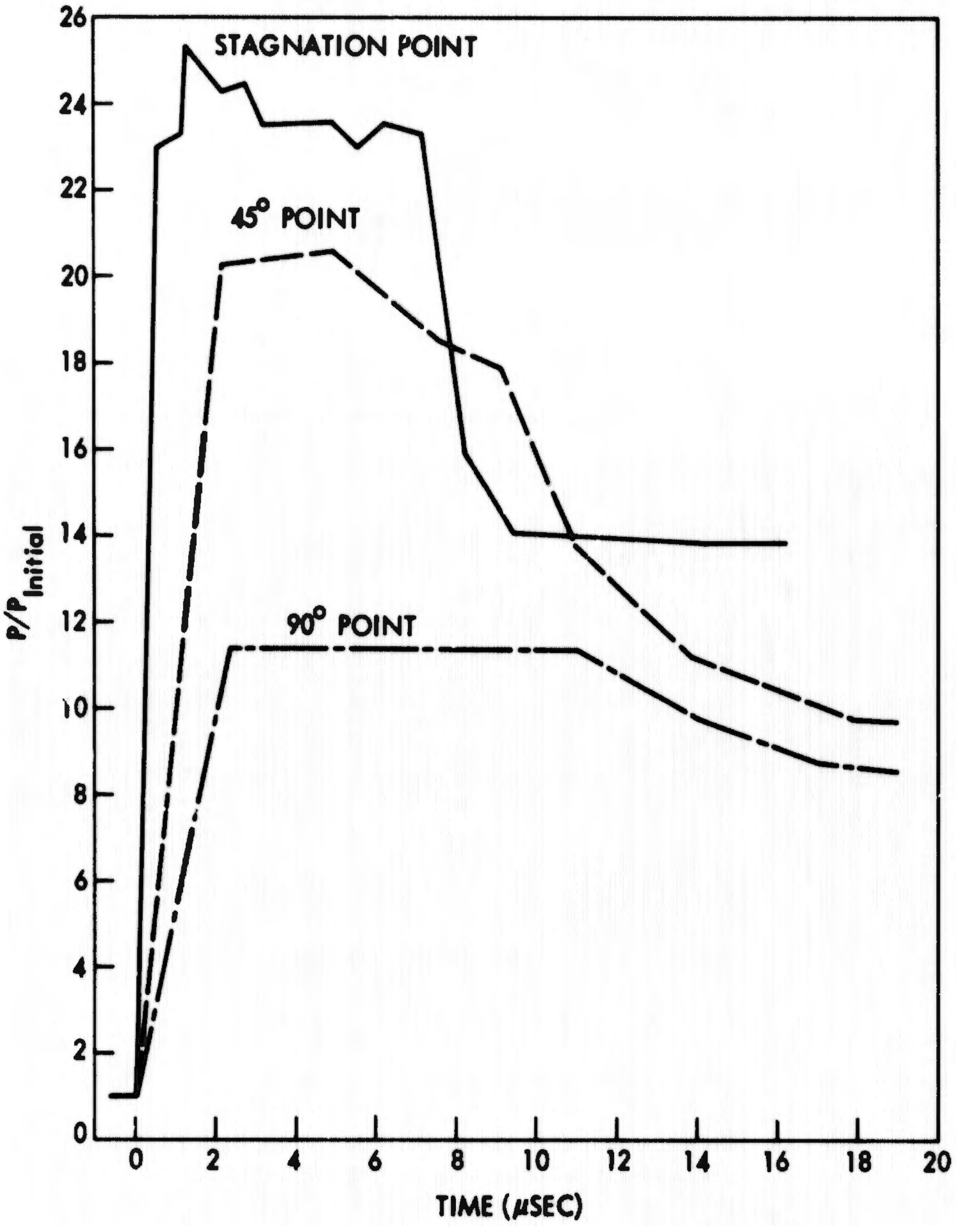

B. $M_1 = 5.05$, $M_s = 4.27$ (RUN 455)

FIG. 13 SHOCK-INDUCED PRESSURE-TIME VARIATIONS ON THE SURFACE OF A 3-INCH DIAMETER HEMISPHERE (CONTINUED)

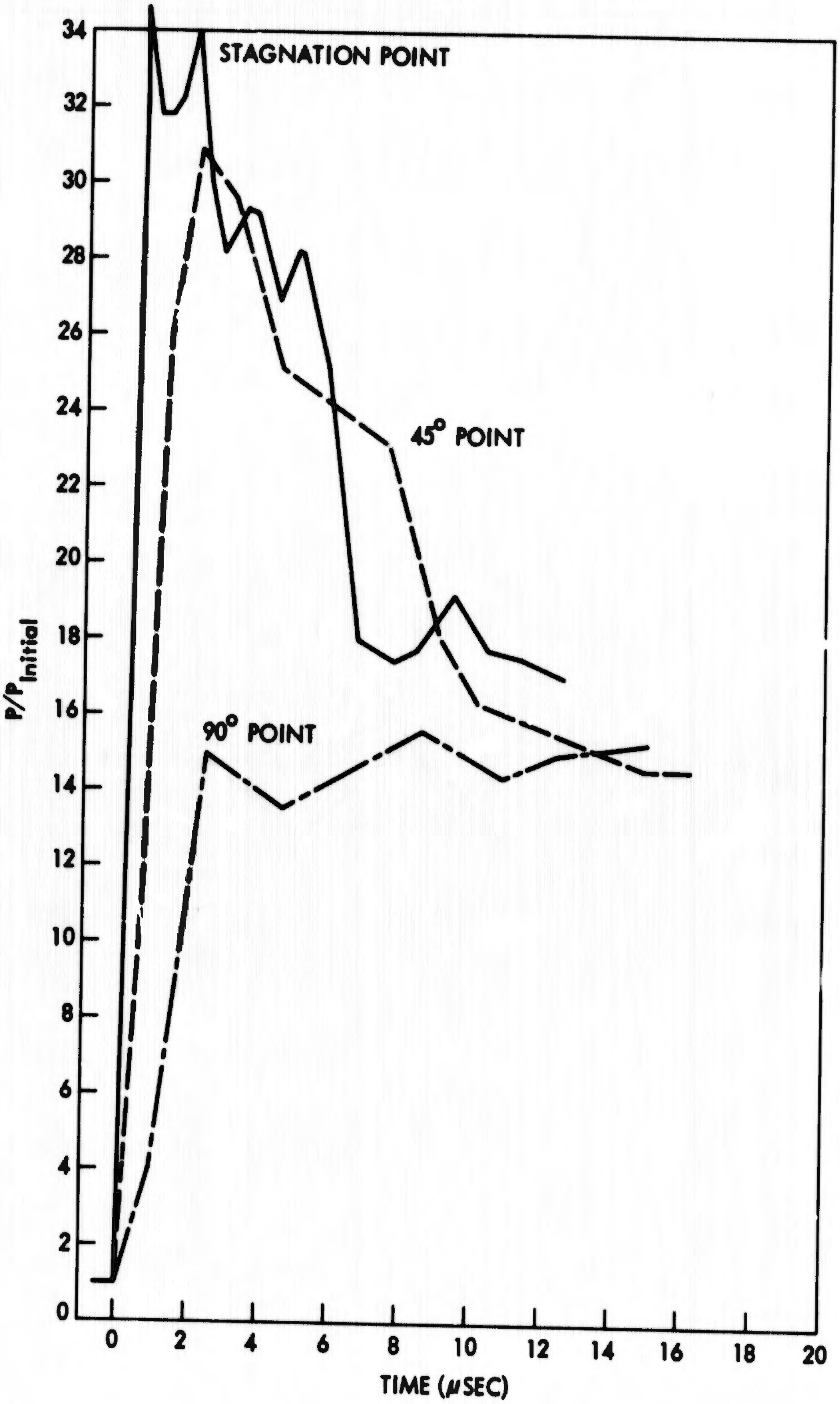

C. $M_1 = 5.07$, $M_s = 5.25$ (RUN 127)

FIG. 13 SHOCK-INDUCED PRESSURE-TIME VARIATIONS ON THE SURFACE OF A 3-INCH DIAMETER HEMISPHERE (CONTINUED)

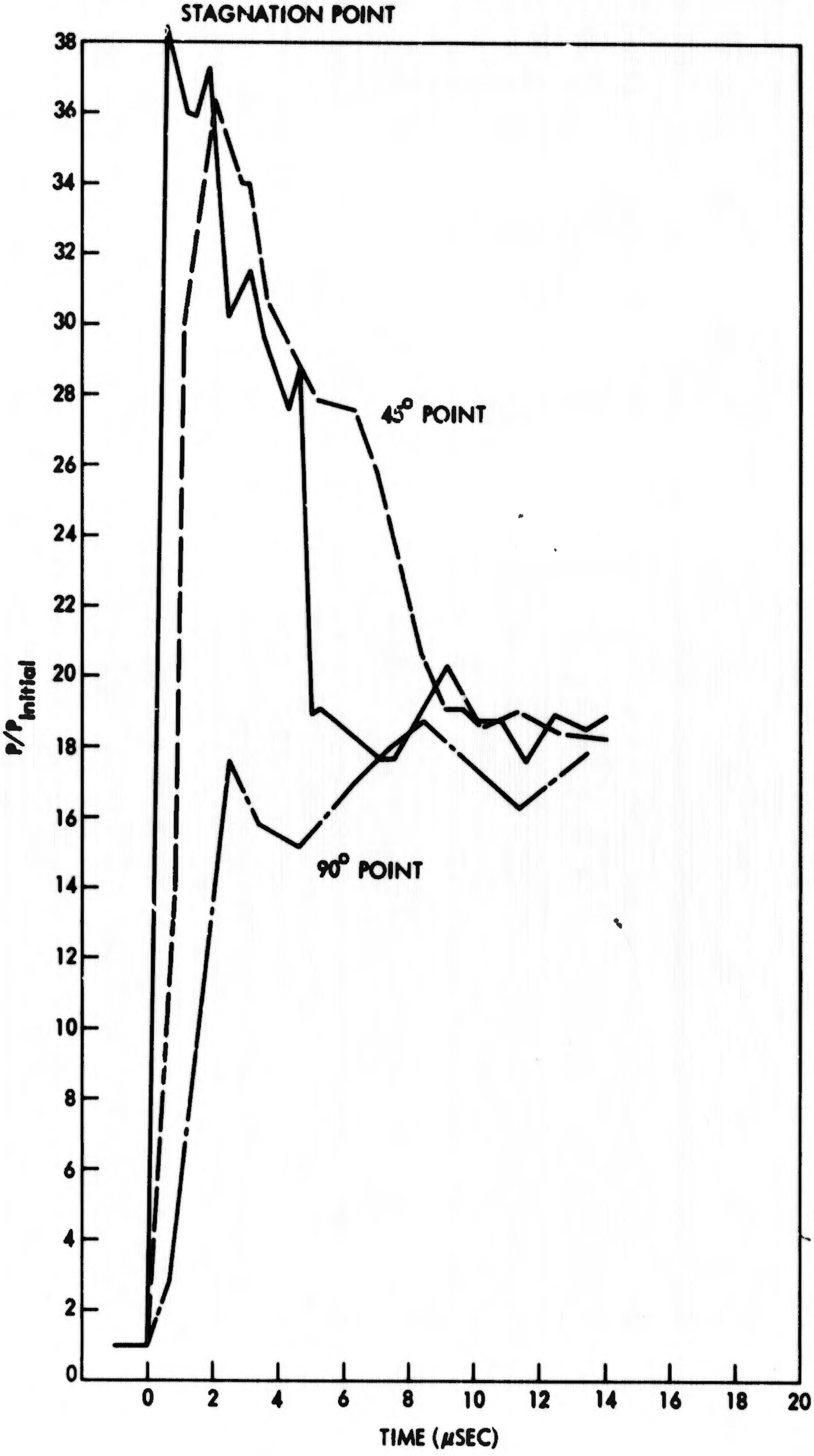

D. $M_1 = 5.07$, $M_s = 5.85$ (RUN 129)

FIG. 13 SHOCK-INDUCED PRESSURE-TIME VARIATIONS ON THE SURFACE OF A 3-INCH DIAMETER HEMISPHERE (CONTINUED)

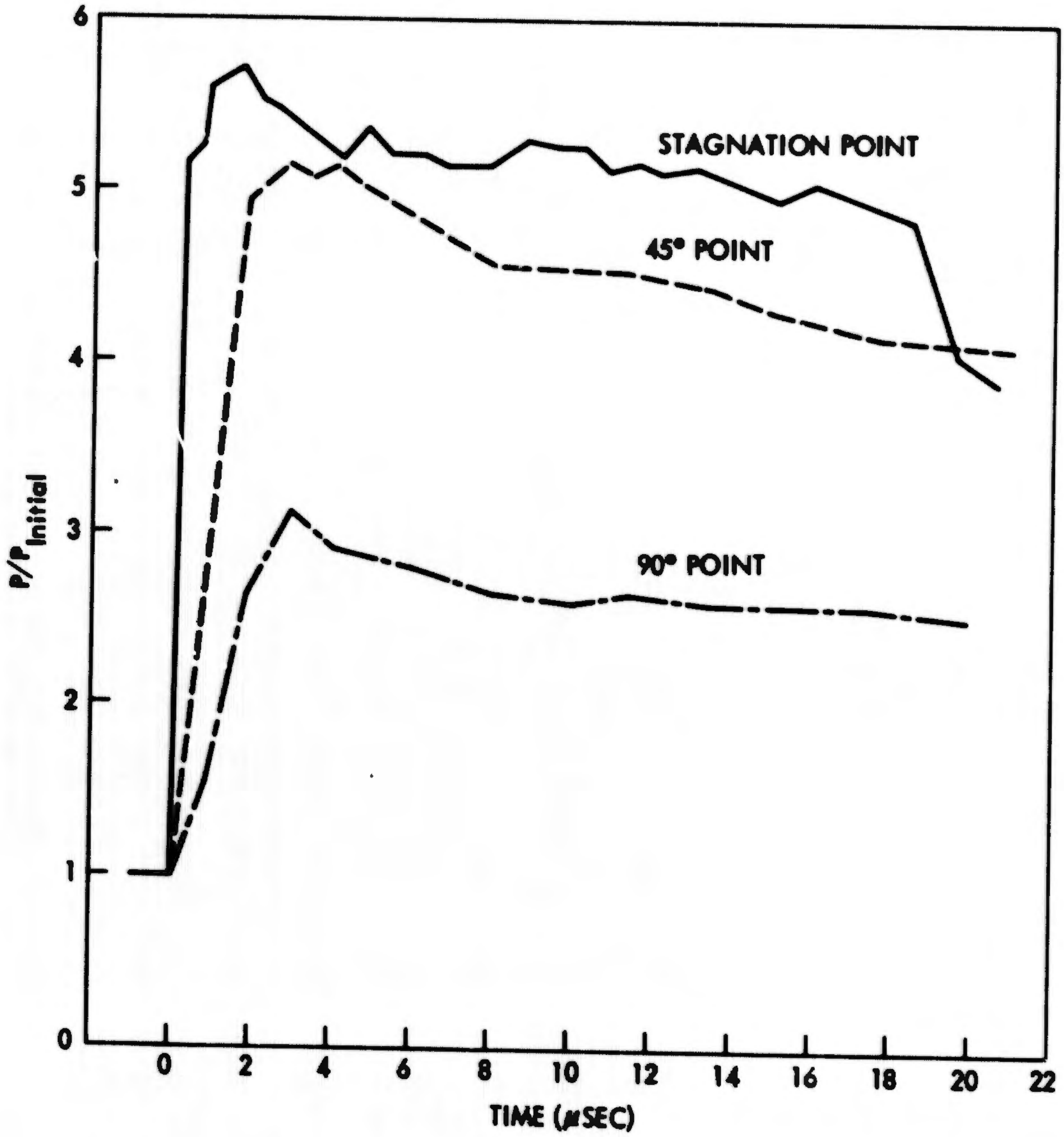

E. $M_1 = 3.1$, $M_s = 1.68$ (RUN 95)

FIG. 13 SHOCK-INDUCED PRESSURE-TIME VARIATIONS ON THE SURFACE OF A 3-INCH DIAMETER HEMISPHERE (CONTINUED)

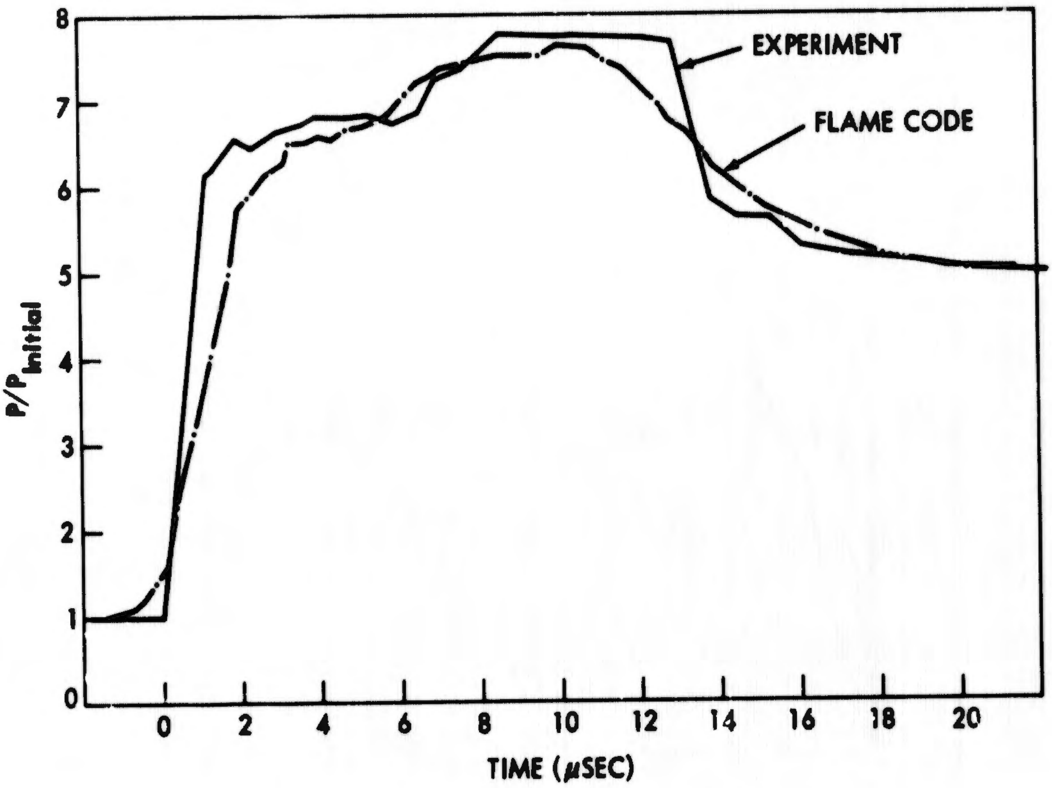

A. $M_1 = 5.07$, $M_s = 2.2$ (RUN 504)

FIG. 14 SHOCK-INDUCED PRESSURE-TIME VARIATION AT THE STAGNATION POINT OF A 3-INCH DIAMETER HEMISPHERE

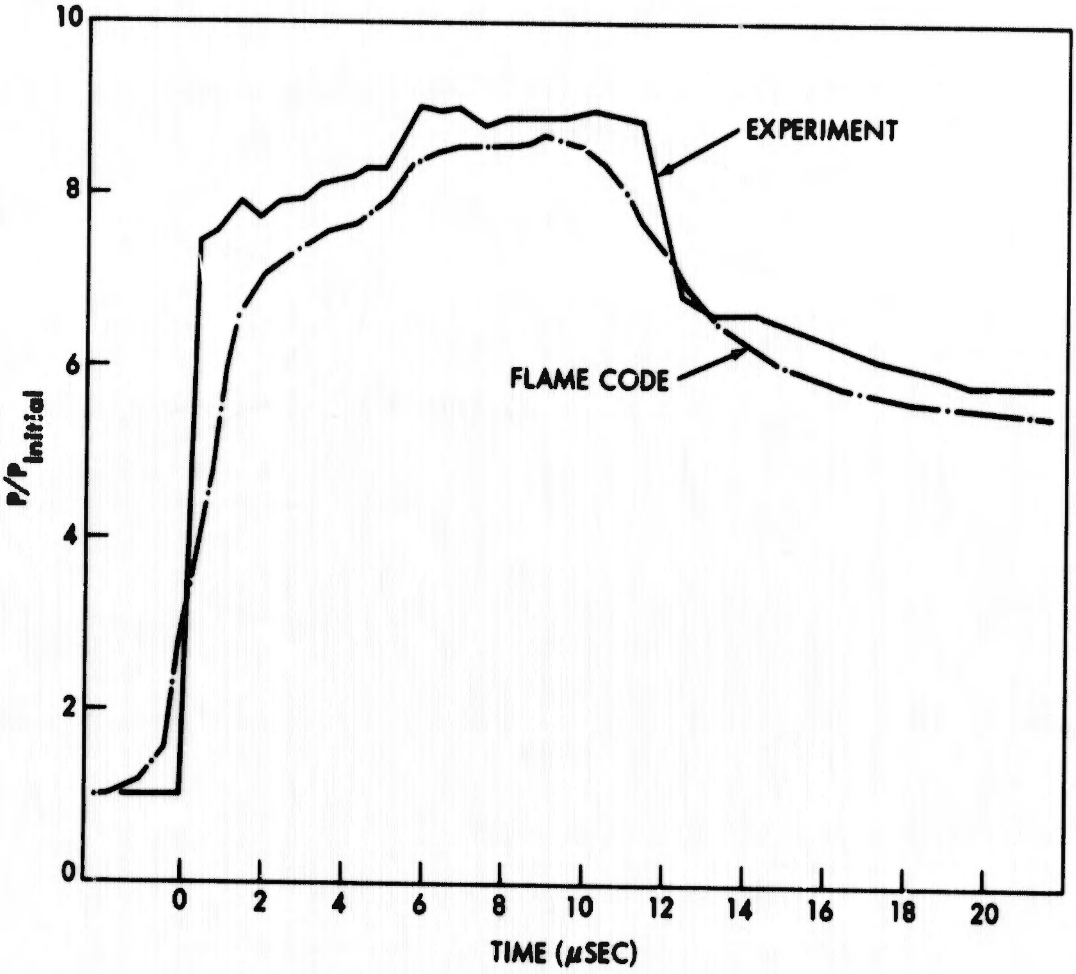

B. $M_1 = 5.07$, $M_s = 2.35$ (RUN 502)

FIG. 14 SHOCK-INDUCED PRESSURE-TIME VARIATION AT THE STAGNATION POINT OF A 3-INCH DIAMETER HEMISPHERE (CONTINUED)

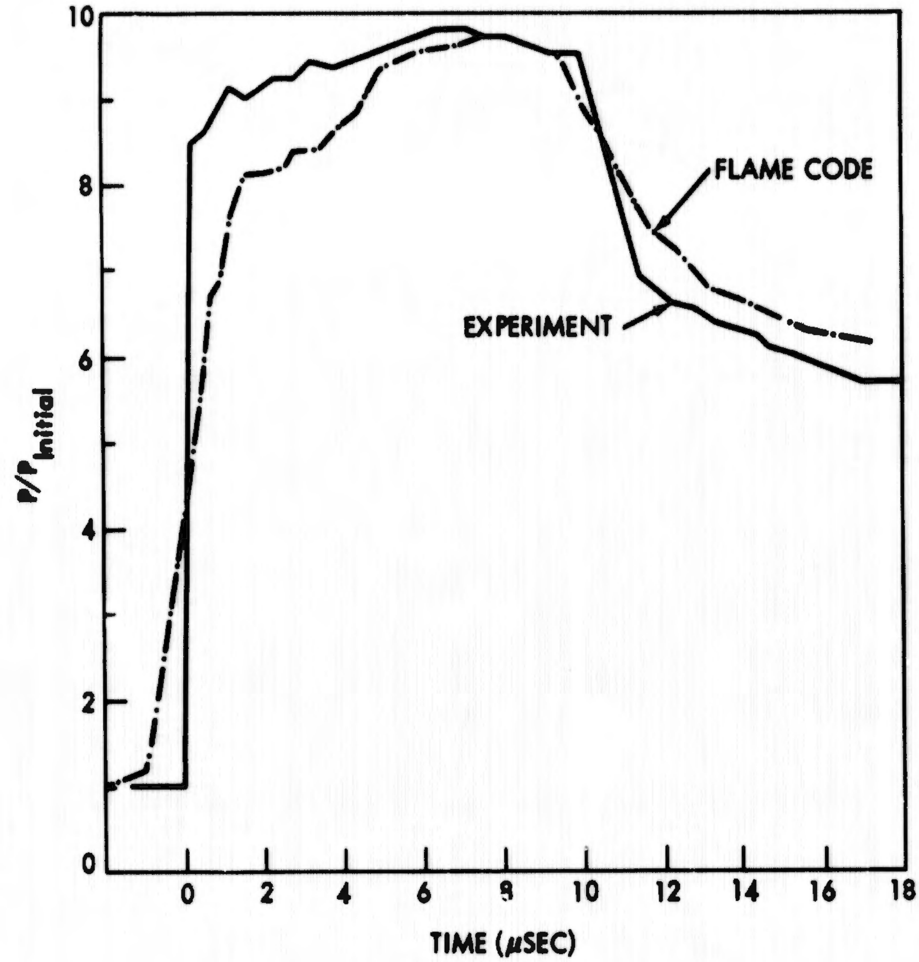

C. $M_1 = 5.07$, $M_s = 2.50$ (RUN 505)

FIG. 14 SHOCK-INDUCED PRESSURE-TIME VARIATION AT THE STAGNATION POINT OF A 3-INCH DIAMETER HEMISPHERE (CONTINUED)

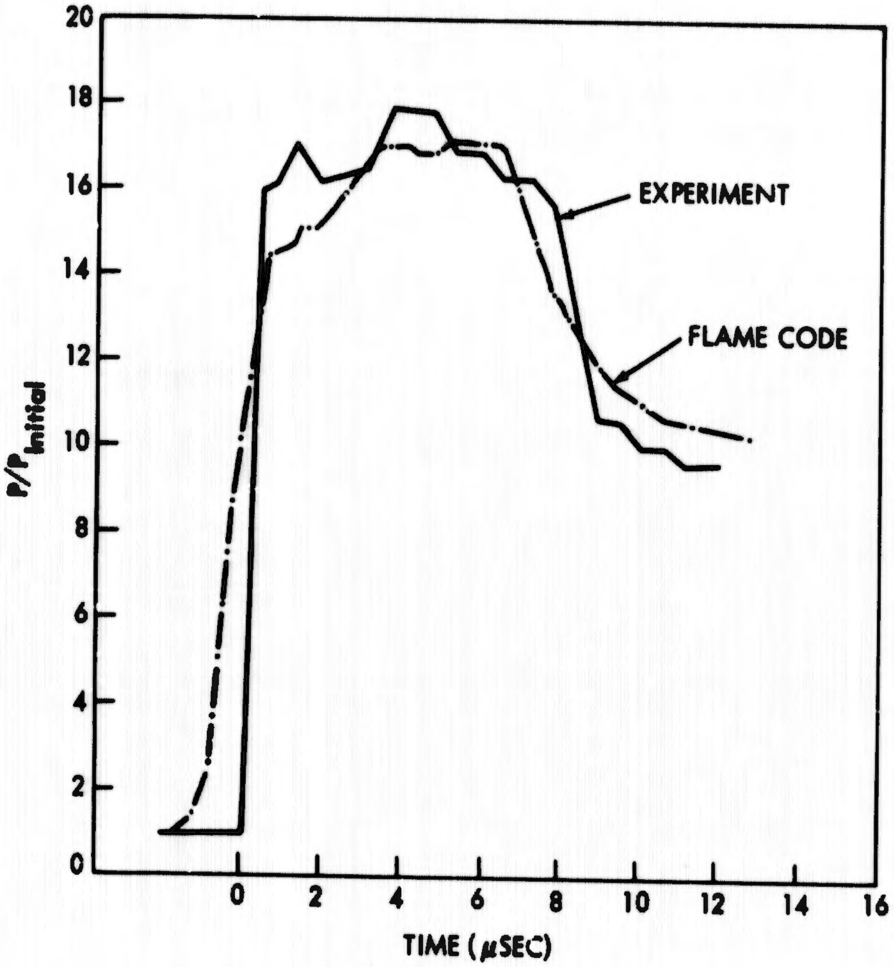

D. $M_1 = 5.07$, $M_s = 3.50$ (RUN 511)

FIG. 14 SHOCK-INDUCED PRESSURE-TIME VARIATION AT THE STAGNATION POINT OF A 3-INCH DIAMETER HEMISPHERE (CONTINUED)

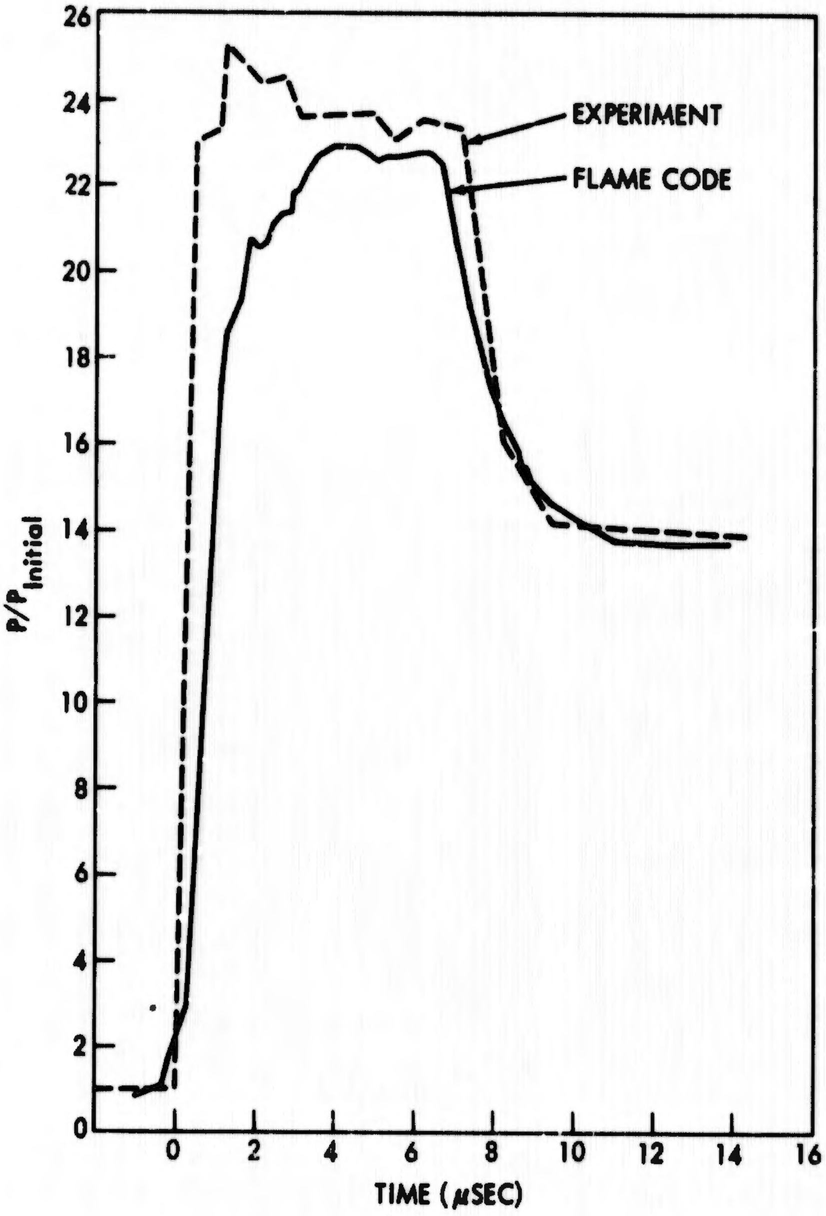

E. $M_1 = 5.05$, $M_s = 4.27$ (RUN 455)

FIG. 14 SHOCK-INDUCED PRESSURE-TIME VARIATION AT THE STAGNATION POINT OF A 3-INCH DIAMETER HEMISPHERE (CONTINUED)

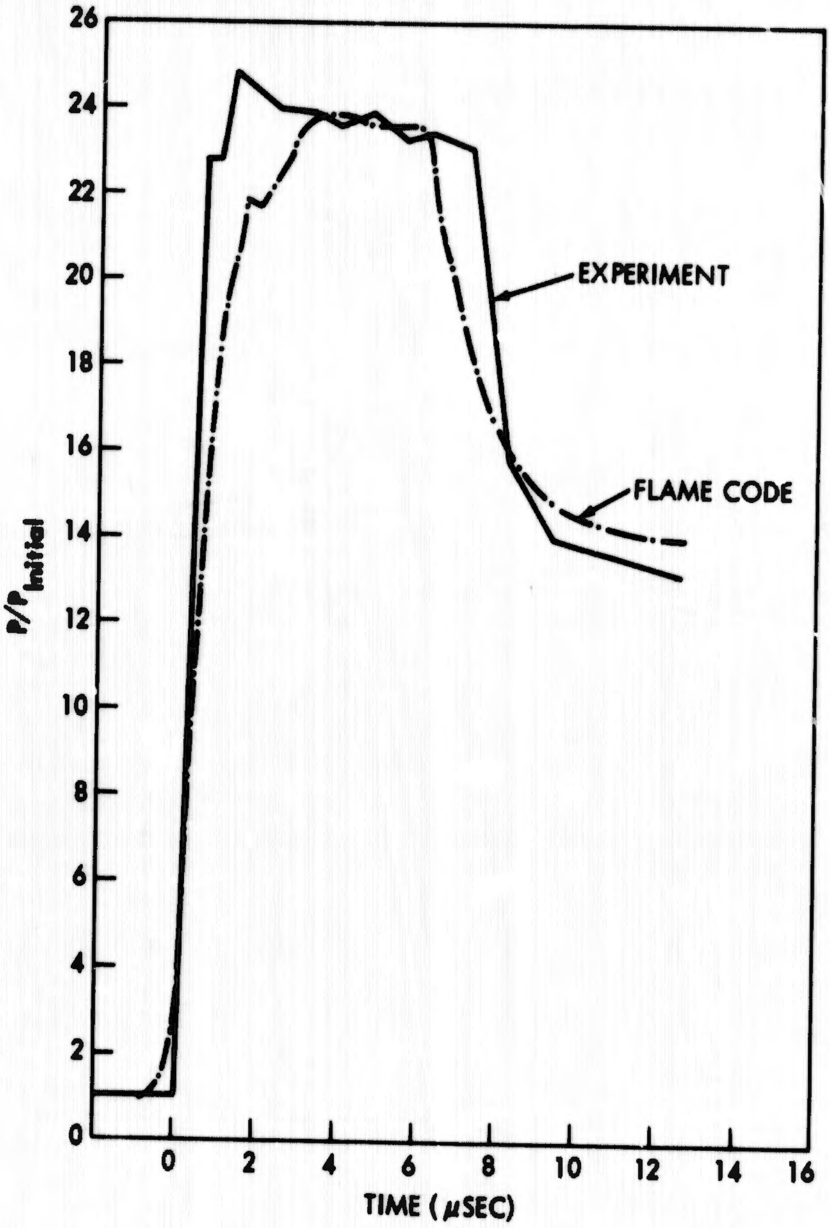

F. $M_1 = 5.05$, $M_s = 4.44$ (RUN 456)

FIG. 14 SHOCK-INDUCED PRESSURE-TIME VARIATION AT THE STAGNATION POINT OF A 3-INCH DIAMETER HEMISPHERE (CONTINUED)

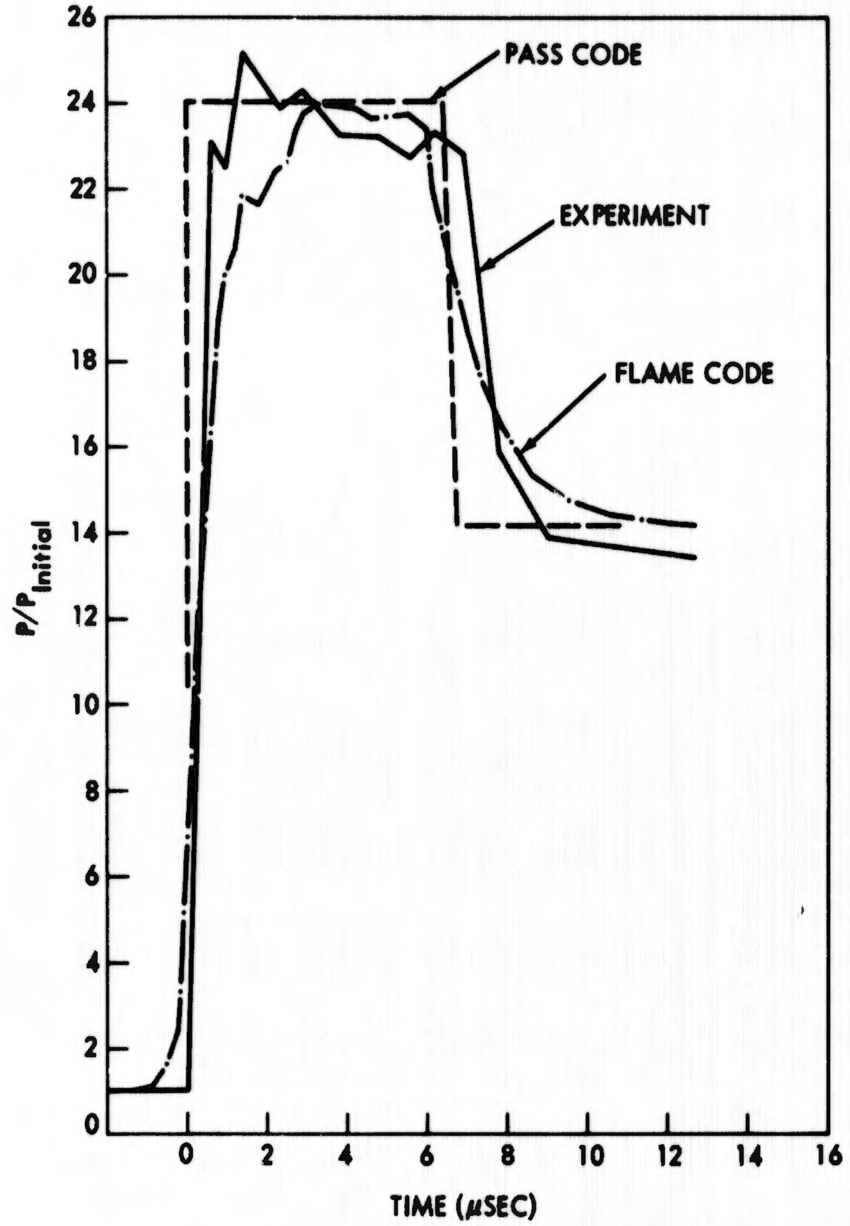

G. $M_1 = 5.05$, $M_s = 4.45$ (RUN 457)

FIG. 14 SHOCK-INDUCED PRESSURE-TIME VARIATION AT THE STAGNATION POINT OF A 3-INCH DIAMETER HEMISPHERE (CONTINUED)

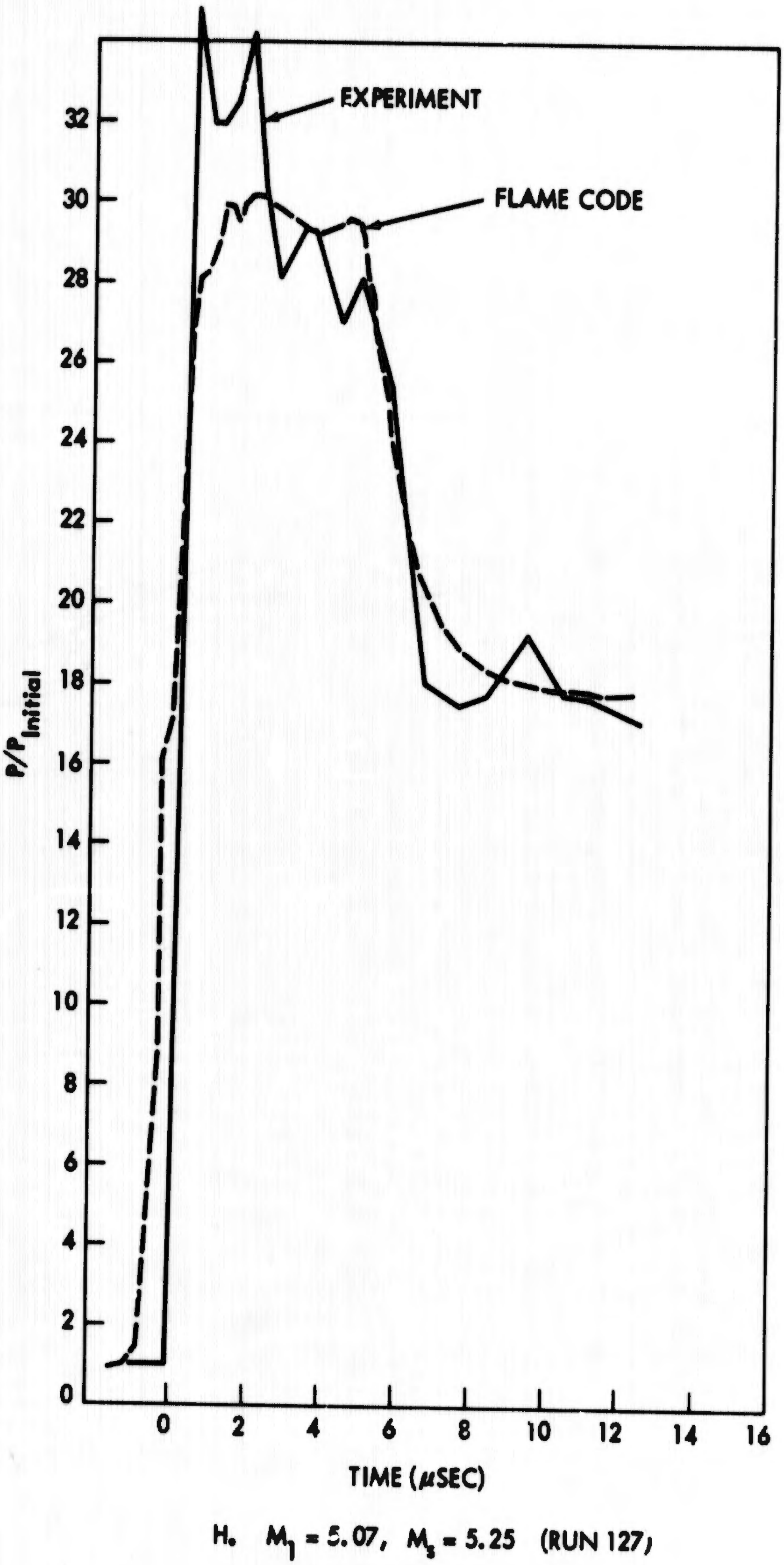

H. $M_1 = 5.07$, $M_s = 5.25$ (RUN 127)

FIG. 14 SHOCK-INDUCED PRESSURE-TIME VARIATION AT THE STAGNATION POINT OF A 3-INCH DIAMETER HEMISPHERE (CONTINUED)

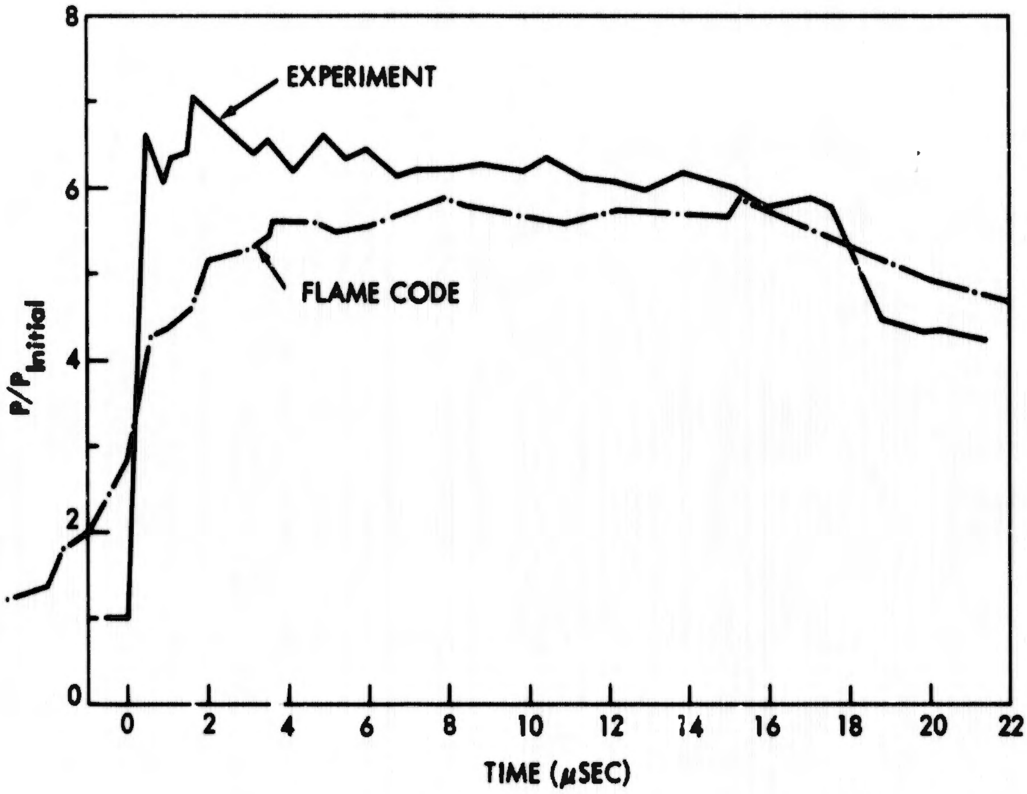

I. $M_1 = 3.07$, $M_s = 1.83$ (RUN 793)

FIG. 14 SHOCK-INDUCED PRESSURE-TIME VARIATION AT THE STAGNATION POINT OF A 3-INCH DIAMETER HEMISPHERE (CONTINUED)

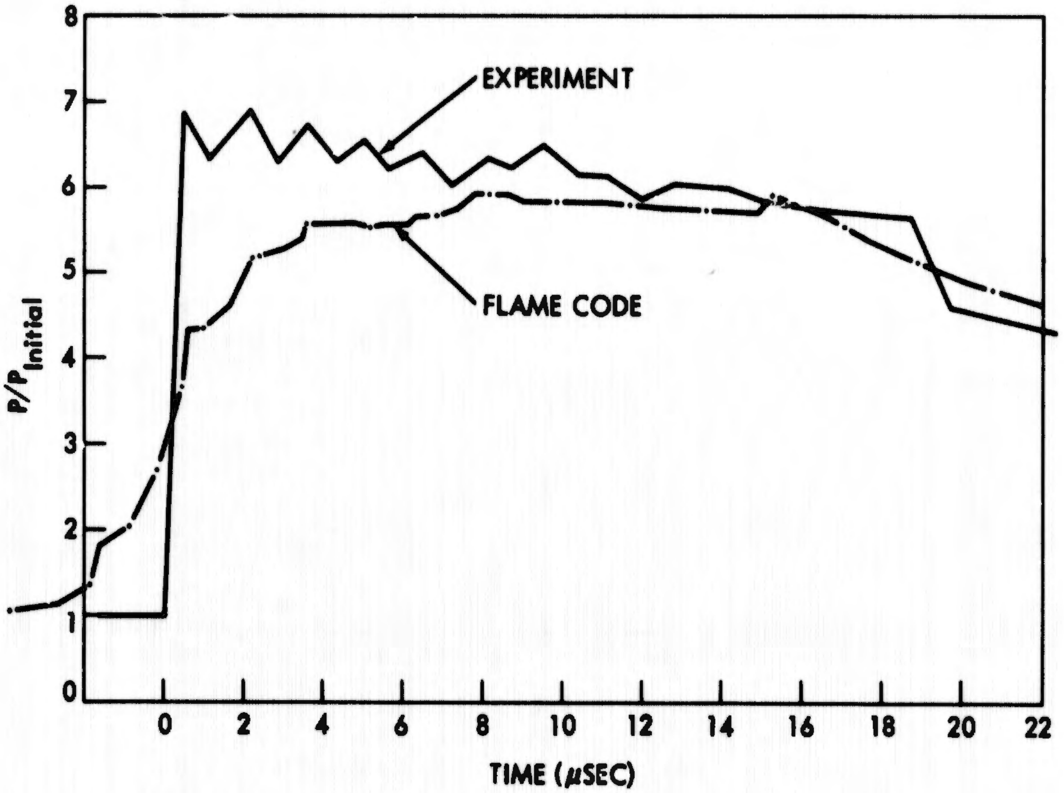

J. $M_1 = 3.09$, $M_s = 1.85$ (RUN 135)

FIG. 14 SHOCK-INDUCED PRESSURE-TIME VARIATION AT THE STAGNATION POINT OF A 3-INCH DIAMETER HEMISPHERE (CONTINUED)

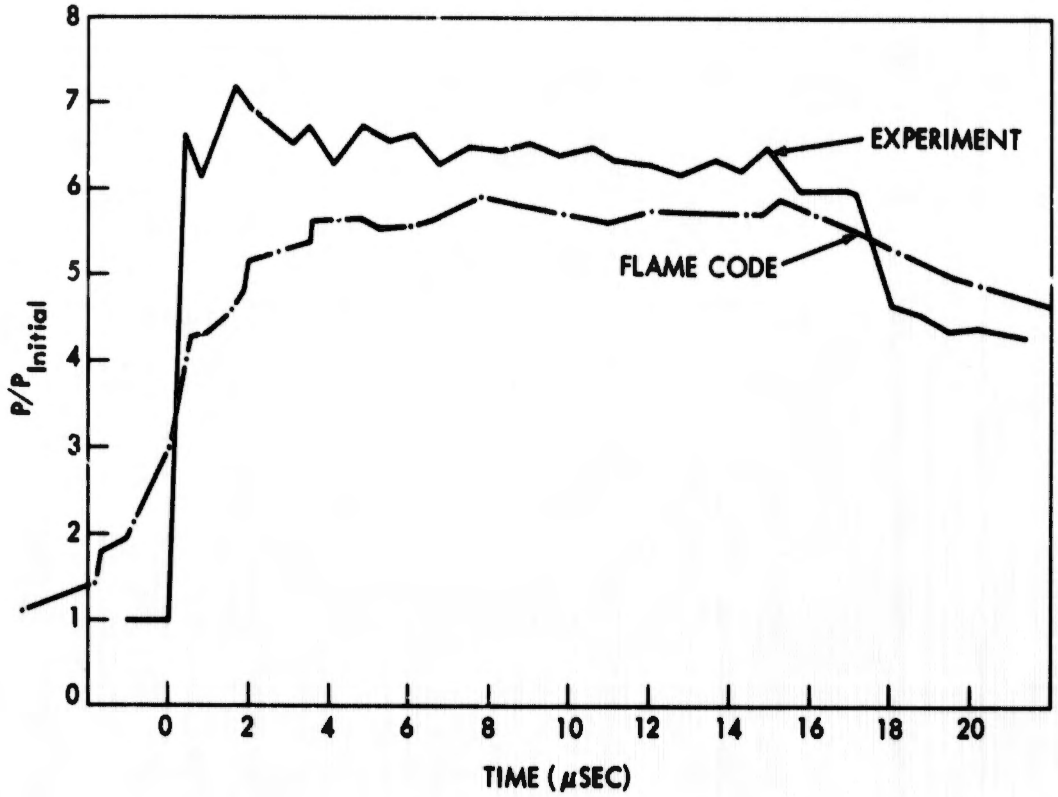

K. $M_1 = 3.07$, $M_s = 1.88$ (RUN 795)

FIG. 14 SHOCK-INDUCED PRESSURE-TIME VARIATION AT THE STAGNATION POINT OF A 3-INCH DIAMETER HEMISPHERE (CONTINUED)

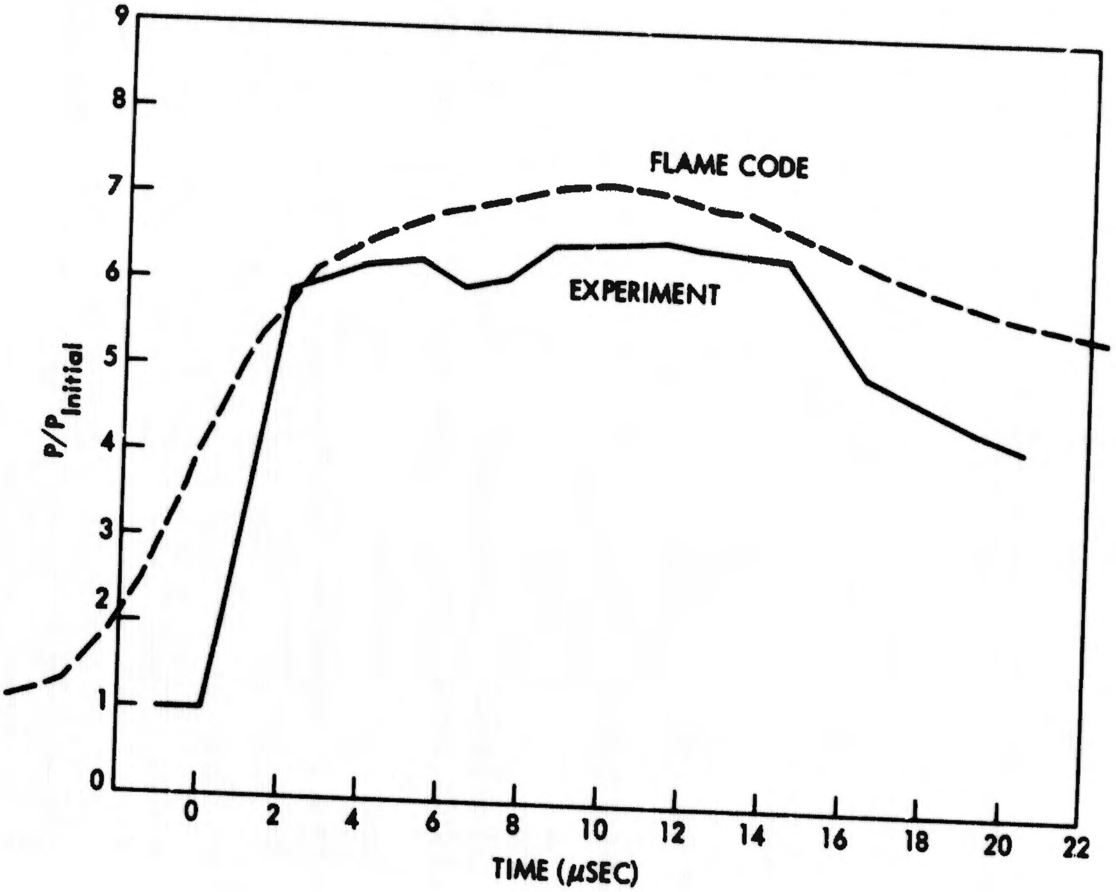

A. $M_1 = 5.07$, $M_s = 2.2$ (RUN 447)

FIG. 15 SHOCK-INDUCED PRESSURE-TIME VARIATION AT THE 45-DEGREE STATION OF A 3-INCH DIAMETER HEMISPHERE

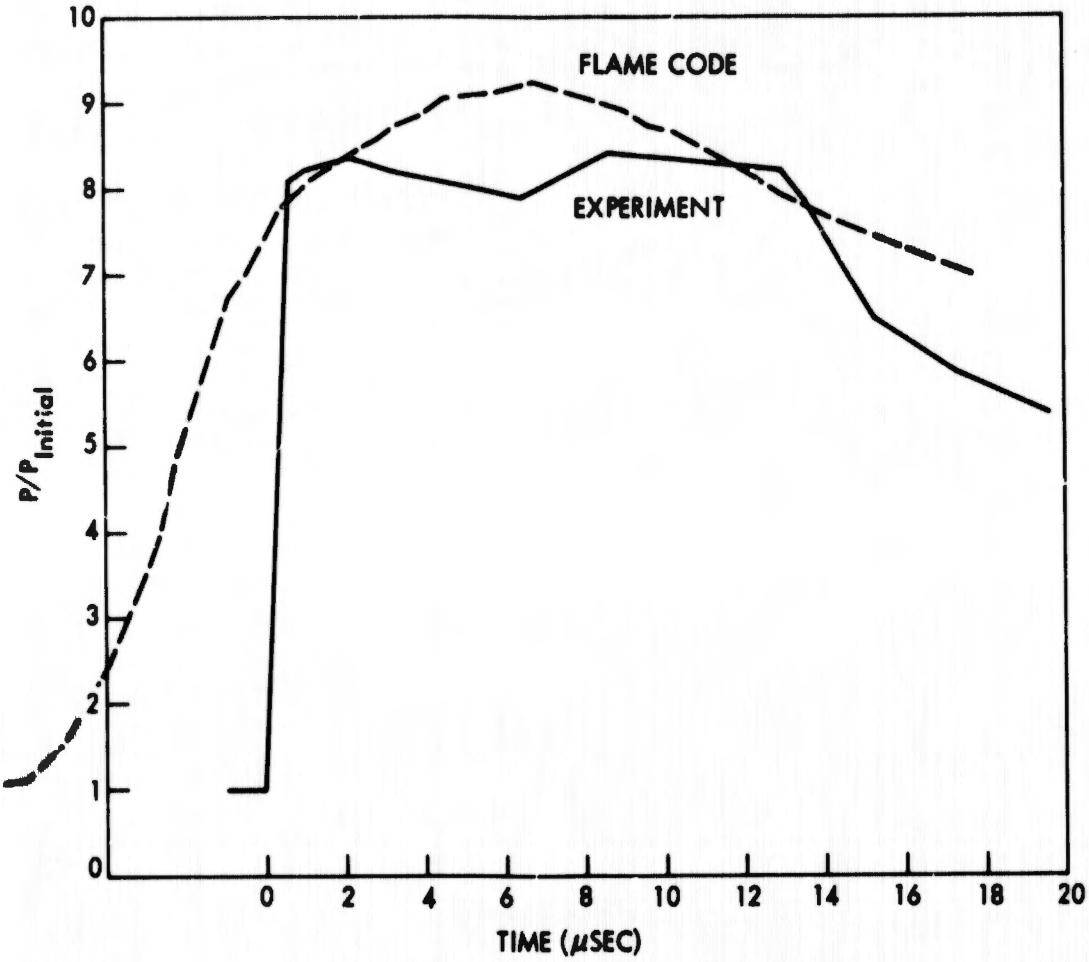

B. $M_1 = 5.07$, $M_s = 2.50$ (RUN 448)

FIG. 15 SHOCK-INDUCED PRESSURE-TIME VARIATION AT THE 45-DEGREE STATION OF A 3-INCH DIAMETER HEMISPHERE (CONTINUED)

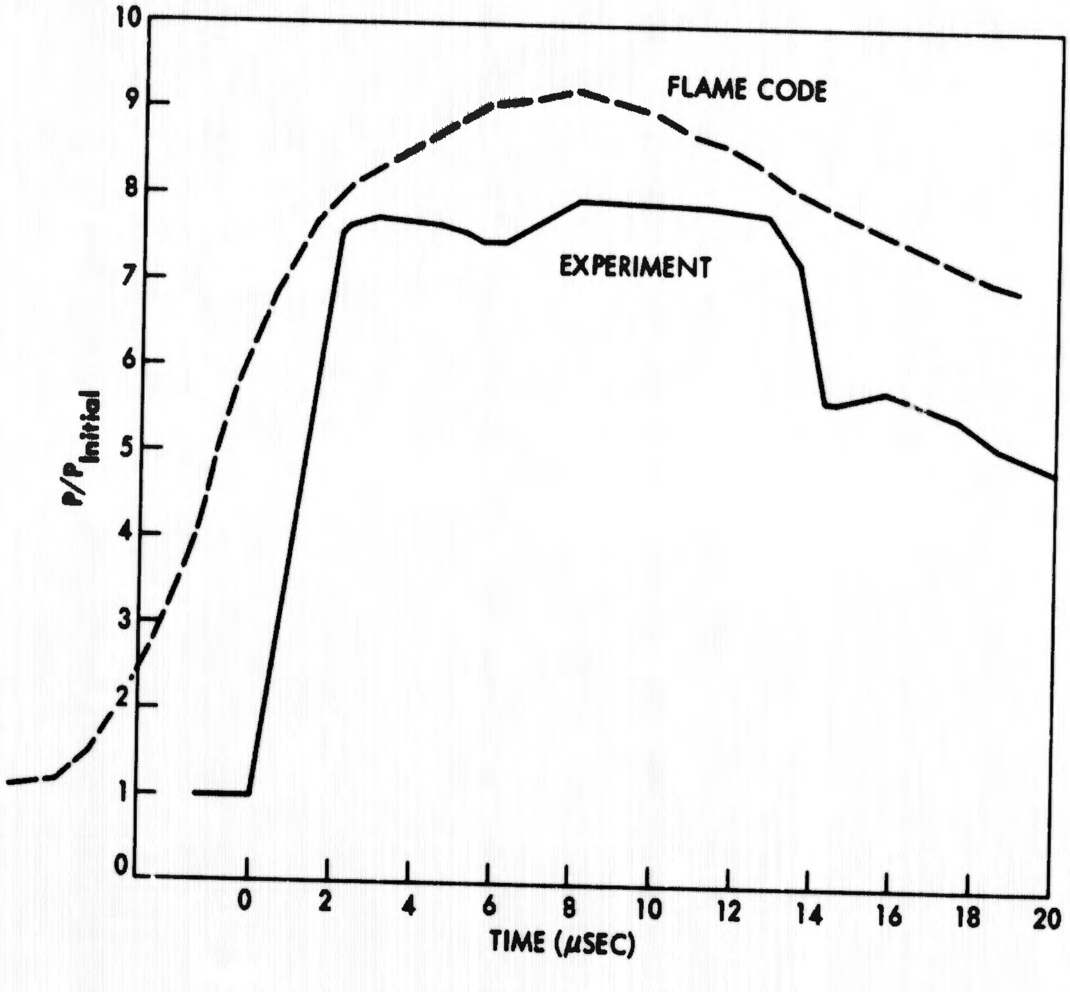

C. $M_1 = 5.07$, $M_s = 2.5$ (RUN 505)

FIG. 15 SHOCK-INDUCED PRESSURE-TIME VARIATION AT THE 45-DEGREE STATION OF A 3-INCH DIAMETER HEMISPHERE (CONTINUED)

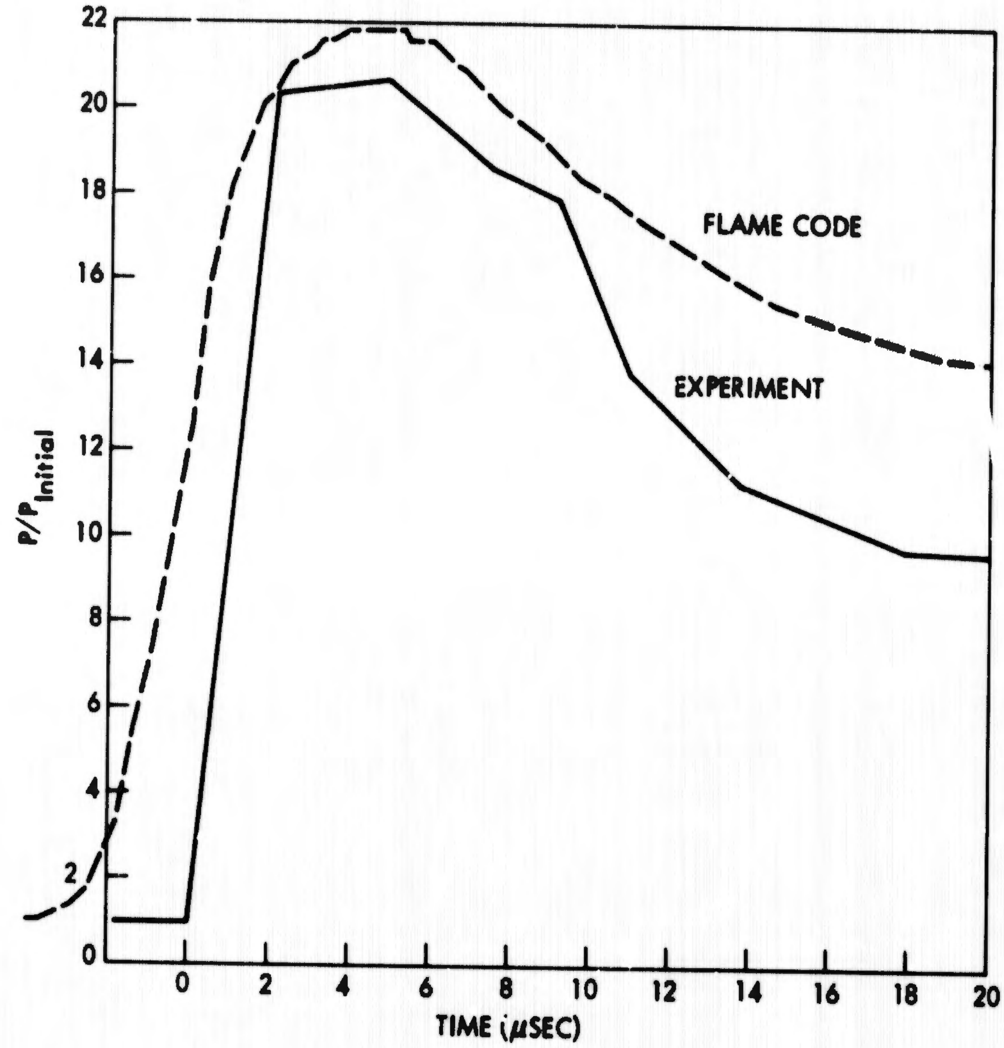

D. $M_1 = 5.05$, $M_s = 4.27$ (RUN 455)

FIG. 15 SHOCK-INDUCED PRESSURE-TIME VARIATION AT THE 45-DEGREE STATION OF A 3-INCH DIAMETER HEMISPHERE (CONTINUED)

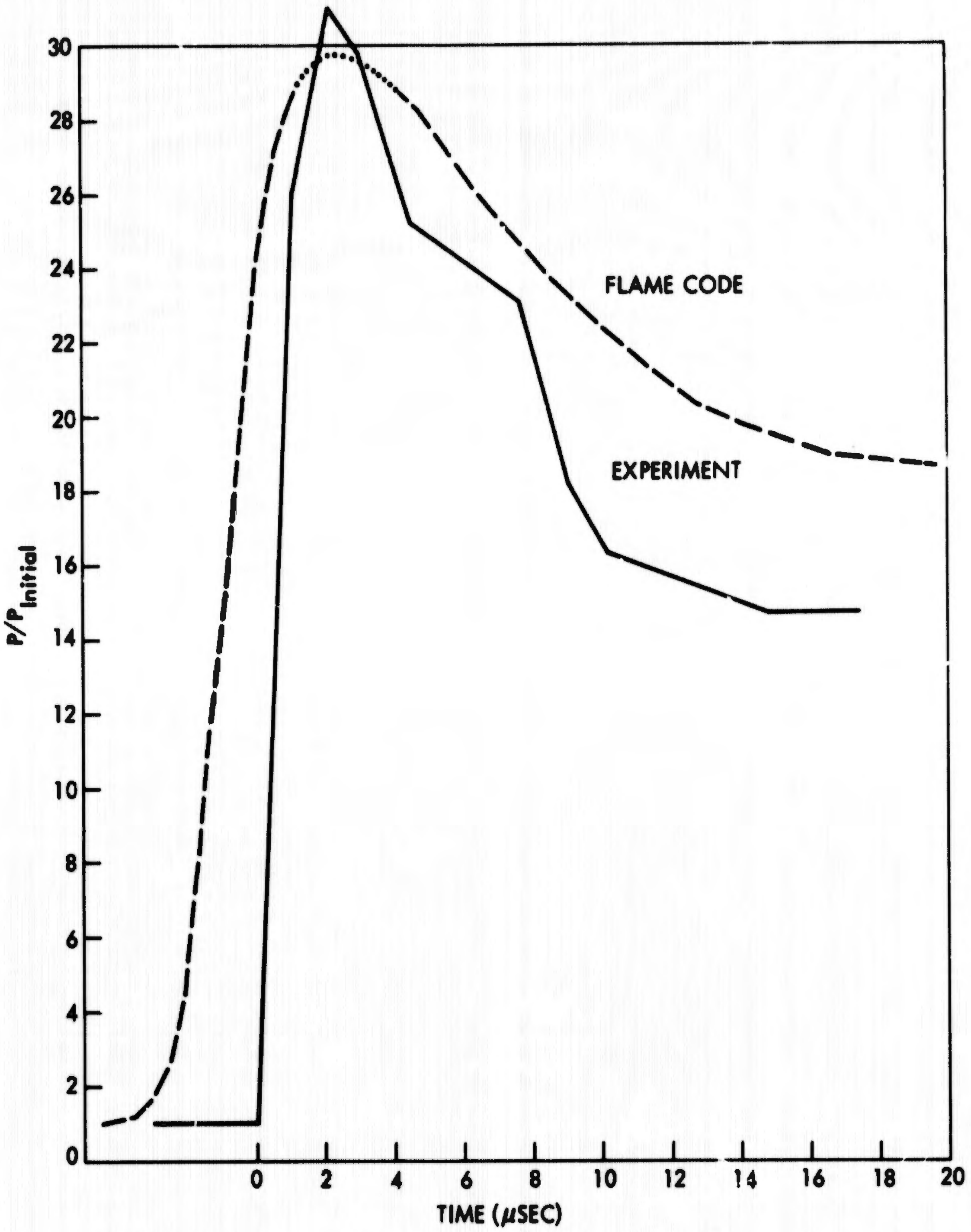

E. $M_1 = 5.07$, $M_s = 5.25$ (RUN 127)

FIG. 15 SHOCK-INDUCED PRESSURE-TIME VARIATION AT THE 45-DEGREE STATION OF A 3-INCH DIAMETER HEMISPHERE (CONTINUED)

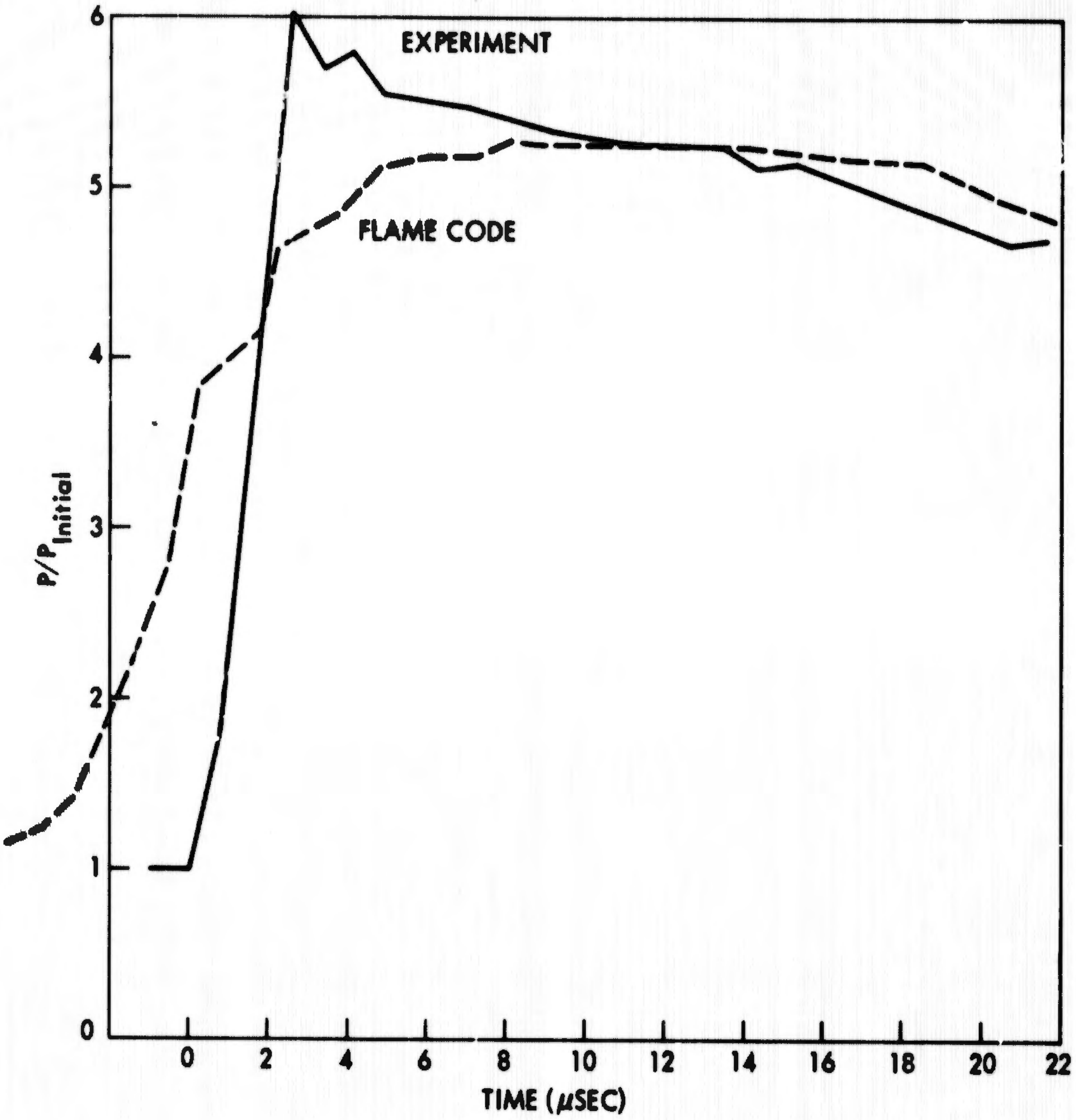

F. $M_1 = 3.09$, $M_s = 1.84$ (RUN 135)

FIG. 15 SHOCK-INDUCED PRESSURE-TIME VARIATION AT THE 45-DEGREE STATION OF A 3-INCH DIAMETER HEMISPHERE (CONTINUED)

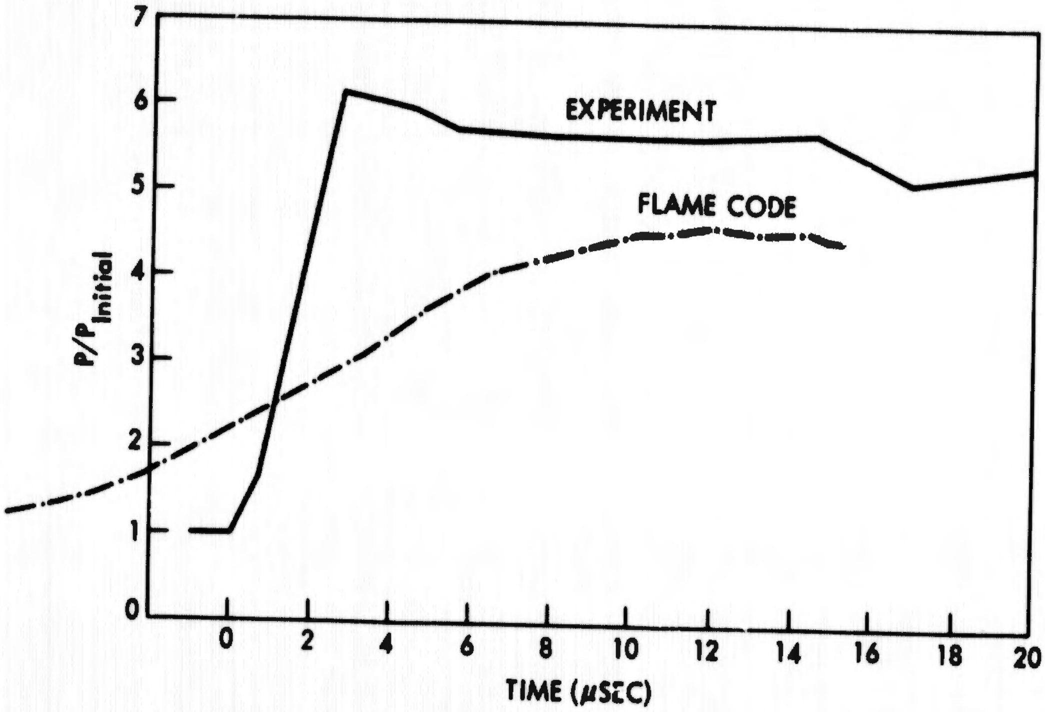

A. $M_1 = 5.07$, $M_s = 2.5$ (RUN 448)

FIG. 16 SHOCK-INDUCED PRESSURE-TIME VARIATION AT THE 90-DEGREE STATION OF A 3-INCH DIAMETER HEMISPHERE

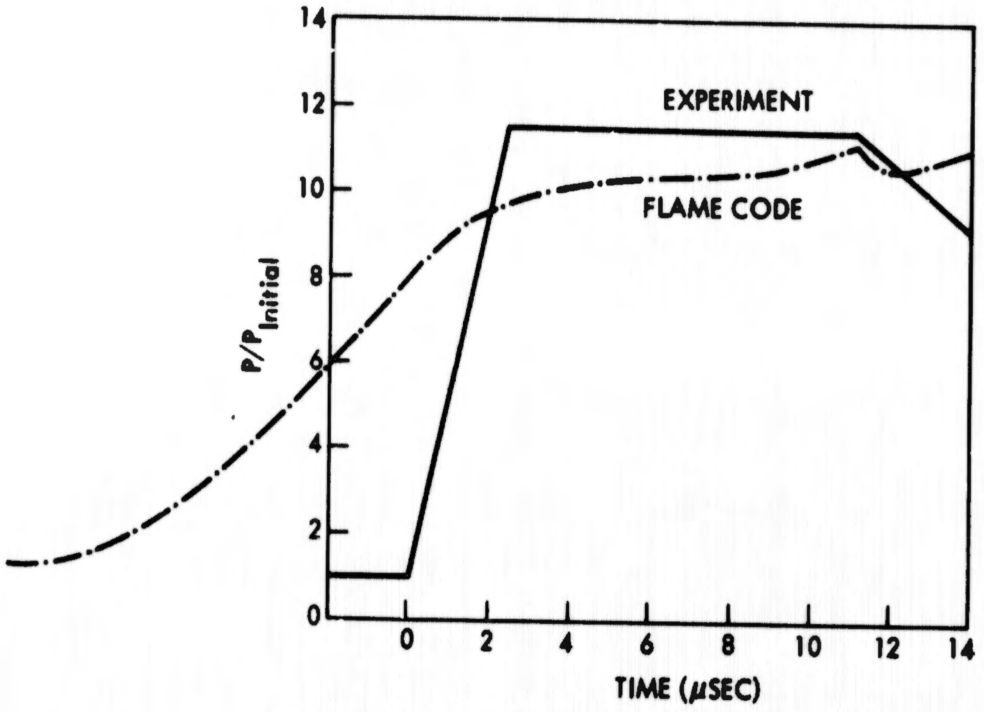

B. $M_1 = 5.05$, $M_s = 4.27$ (RUN 455)

FIG. 16 SHOCK-INDUCED PRESSURE-TIME VARIATION AT THE 90-DEGREE STATION OF A 3-INCH DIAMETER HEMISPHERE (CONTINUED)

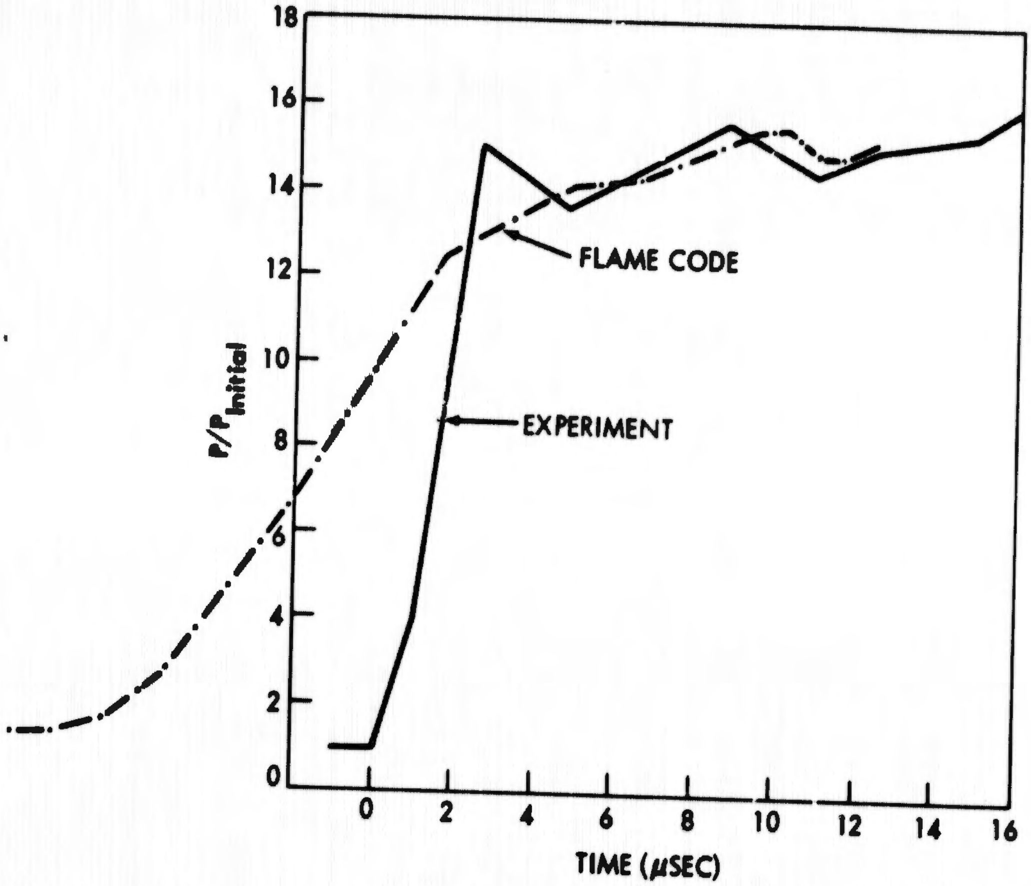

C. $M_1 = 5.07$, $M_s = 5.25$ (RUN 127)

FIG. 16 SHOCK-INDUCED PRESSURE-TIME VARIATION AT THE 90-DEGREE STATION OF A 3-INCH DIAMETER HEMISPHERE (CONTINUED)

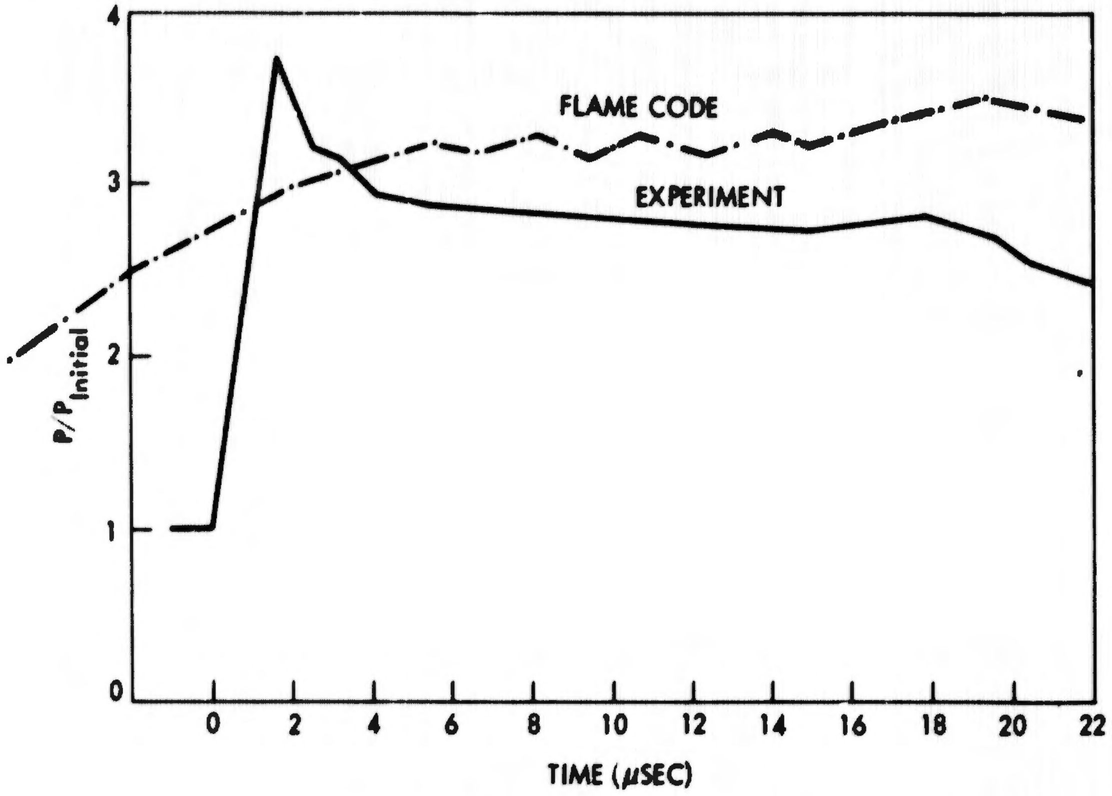

D. $M_1 = 3.07$, $M_s = 1.83$ (RUN 793)

FIG. 16 SHOCK-INDUCED PRESSURE-TIME VARIATION AT THE 90-DEGREE STATION OF A 3-INCH DIAMETER HEMISPHERE (CONTINUED)

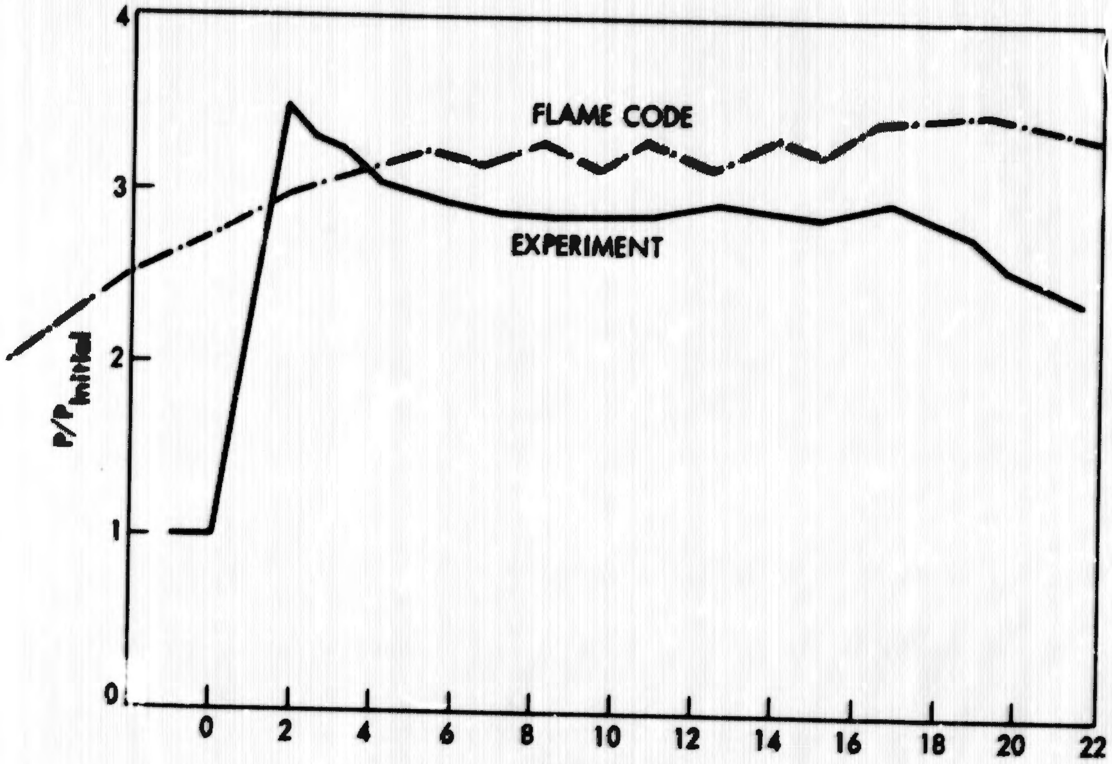

E. $M_1 = 3.07$, $M_s = 1,88$ (RUN 795)

FIG. 16 SHOCK-INDUCED PRESSURE-TIME VARIATION AT THE 90-DEGREE STATION OF A 3-INCH DIAMETER HEMISPHERE (CONTINUED)

A. $M_1 = 5.05$ $M_s = 4.3$

FIG. 17 TWO-SPARK SHADOW PHOTOGRAPH OF THE SHOCK INTERACTION FIELD FOR A HEMISPHERE

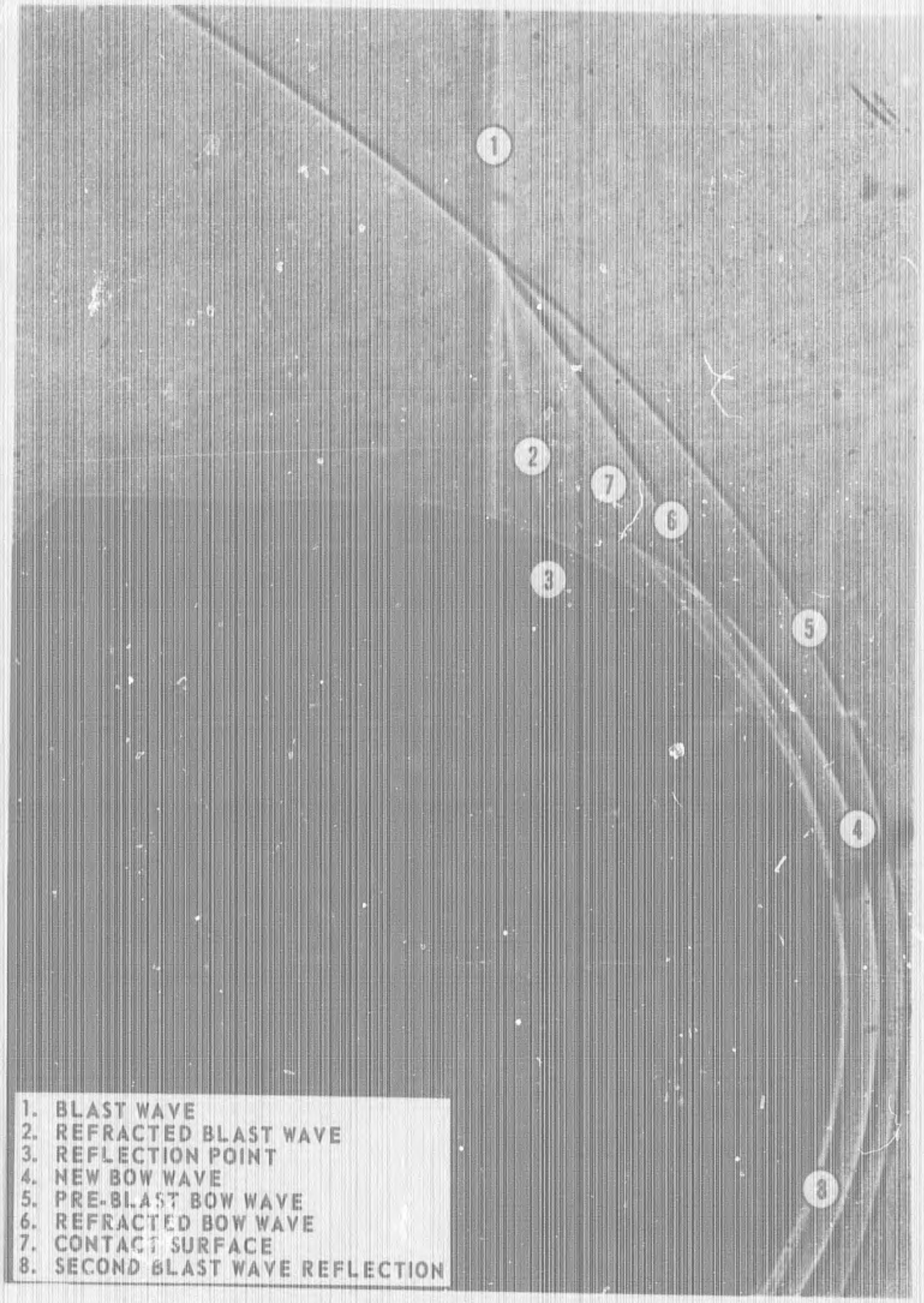

B. $M_1 = 5.07$ $M_s = 2.2$

FIG. 17 TWO-SPARK SHADOW PHOTOGRAPH OF THE SHOCK INTERACTION FIELD FOR A HEMISPHERE (CONTINUED)

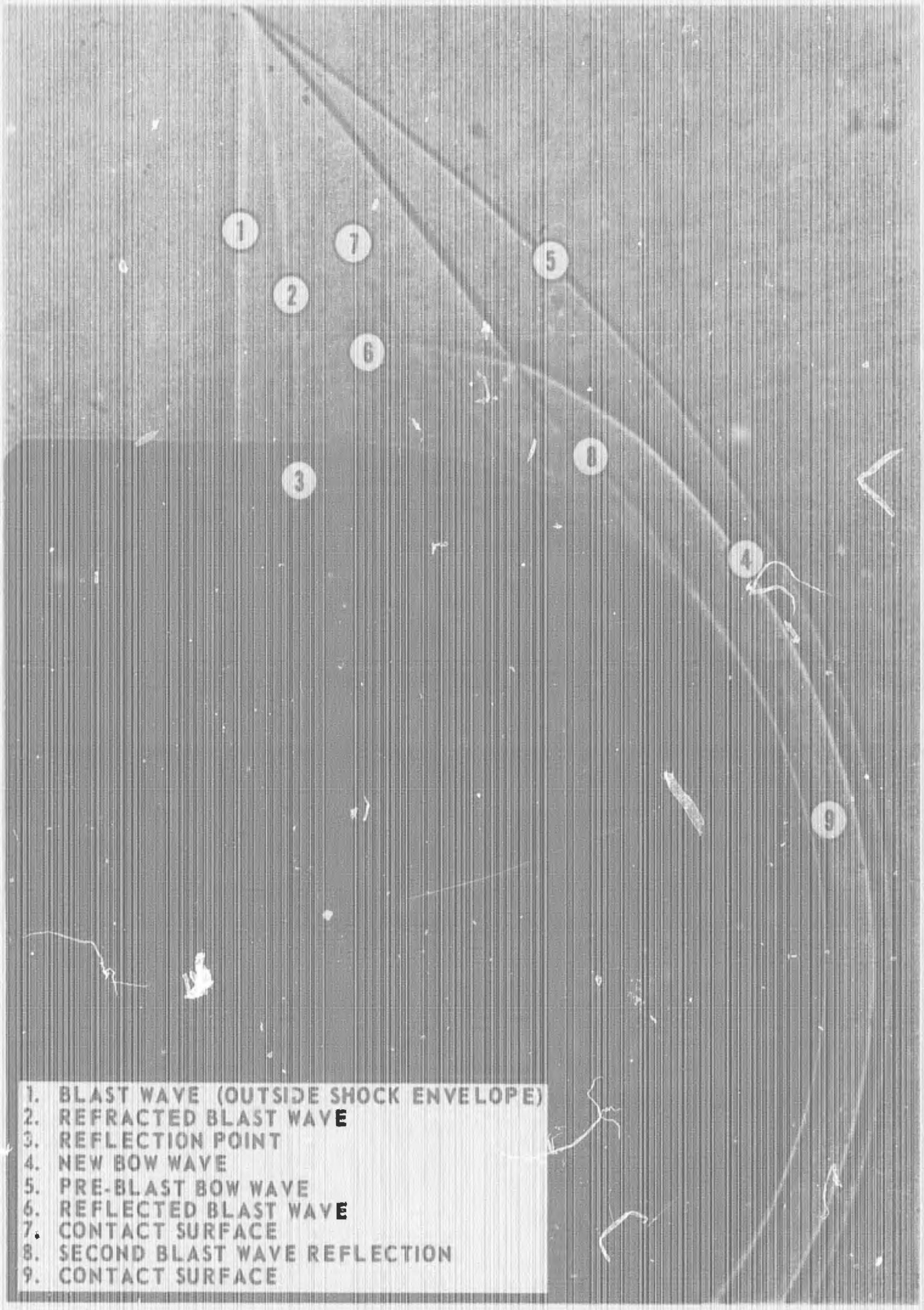

C. $M_1 = 5.05$ $M_s = 2.35$

FIG. 17 TWO-SPARK SHADOW PHOTOGRAPH OF THE SHOCK INTERACTION FIELD FOR A HEMISPHERE (CONTINUED)

APPENDIX

Supplementary Data on Test Flow Conditions, Pressure Transducer and Shock Interaction Characteristics

BLANK PAGE

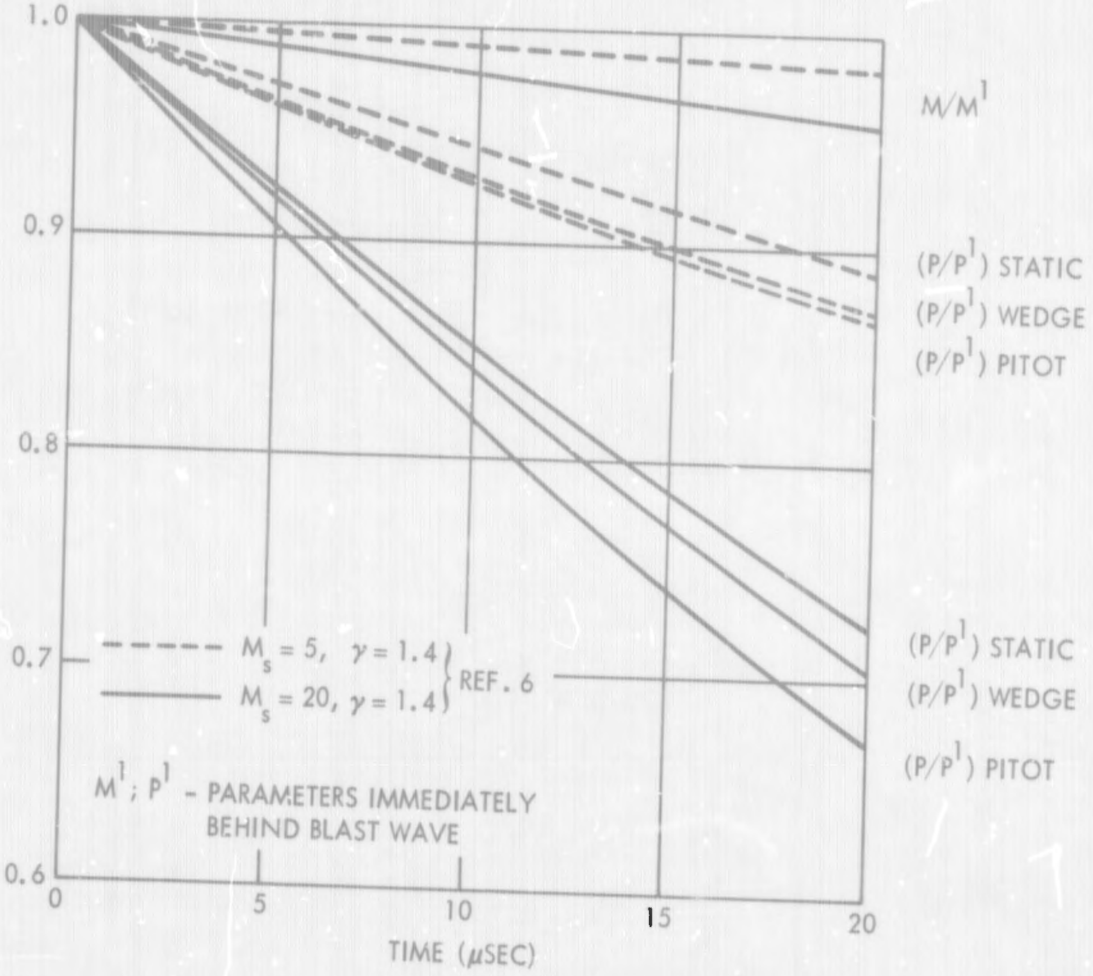

A. CALCULATED (REF 6)

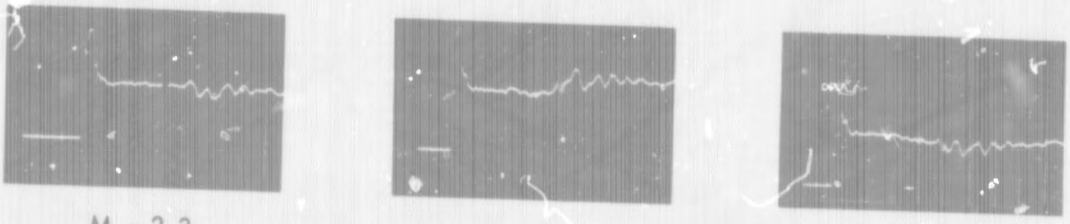

$M_s = 2.3$ $M_s = 5$ $M_s = 5.2$

B. MEASURED WITH A 0.13-INCH DIAMETER PITOT PROBE. SWEEP RATE 5 μSEC/CM FOR ALL TRACES

FIG. A-1 VARIATION IN FLOW PARAMETERS BEHIND A BLAST WAVE FOR A 5-FOOT LONG CONICAL MACH 5 NOZZLE

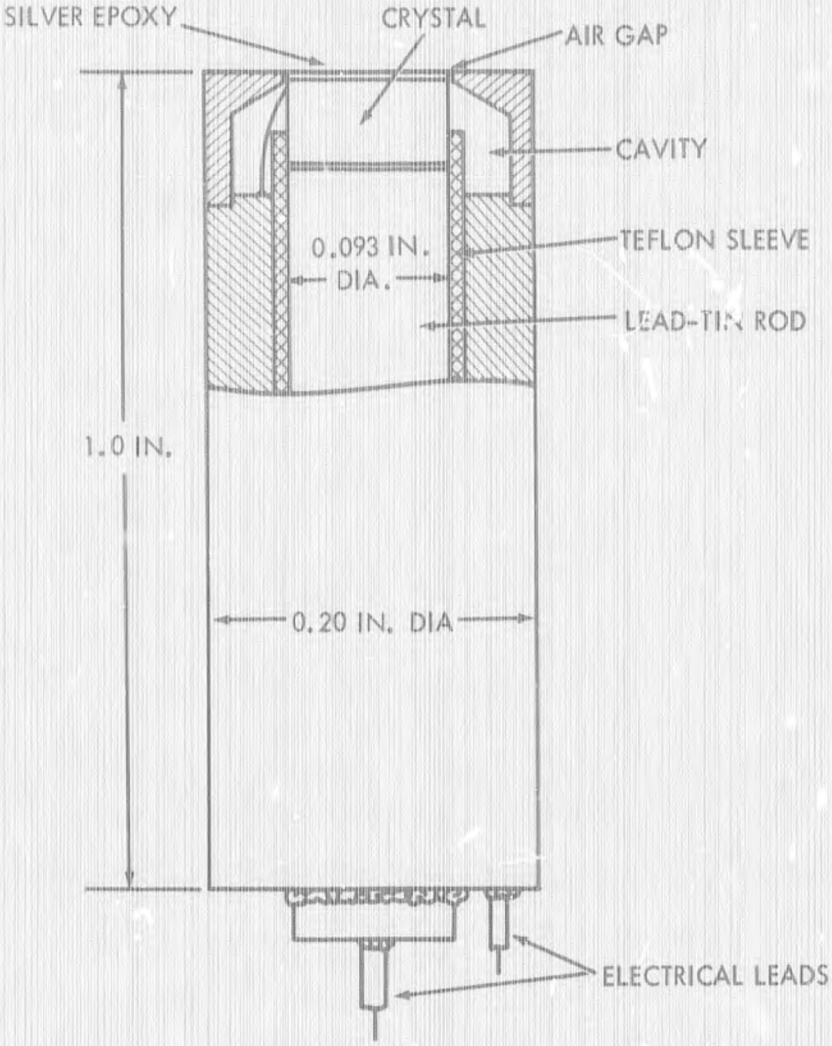

FIG. A-2 SCHEMATIC ILLUSTRATION OF THE NOL PRESSURE TRANSDUCER

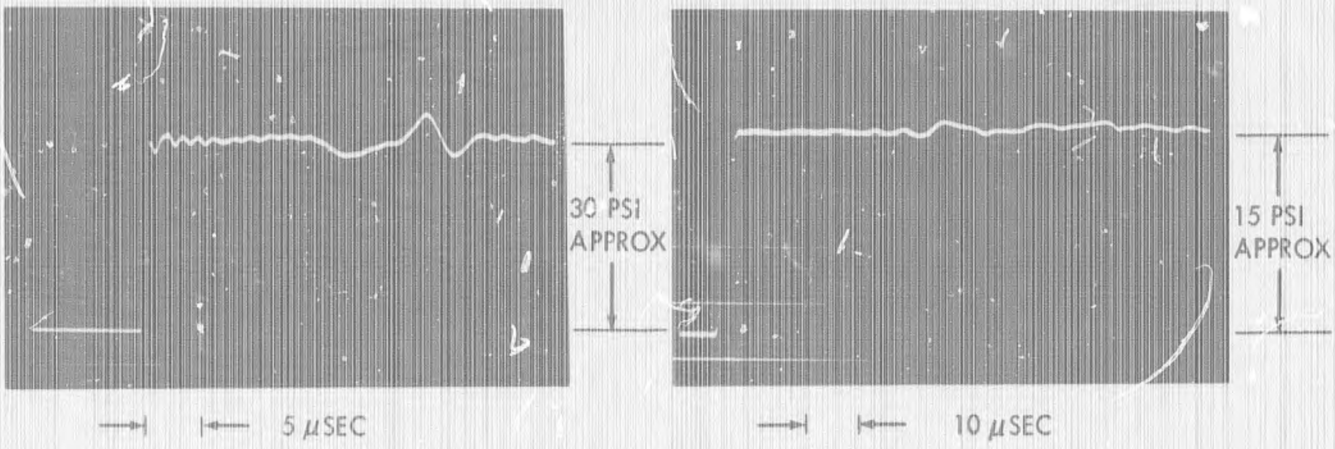

REFLECTED SHOCK LOADING

INCIDENT SHOCK LOADING

FIG. A-3 TYPICAL TRANSDUCER CALIBRATION PRESSURE TRACES

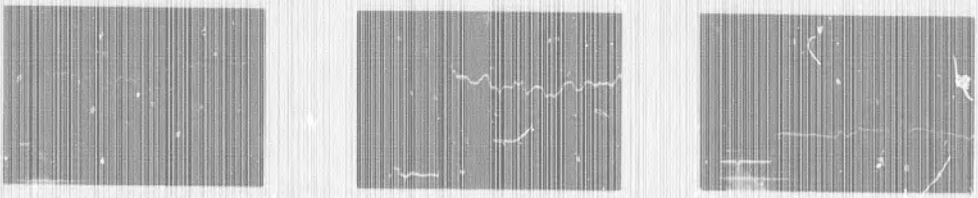

→| |← 10 μSEC (TRACES A THROUGH F)

A. 9° CONE $M_s = 5.0$

B. 9° CONE $M_s = 3.9$

C. 9° CONE $M_s = 2.3$

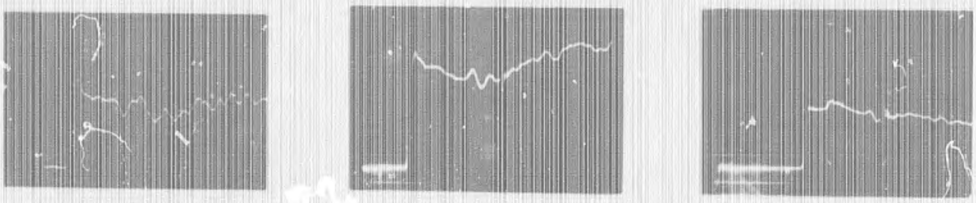

D. 15° CONE $M_s = 4.45$

E. 15° CONE $M_s = 4.4$

F. 15° CONE $M_s = 2.4$

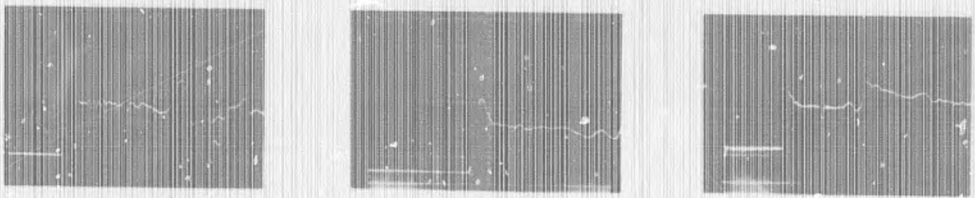

→| |← 5 μSEC

G. 30° CONE $M_s = 4.82$

→| |← 5 μSEC

H. 30° CONE $M_s = 4.14$

→| |← 10 μSEC

I. 30° CONE $M_s = 1.7$

FIG. A-4 TYPICAL PRESSURE-TIME TRACES FOR CONES OF DIFFERENT SEMIVERTEX ANGLES. ALL TRACES AT A FREE-STREAM MACH NUMBER OF 5.1

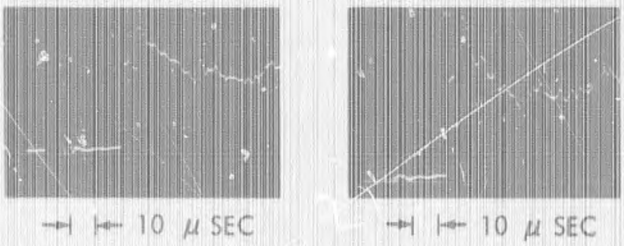

A. $M_s = 3.9$ B. $M_s = 4.5$

FIG. A-5 TYPICAL PRESSURE-TIME TRACES FOR A SPHERICALLY BLUNTED 9° CONE AT A FREE-STREAM MACH NO. 5.1

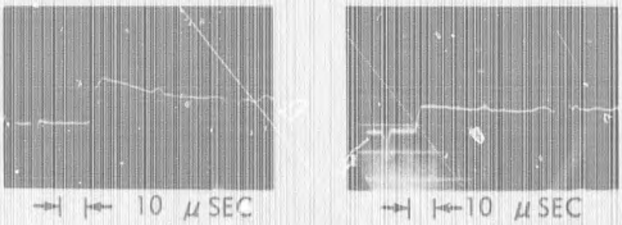

A. $M_s = 3.43$ B. $M_s = 2.65$

FIG. A-6 TYPICAL PRESSURE-TIME TRACES FOR A 9° CONE AT A FREE-STREAM MACH NO. 6.9

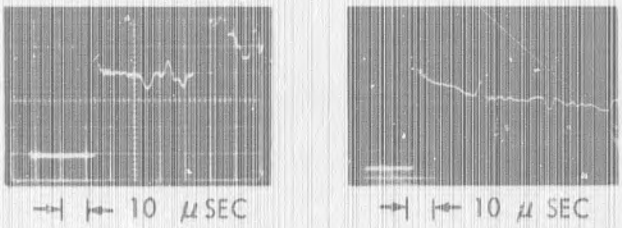

A. $M_s = 1.77$ B. $M_s = 1.59$

FIG. A-7 TYPICAL PRESSURE-TIME TRACES FOR A 9° CONE AT A FREE-STREAM MACH NO. 3.1

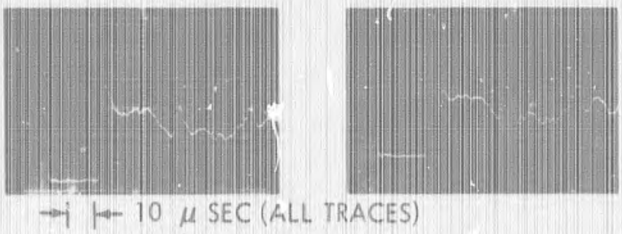

A. $\alpha = 10^\circ$, $M_s = 4.09$ B. $\alpha = 20^\circ$, $M_s = 4.16$

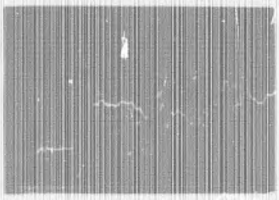

C. $\alpha = 30^\circ$, $M_s = 4.40$

FIG. A-8 TYPICAL PRESSURE-TIME TRACES FOR A 9° CONE AT DIFFERENT ANGLES OF ATTACK. FREE-STREAM MACH NO. 5.1; WINDWARD SURFACE.

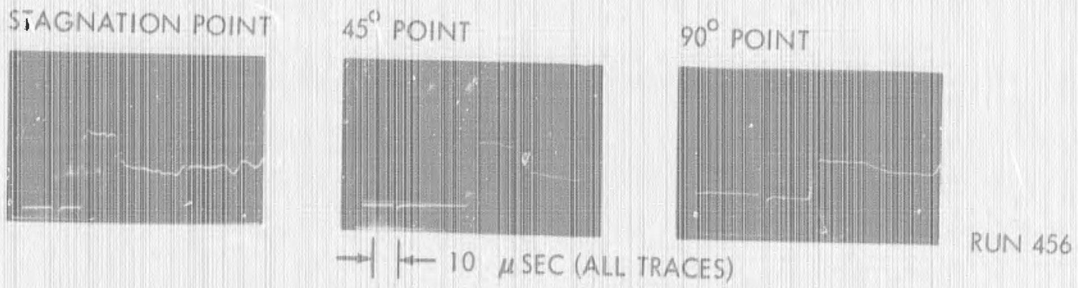

A. $M_1 = 5.1$, $M_s = 4.44$

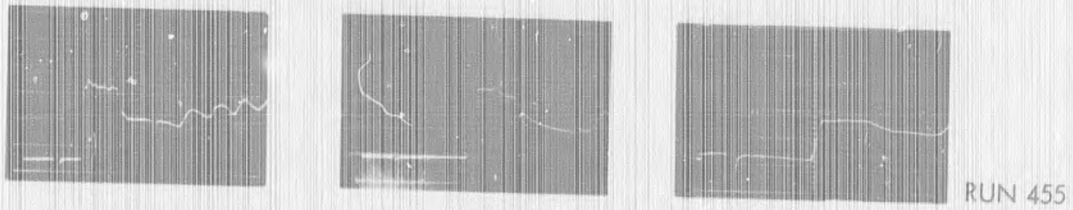

B. $M_1 = 5.1$, $M_s = 4.27$

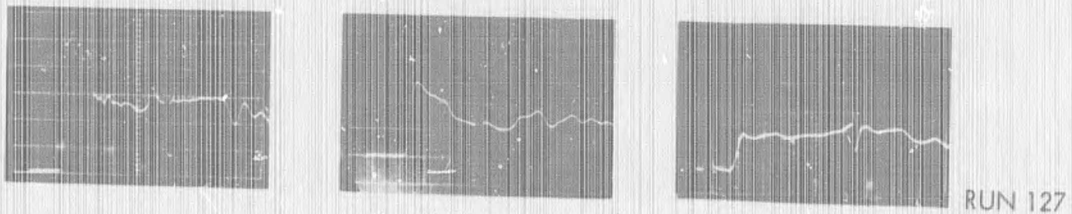

C. $M_1 = 5.1$, $M_s = 5.25$

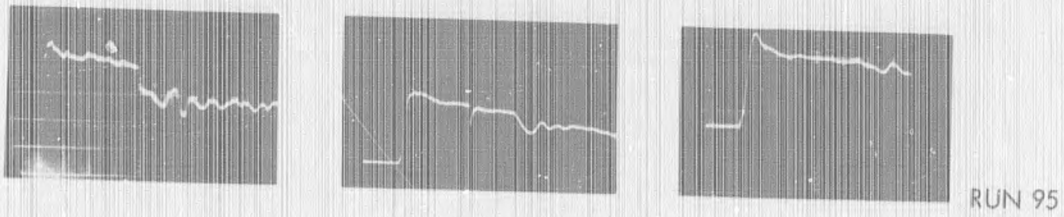

D. $M_1 = 3.1$, $M_s = 1.68$

FIG. A-9 TYPICAL PRESSURE-TIME TRACES FOR THE THREE-INCH DIAMETER HEMISPHERE

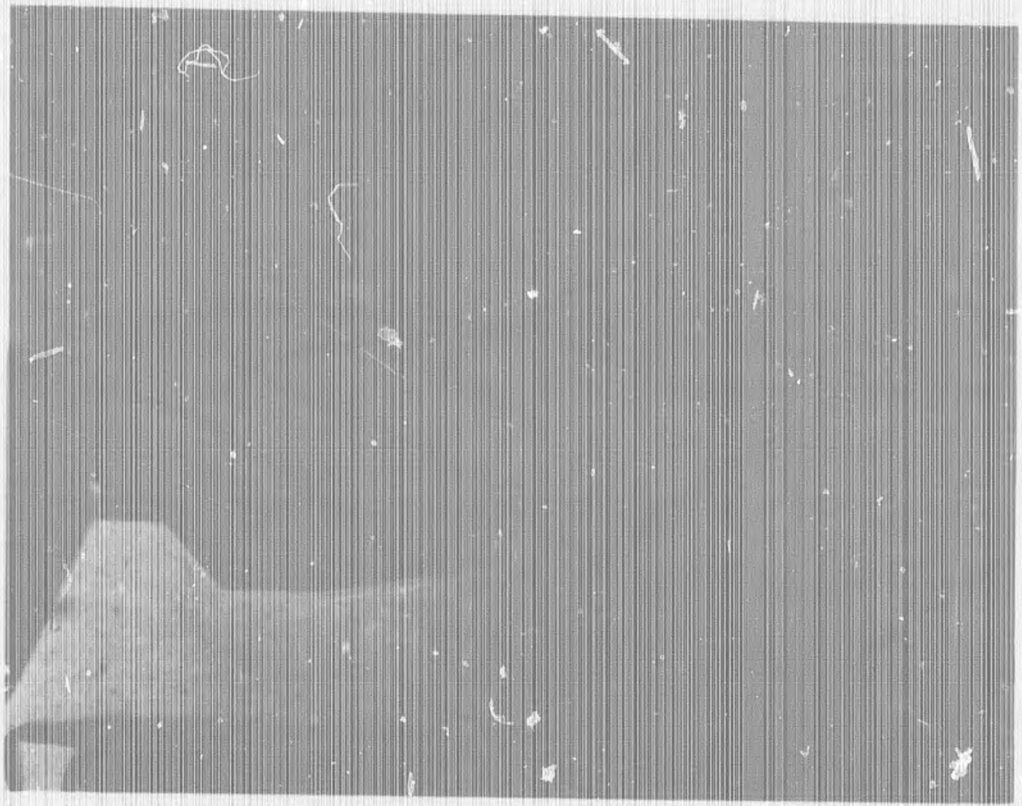

A. $M_s = 2.21$ (RUN 277)

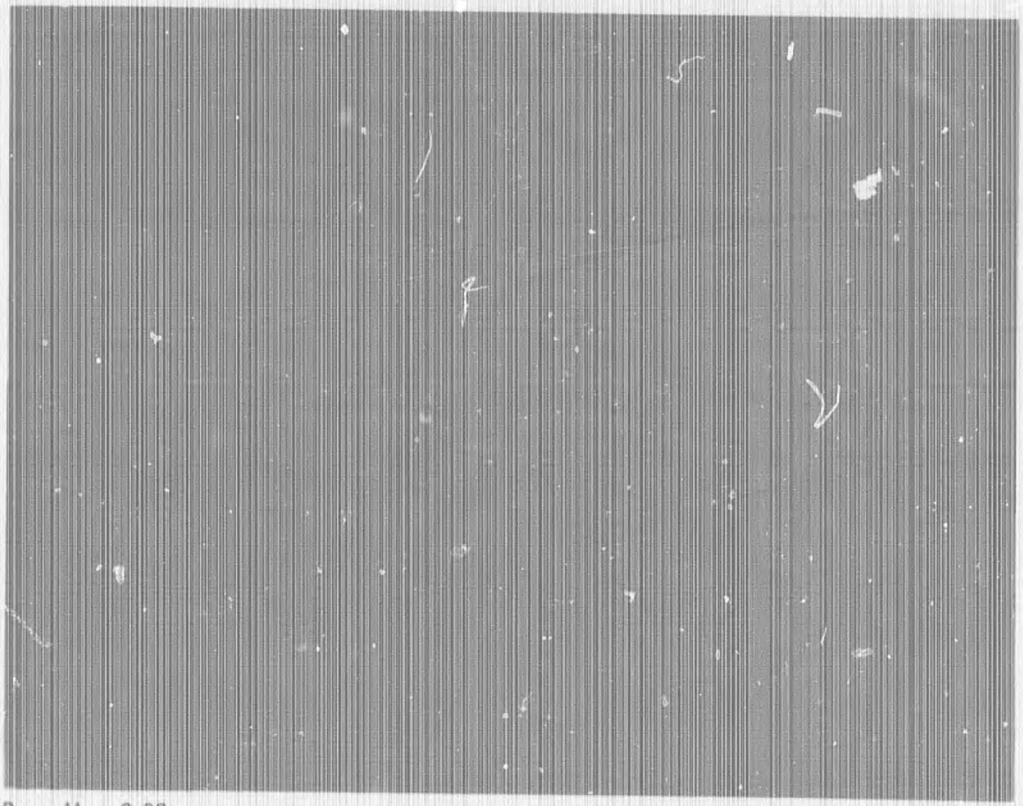

B. $M_s = 2.32$ (RUN 236)

FIG. A-10 TWO-SPARK SHADOW PHOTOGRAPHS OF THE SHOCK INTERACTION FIELD; 9^0 CONE AT FREE-STREAM MACH 5.1

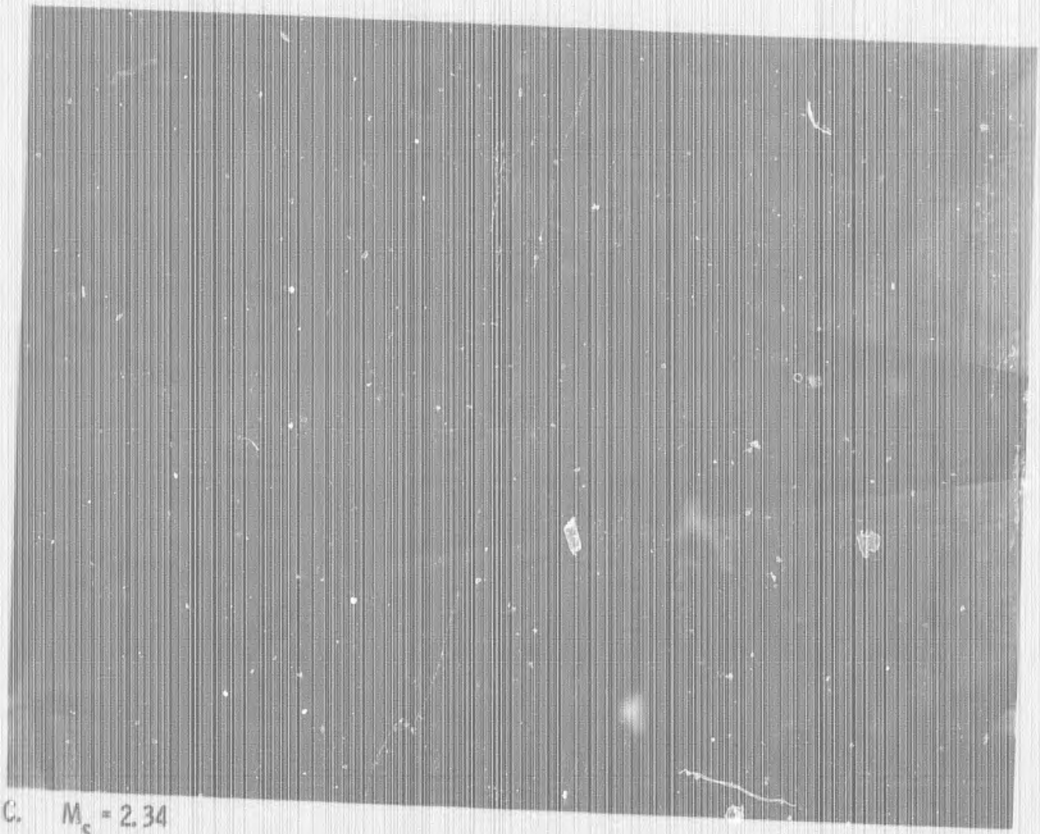

C. $M_s = 2.34$

(RUN 237)

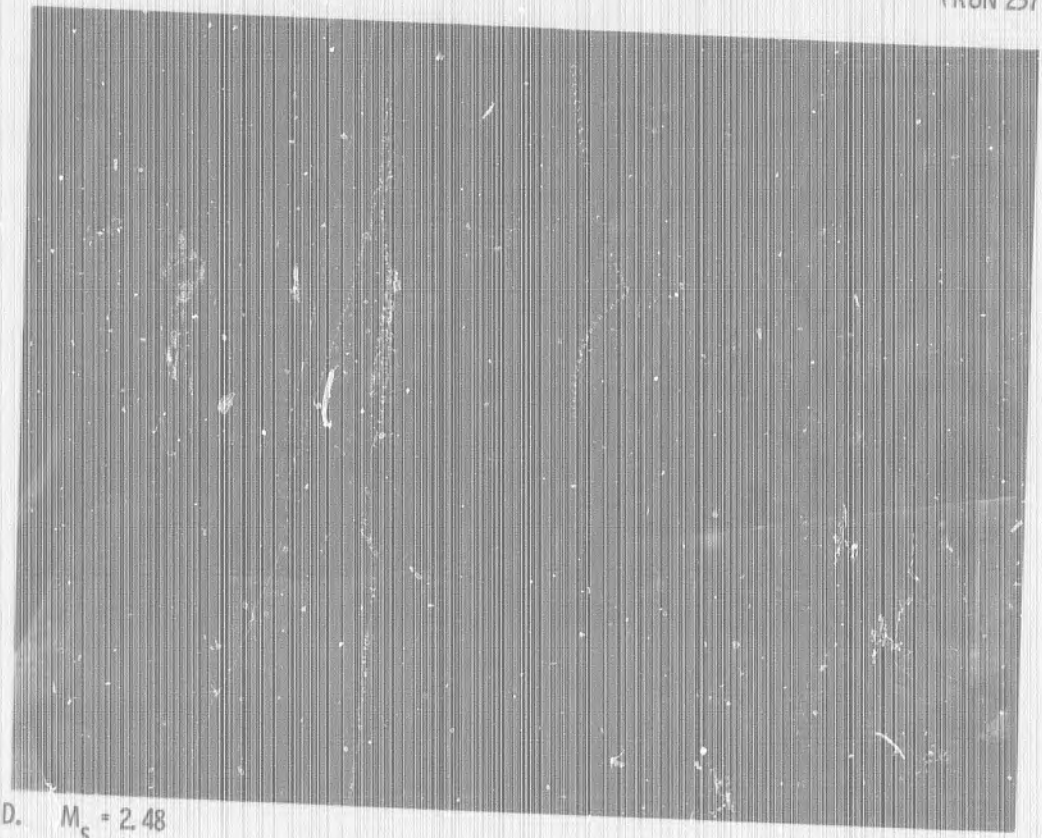

D. $M_s = 2.48$

(RUN 418)

FIG. A-10 TWO-SPARK SHADOW PHOTOGRAPHS OF THE SHOCK INTERACTION FIELD; 9° CONE AT FREE-STREAM MACH 5.1 (CONTINUED)

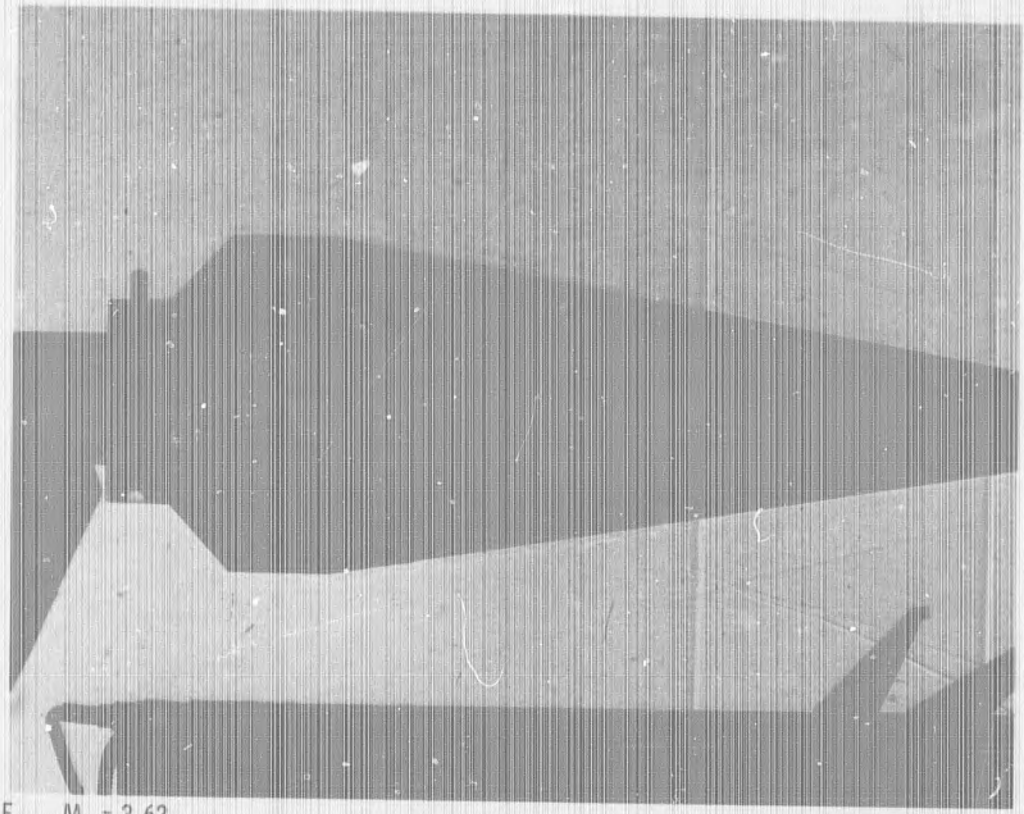

E. $M_s = 2.62$ (RUN 421)

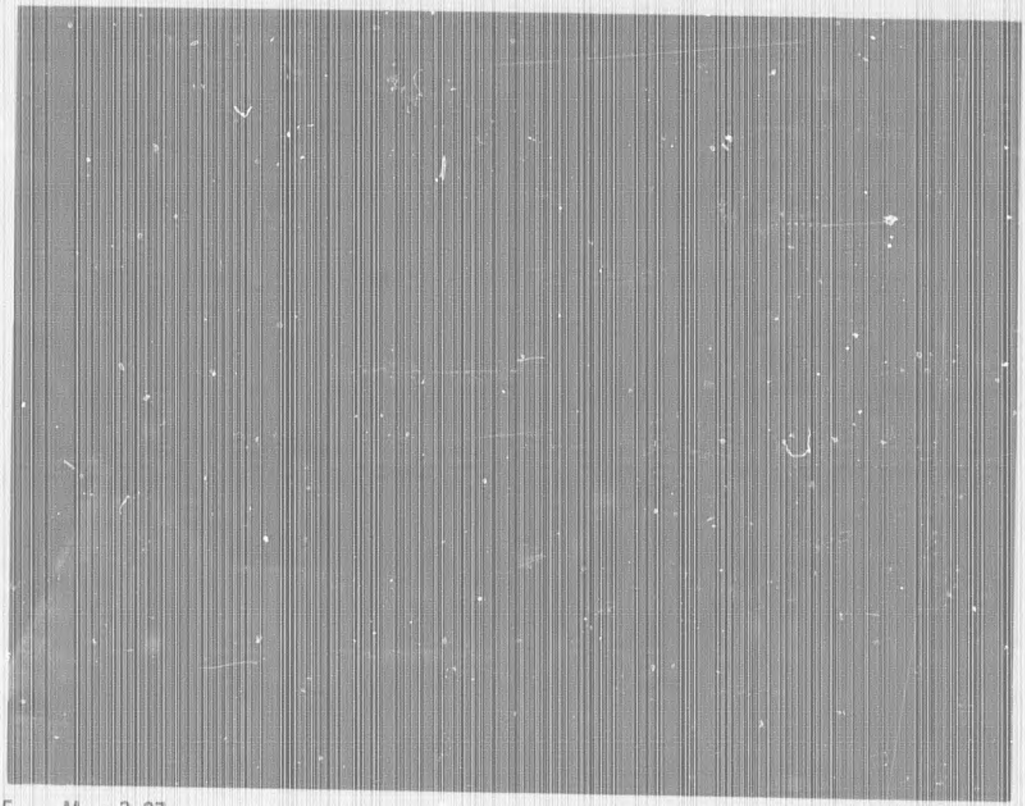

F. $M_s = 3.97$ (RUN 280)

FIG. A-10 TWO-SPARK SHADOW PHOTOGRAPHS OF THE SHOCK INTERACTION FIELD; 9^0 CONE AT FREE-STREAM MACH 5.1 (CONTINUED)

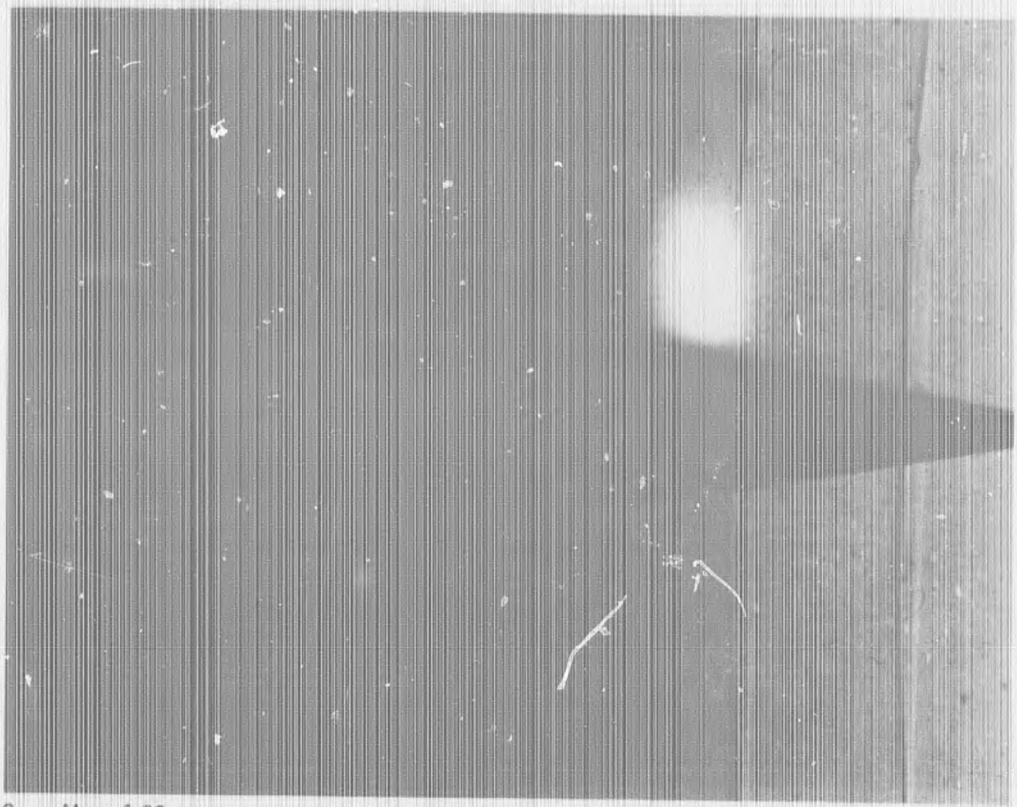

G. $M_s = 4.32$ (RUN 736)

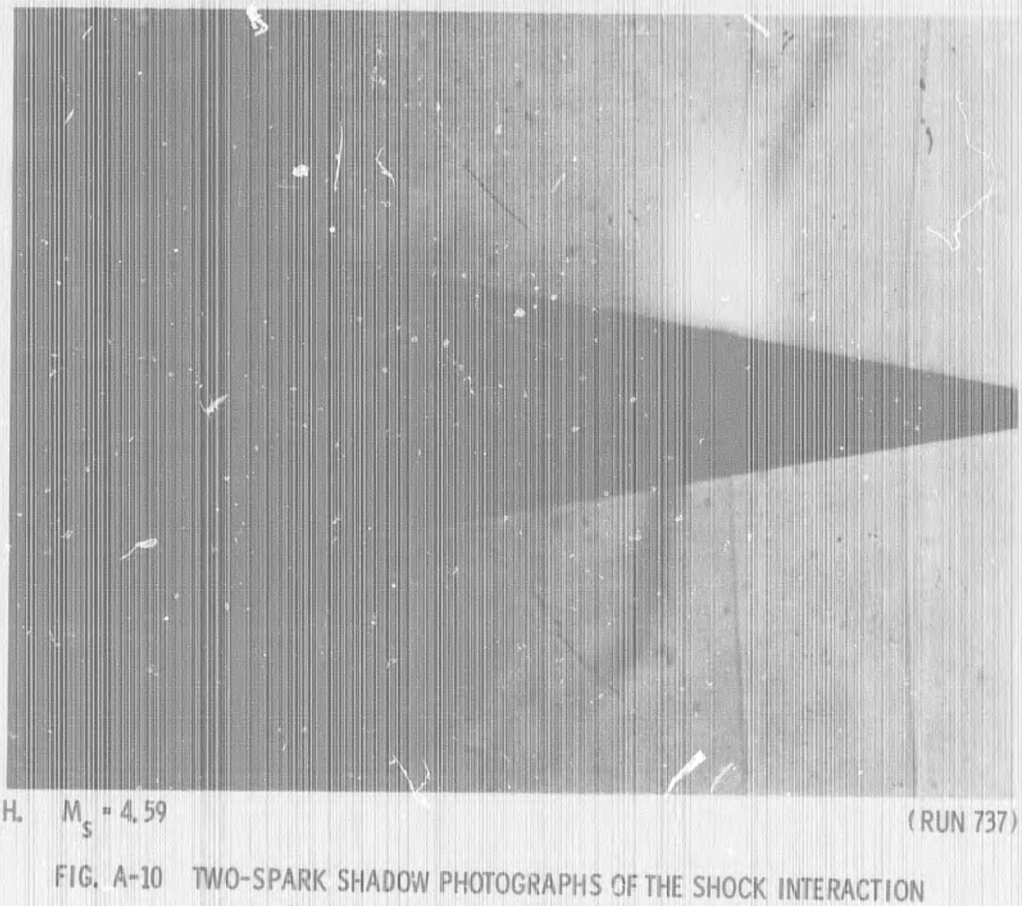

H. $M_s = 4.59$ (RUN 737)

FIG. A-10 TWO-SPARK SHADOW PHOTOGRAPHS OF THE SHOCK INTERACTION FIELD; 9° CONE AT FREE-STREAM MACH 5.1 (CONTINUED)

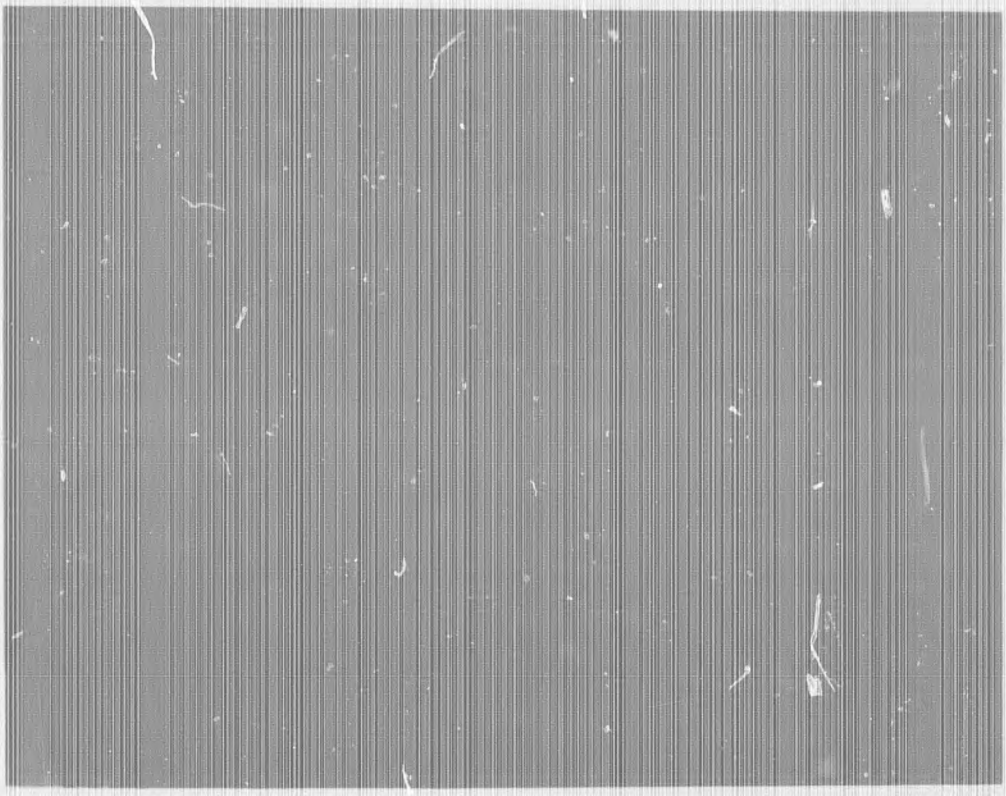

I. $M_s = 4.62$ (RUN 432)

J. $M_s = 4.76$ (RUN 287)

FIG. A-10 TWO-SPARK SHADOW PHOTOGRAPHS OF THE SHOCK INTERACTION FIELD; 9° CONE AT FREE-STREAM MACH 5.1 (CONTINUED)

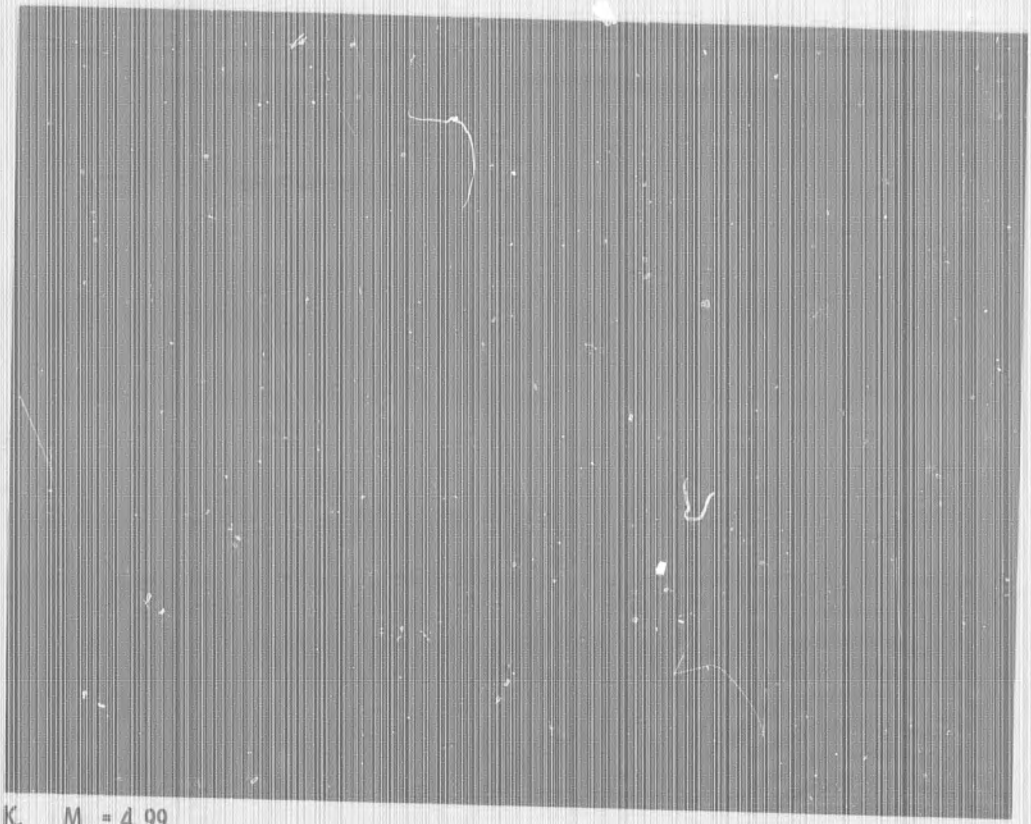

K. $M_s = 4.99$ (RUN 283)

L. $M_s = 5.37$ (RUN 190)

FIG. A-10 TWO-SPARK SHADOW PHOTOGRAPHS OF THE SHOCK INTERACTION FIELD; 9^0 CONE AT FREE-STREAM MACH 5.1 (CONTINUED)

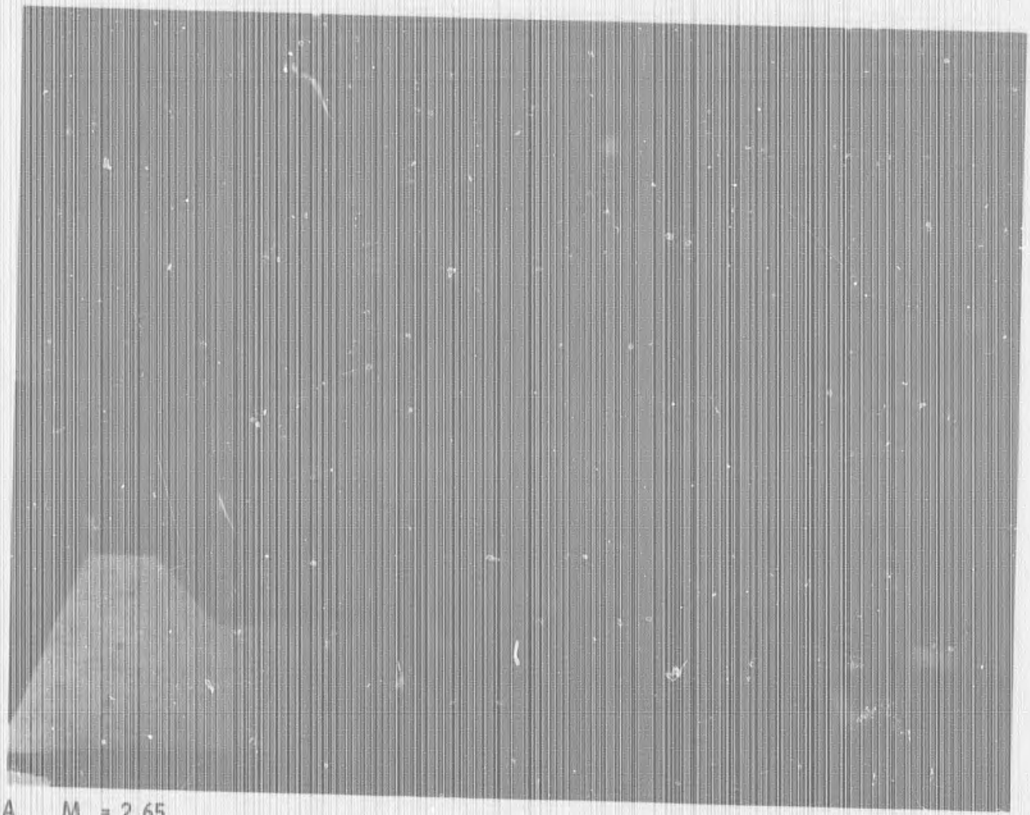

A. $M_s = 2.65$ (RUN 384)

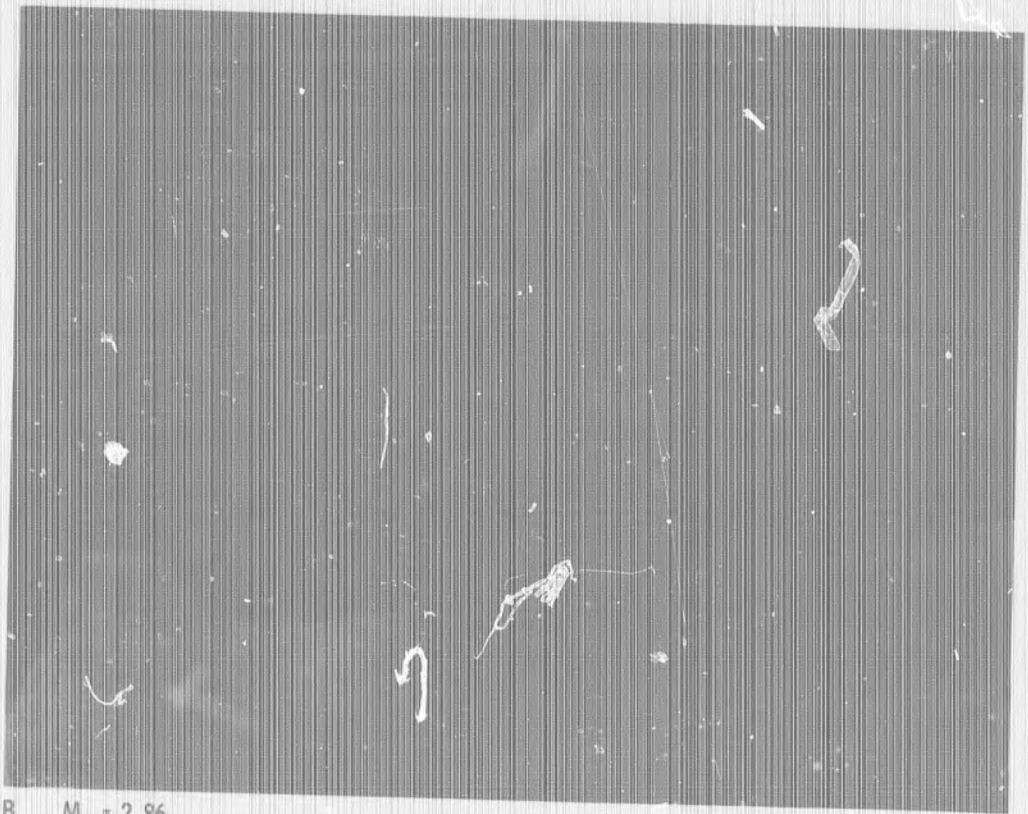

B. $M_s = 2.86$ (RUN 399)

FIG. A-11 TWO-SPARK SHADOW PHOTOGRAPHS OF THE SHOCK INTERACTION FIELD; 9° CONE AT FREE-STREAM MACH 7.0

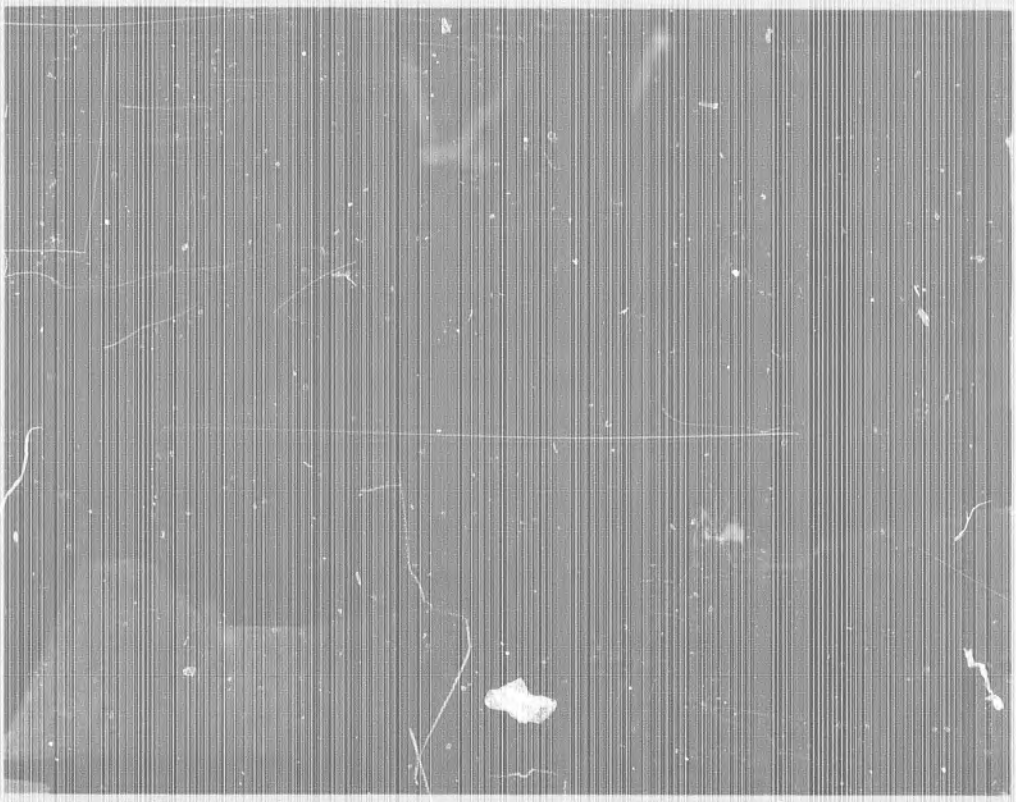

C. $M_s = 2.93$ (RUN 383)

D. $M_s = 3.03$ (RUN 381)

FIG. A-11 TWO-SPARK SHADOW PHOTOGRAPHS OF THE SHOCK INTERACTION FIELD; 9^0 CONE AT FREE-STREAM MACH 7.0 (CONTINUED)

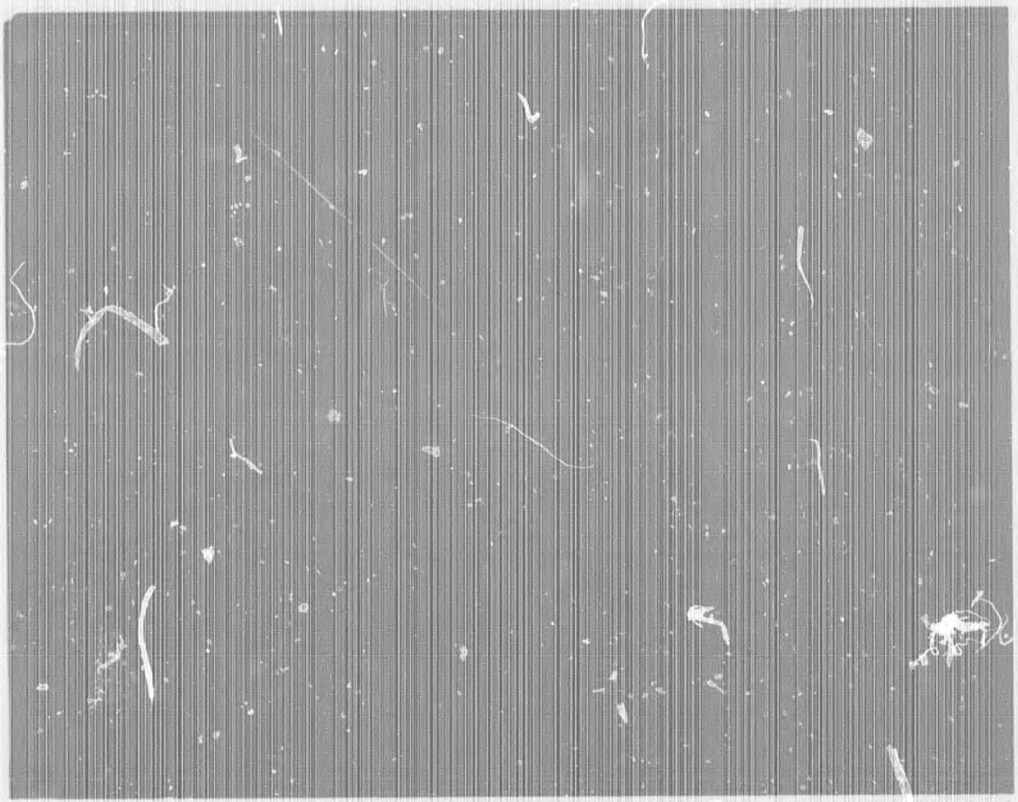

E. $M_s = 3.43$ (RUN 382)

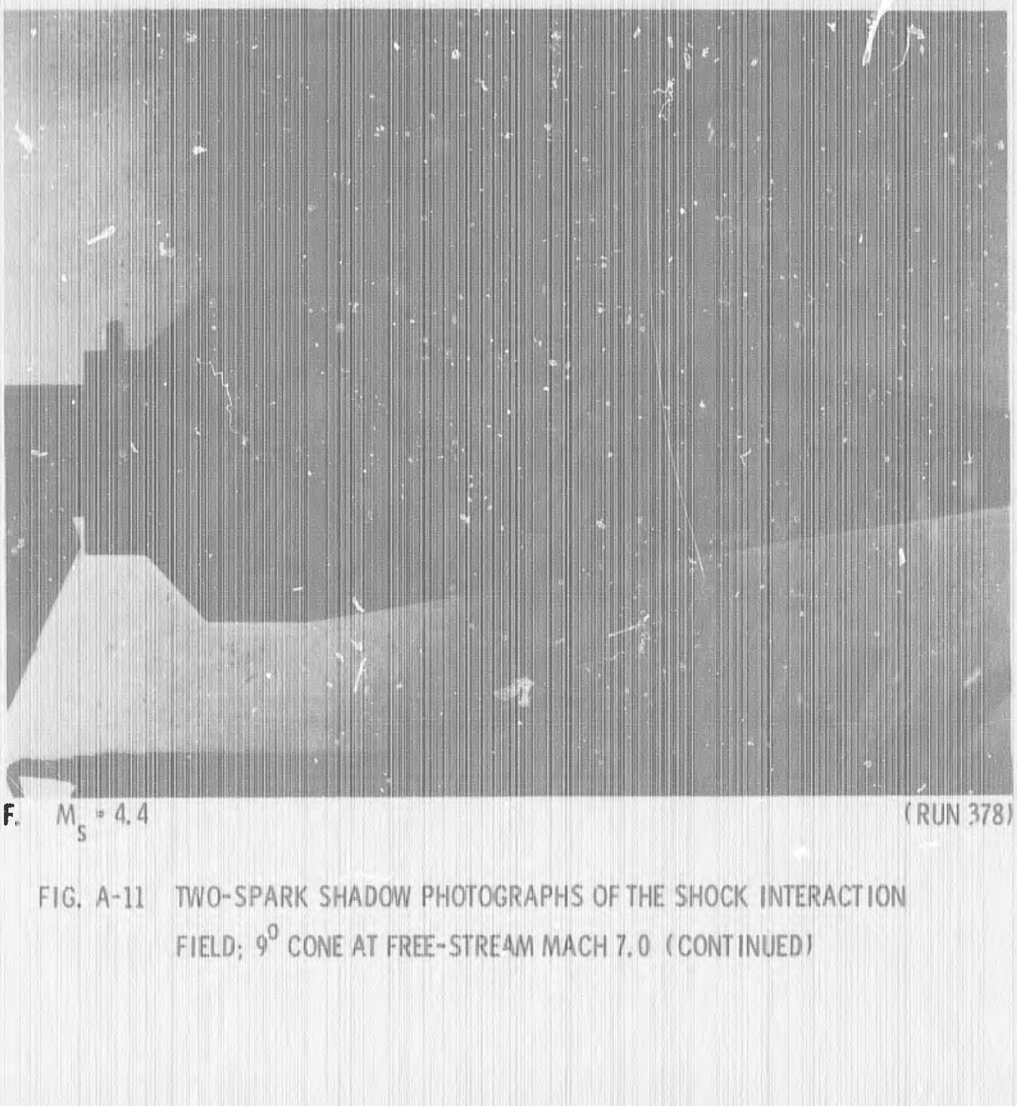

F. $M_s = 4.4$ (RUN 378)

FIG. A-11 TWO-SPARK SHADOW PHOTOGRAPHS OF THE SHOCK INTERACTION FIELD; 9° CONE AT FREE-STREAM MACH 7.0 (CONTINUED)

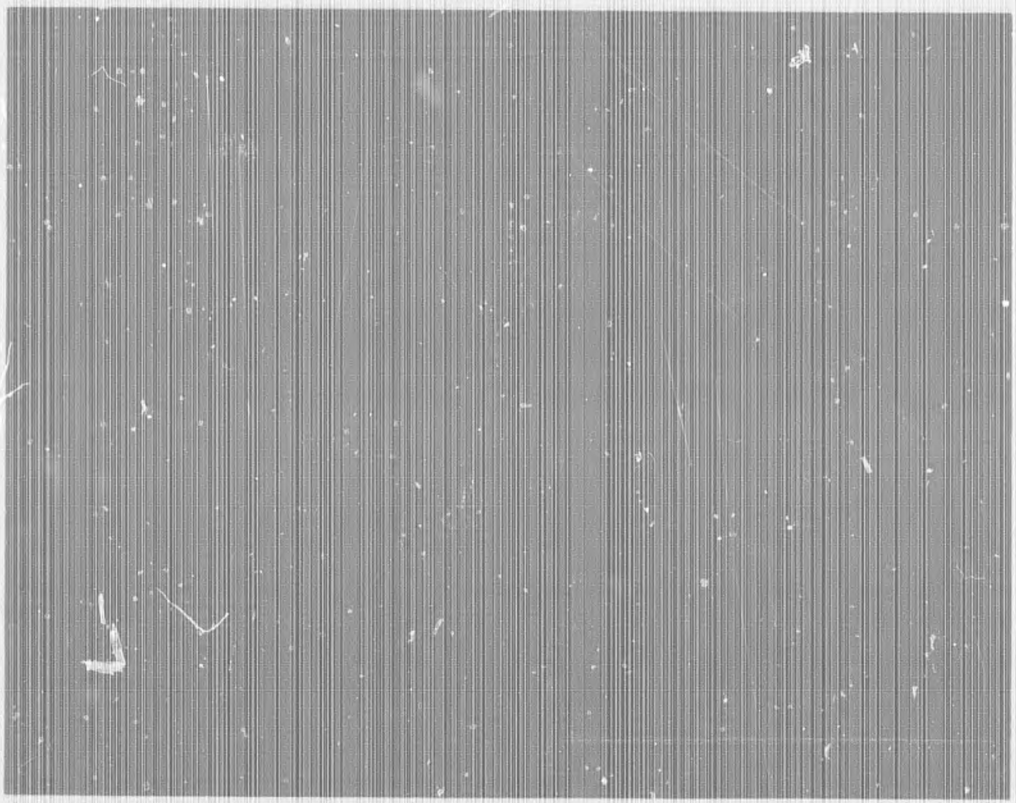

A. $M_s = 1.59$ (RUN 225)

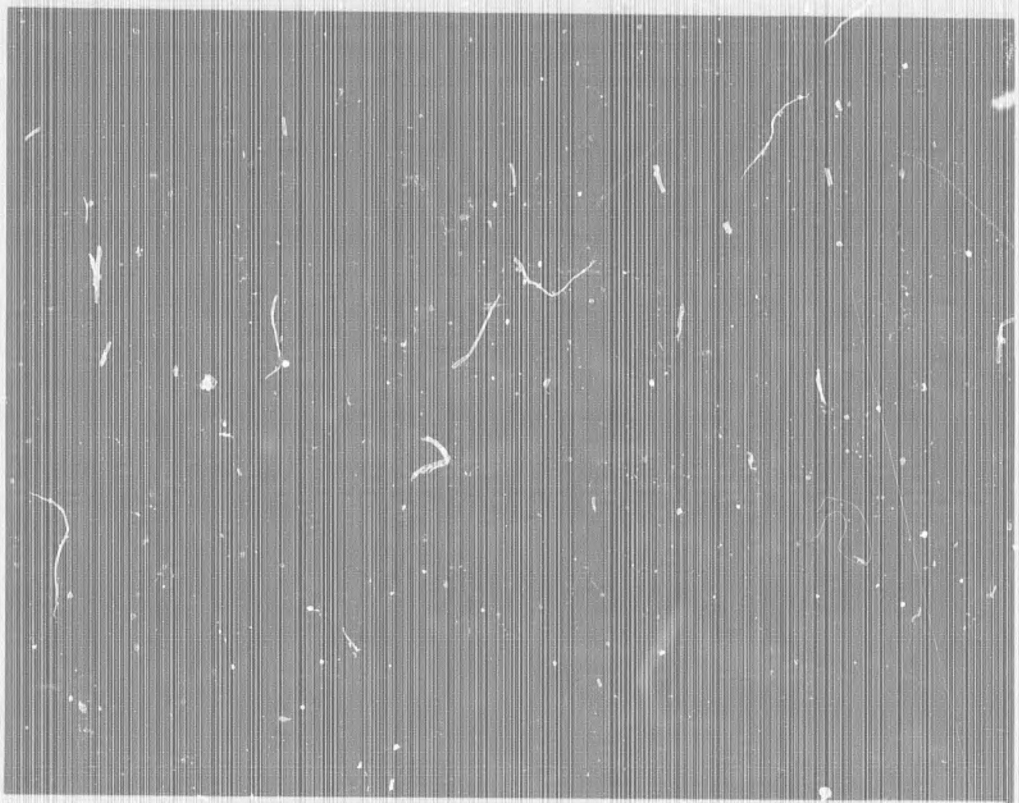

B. $M_s = 1.64$ (RUN 152)

FIG. A-12 SHADOW PHOTOGRAPHS OF THE SHOCK INTERACTION FIELD; 9^0 CONE AT FREE-STREAM MACH 3.1

C. $M_s = 1.67$ (RUN 153)

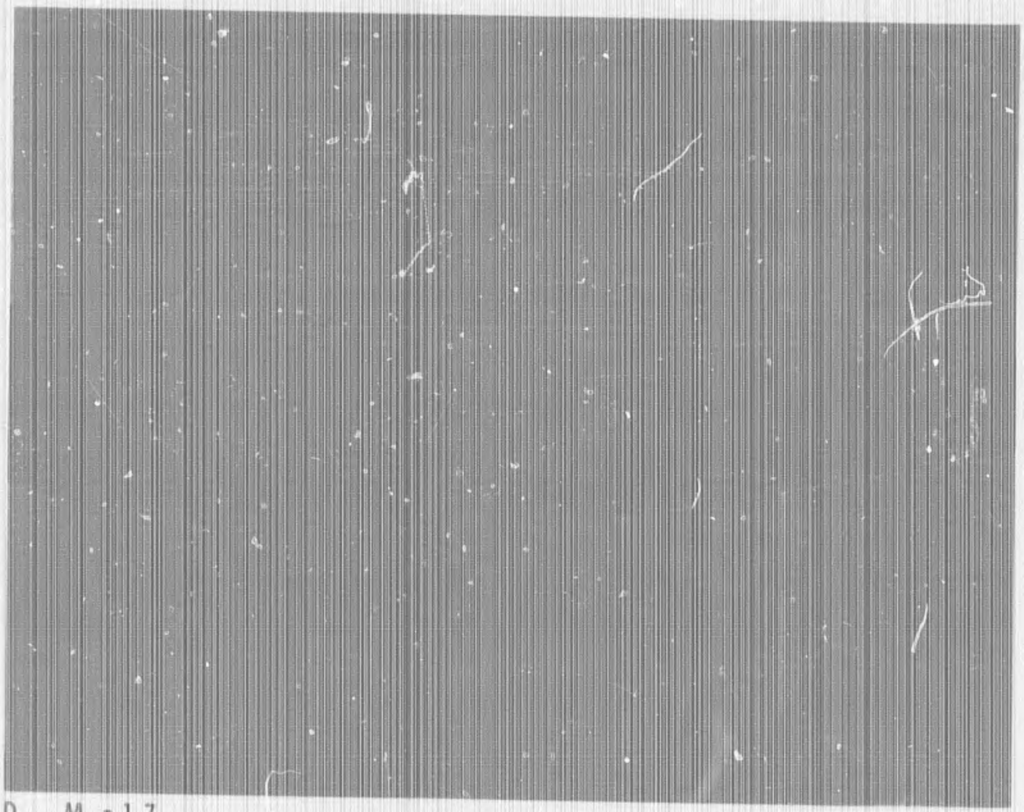

D. $M_s = 1.7$ (RUN 150)

FIG. A-12 SHADOW PHOTOGRAPHS OF THE SHOCK INTERACTION FIELD; 9° CONE AT FREE-STREAM MACH 3.1 (CONTINUED)

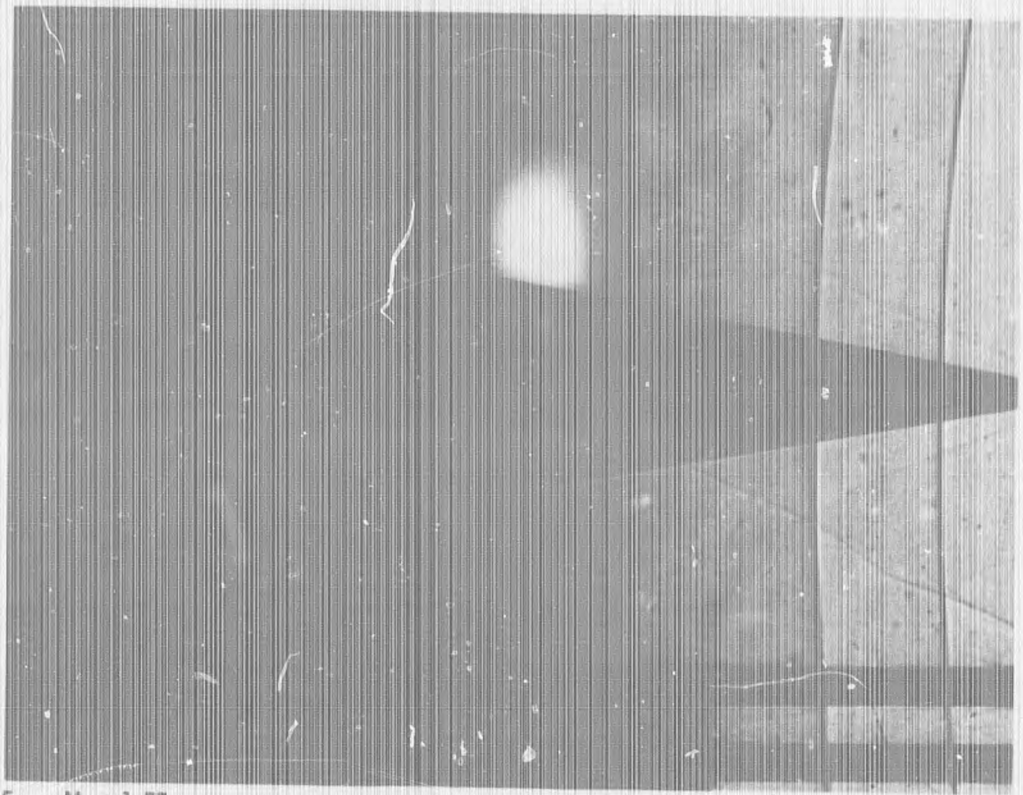

E. $M_s = 1.77$ (RUN 787)

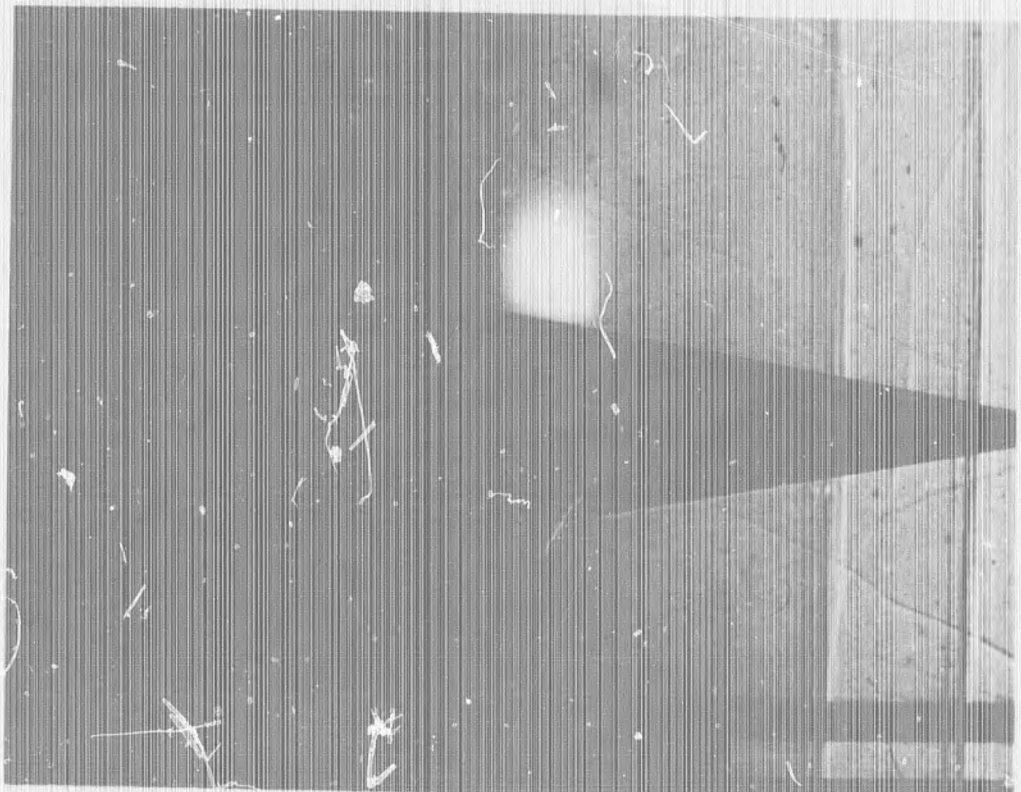

F. $M_s = 2.14$ (RUN 784)

FIG. A-12 SHADOW PHOTOGRAPHS OF THE SHOCK INTERACTION FIELD; 9^0 CONE AT FREE-STREAM MACH 3.1 (CONTINUED)

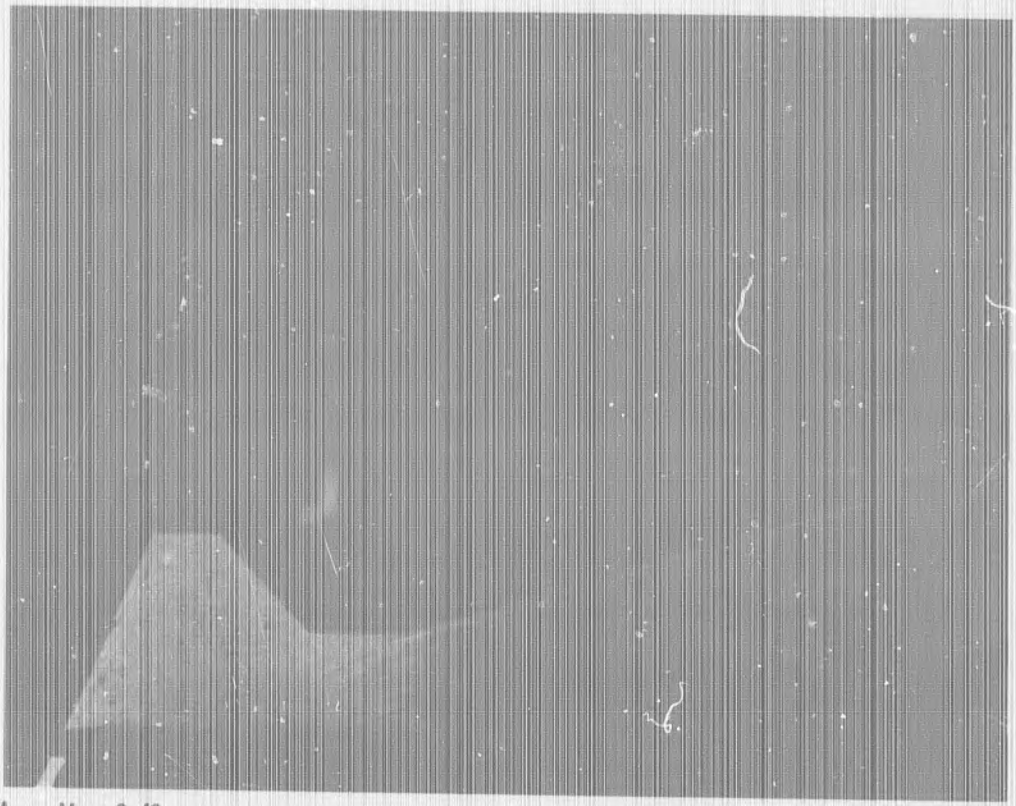

A. $M_s = 2.40$ (RUN 332)

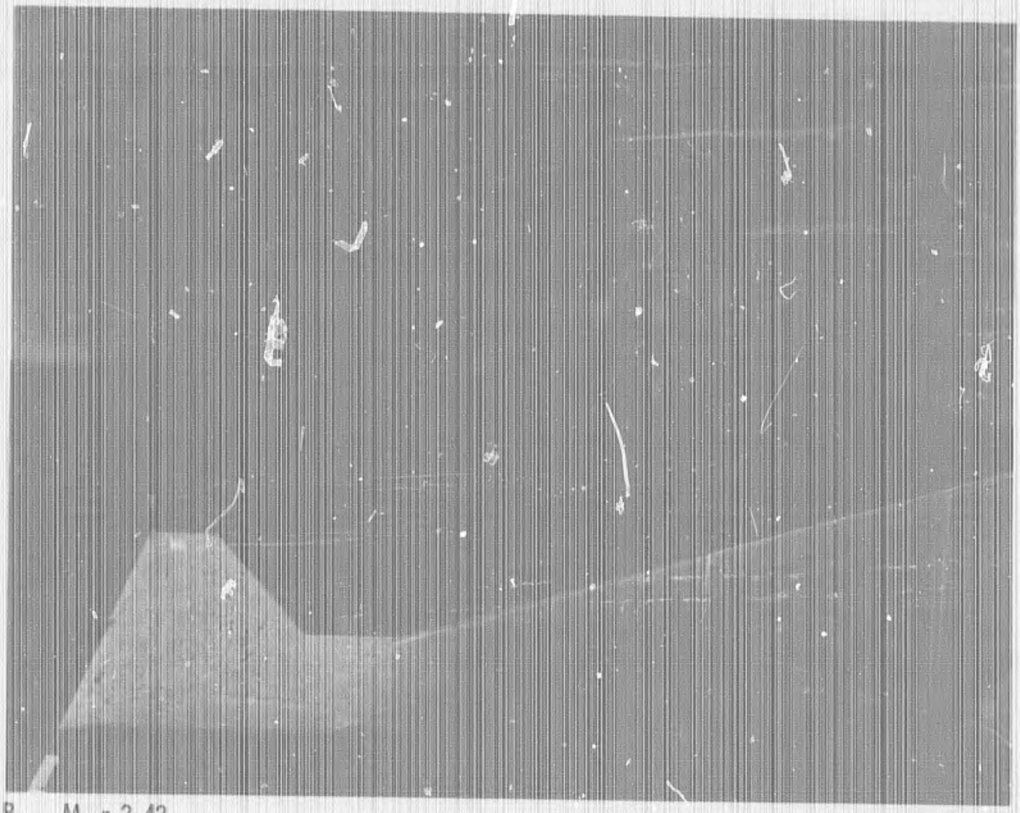

B. $M_s = 2.42$ (RUN 349)

FIG. A-13 TWO-SPARK SHADOW PHOTOGRAPHS OF THE SHOCK INTERACTION FIELD; 15° CONE AT FREE-STREAM MACH 5.1

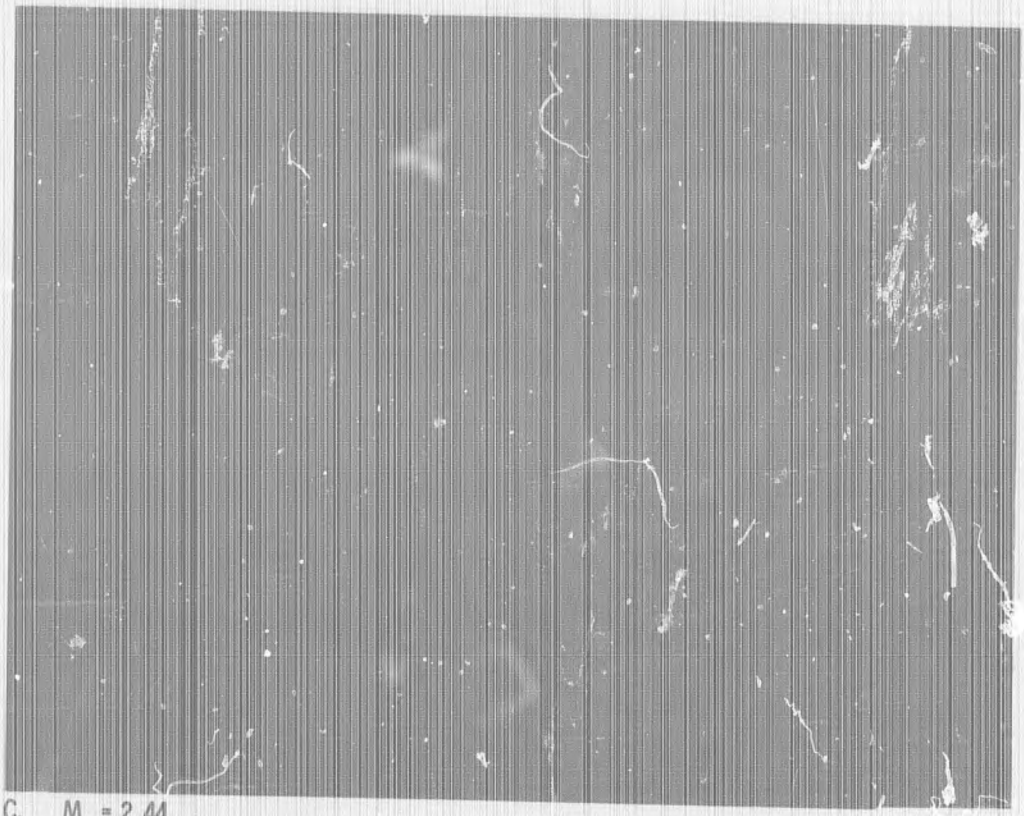

C. $M_s = 2.44$ (RUN 333)

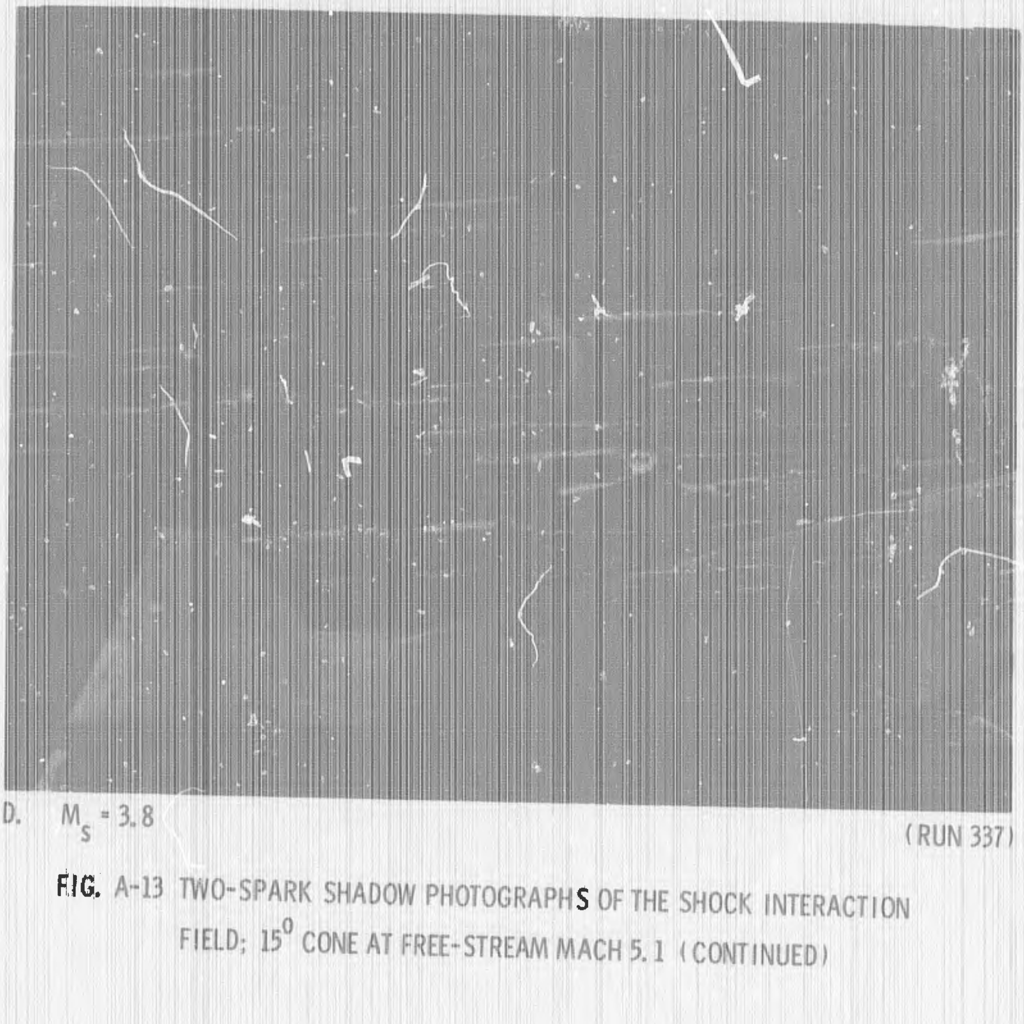

D. $M_s = 3.8$ (RUN 337)

FIG. A-13 TWO-SPARK SHADOW PHOTOGRAPHS OF THE SHOCK INTERACTION FIELD; 15^0 CONE AT FREE-STREAM MACH 5.1 (CONTINUED)

E. $M_s = 3.92$ (RUN 338)

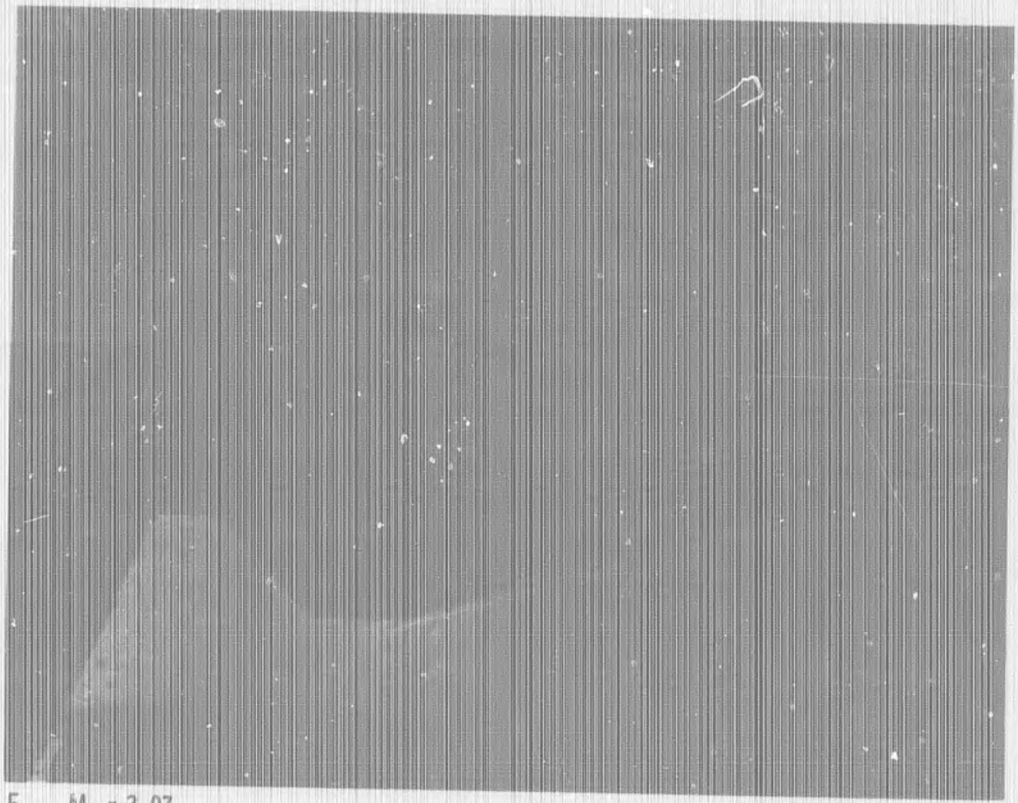

F. $M_s = 3.97$ (RUN 342)

FIG. A-13 TWO-SPARK SHADOW PHOTOGRAPHS OF THE SHOCK INTERACTION FIELD; 15^0 CONE AT FREE-STREAM MACH 5.1 (CONTINUED)

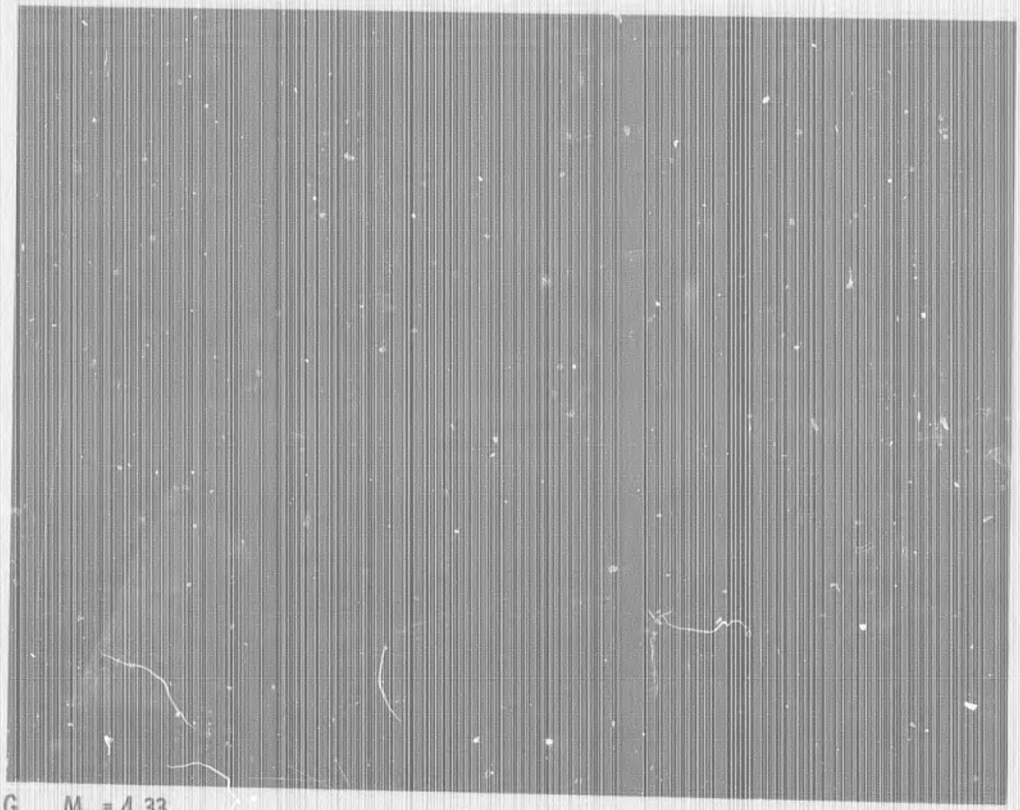

G. $M_s = 4.33$ (RUN 346)

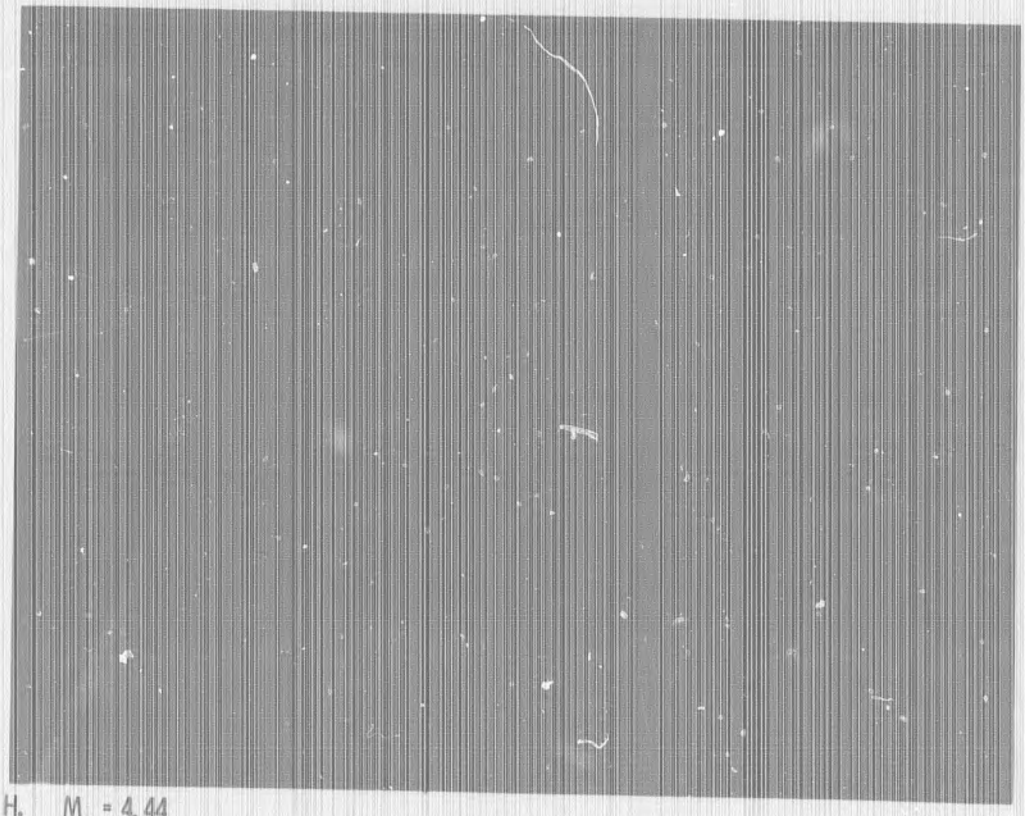

H. $M_s = 4.44$ (RUN 343)

FIG. A-13 TWO-SPARK SHADOW PHOTOGRAPHS OF THE SHOCK INTERACTION FIELD; 15^0 CONE AT FREE-STREAM MACH 5.1 (CONTINUED)

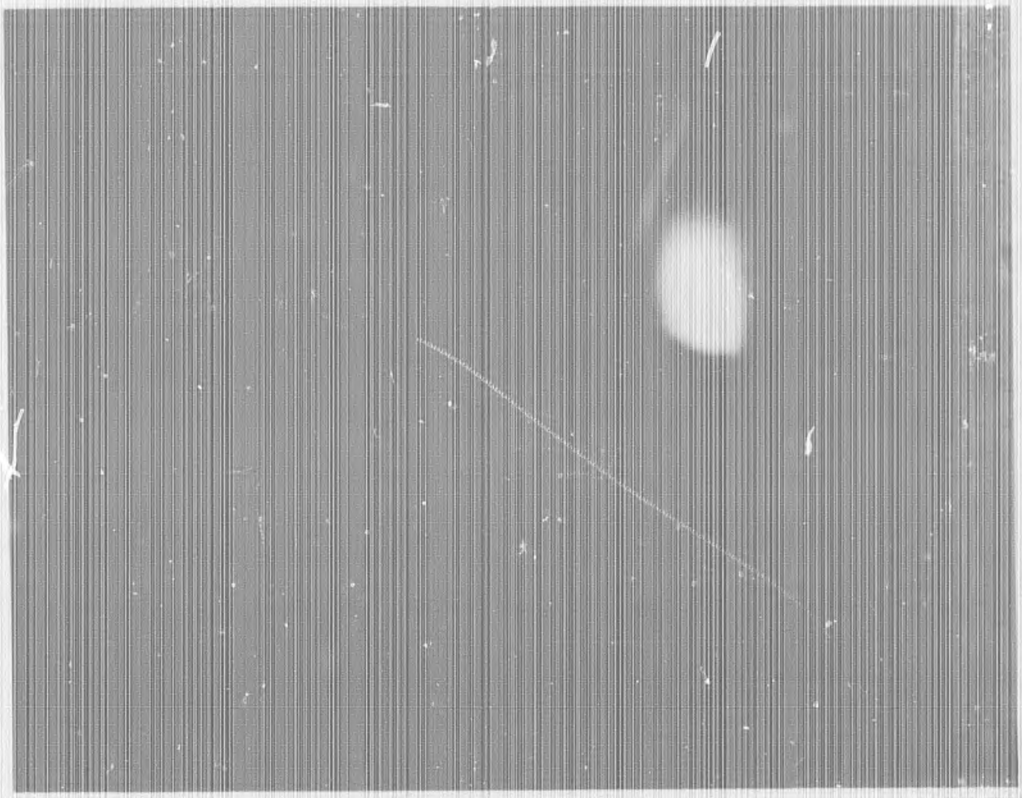

I. $M_s = 4.45$ (RUN 772)

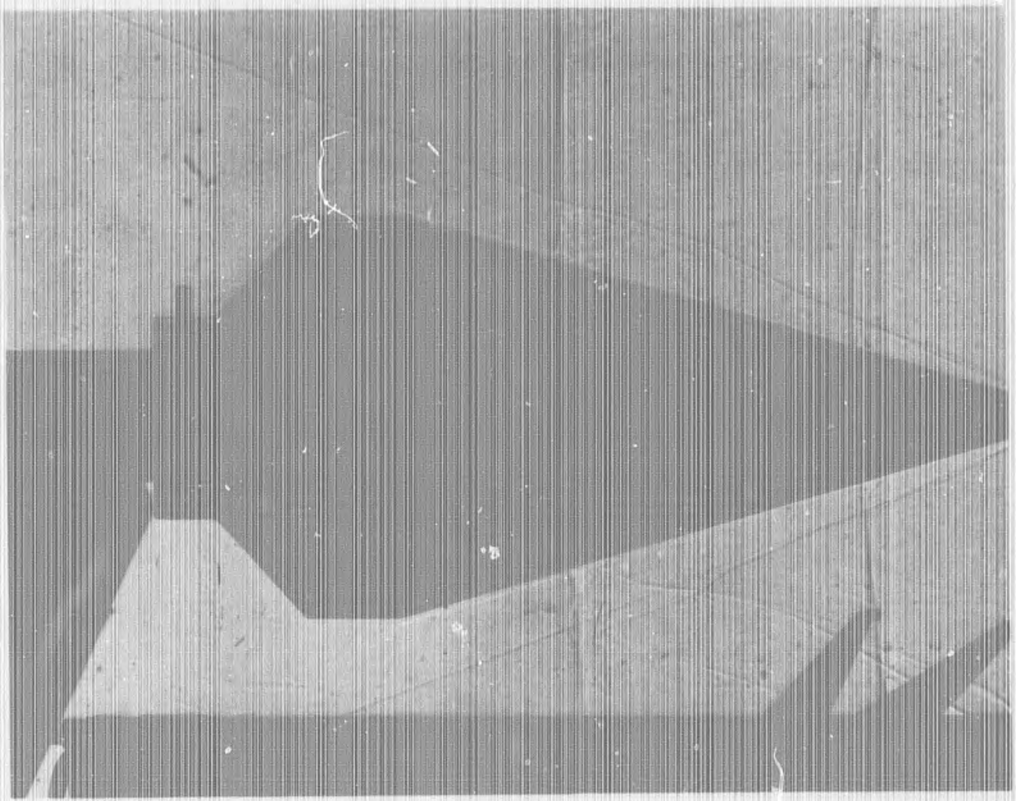

J. $M_s = 4.49$ (RUN 345)

FIG. A-13 TWO-SPARK SHADOW PHOTOGRAPHS OF THE SHOCK INTERACTION FIELD; 15° CONE AT FREE-STREAM MACH 5.1 (CONTINUED)

K. $M_s = 4.7$ (RUN 773)

L. $M_s = 4.84$ (RUN 672)

FIG. A-13 TWO-SPARK SHADOW PHOTOGRAPHS OF THE SHOCK INTERACTION FIELD; 15^0 CONE AT FREE-STREAM MACH 5.1 (CONTINUED)

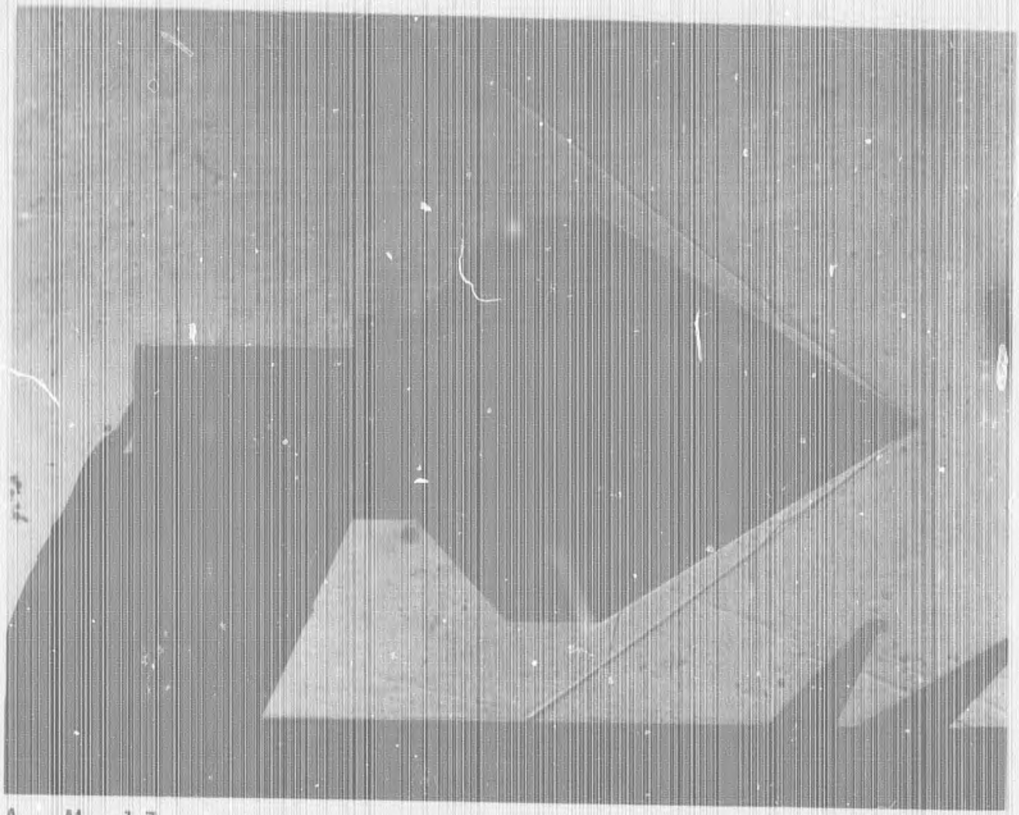

A. $M_s = 1.7$ (RUN 358)

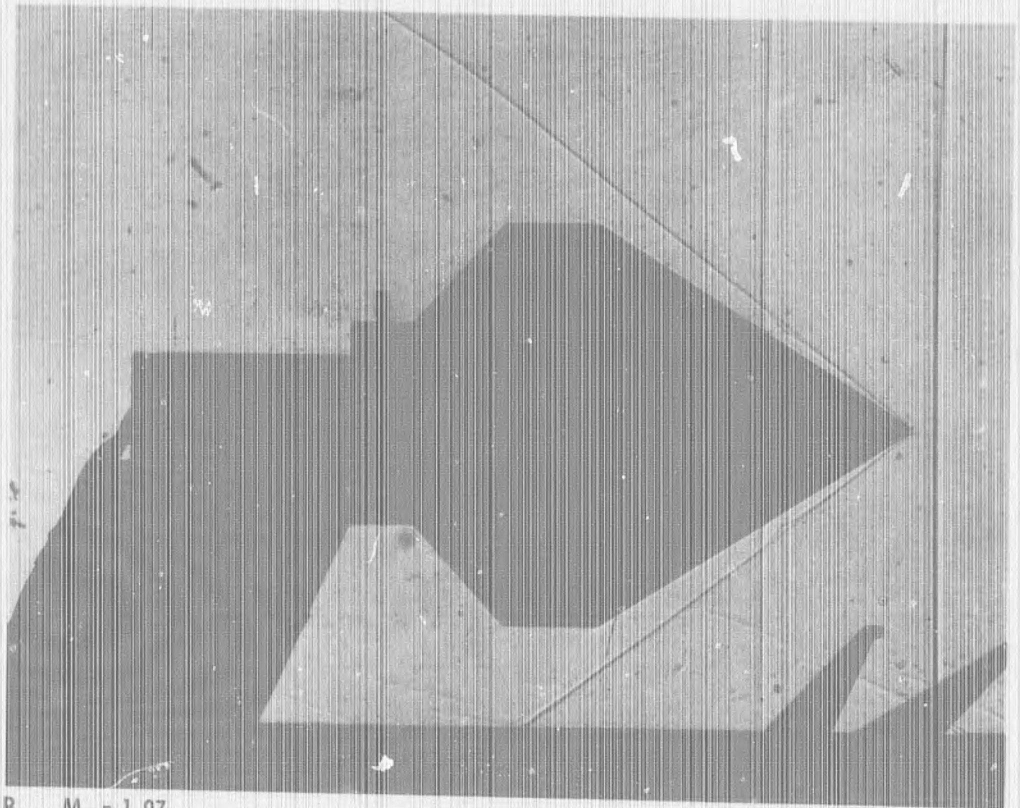

B. $M_s = 1.97$ (RUN 363)

FIG. A-14 TWO-SPARK SHADOW PHOTOGRAPHS OF THE SHOCK INTERACTION FIELD; 30° CONE AT FREE-STREAM MACH 5.1

C. $M_s = 2.2$ (RUN 359)

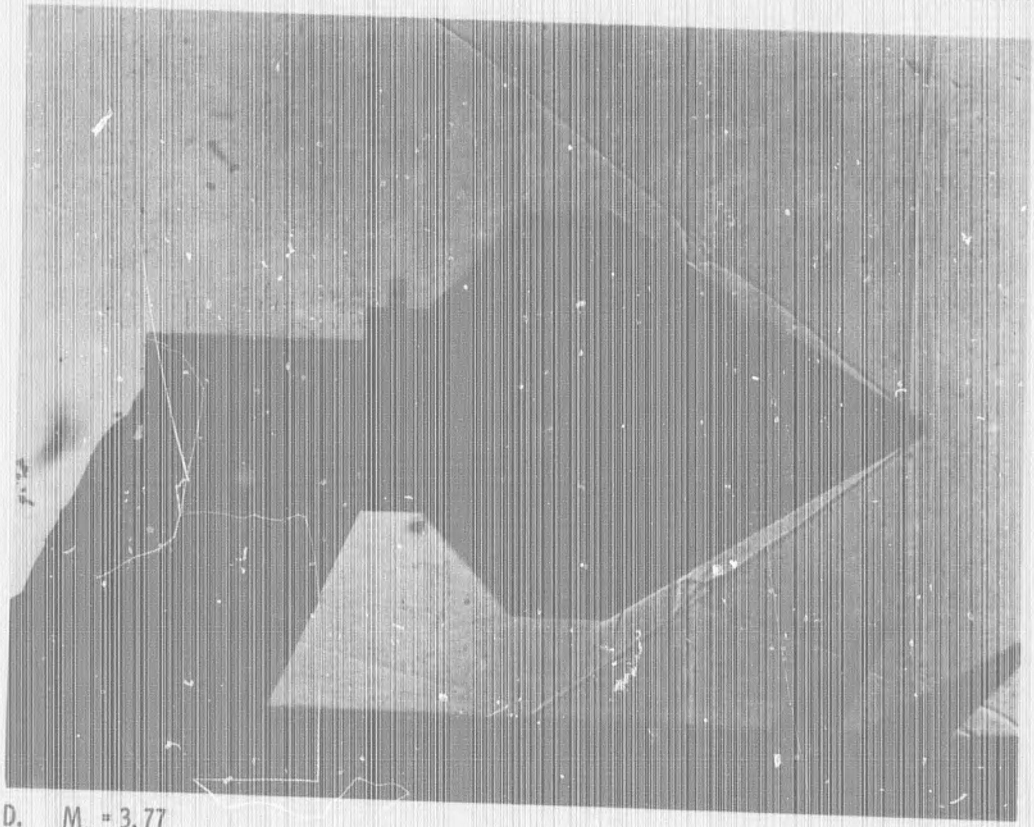

D. $M_s = 3.77$ (RUN 367)

FIG. A-14 TWO-SPARK SHADOW PHOTOGRAPHS OF THE SHOCK INTERACTION FIELD; 30° CONE AT FREE-STREAM MACH 5.1 (CONTINUED)

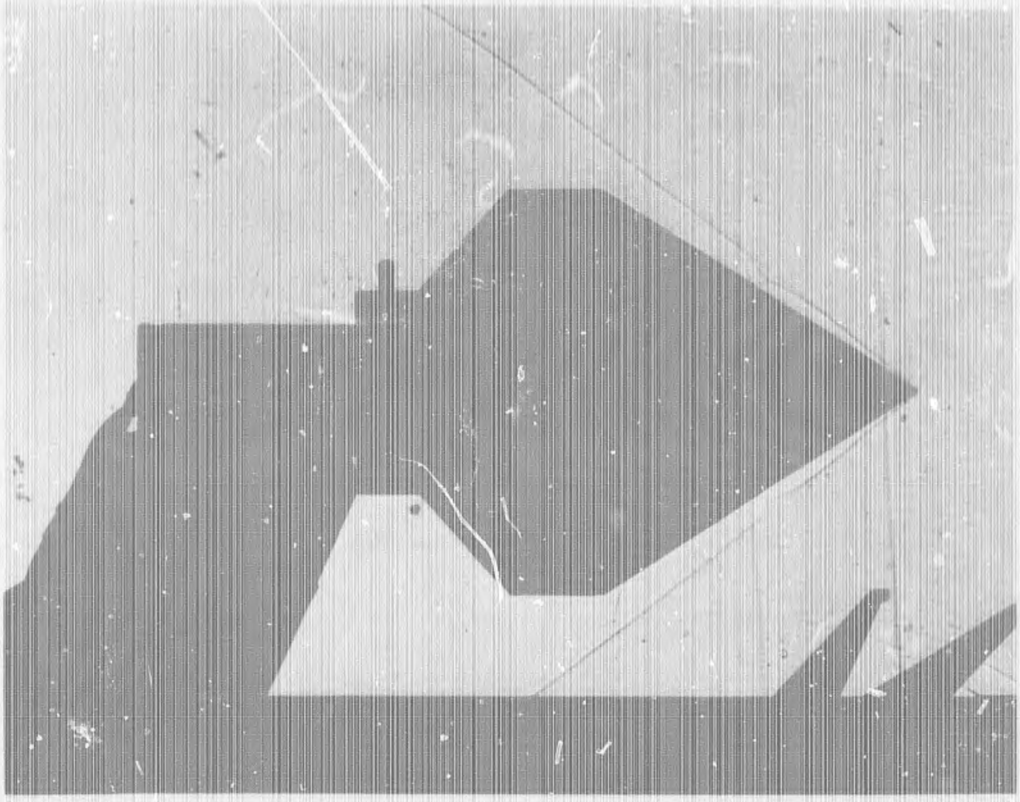

E. $M_s = 3.87$ (RUN 372)

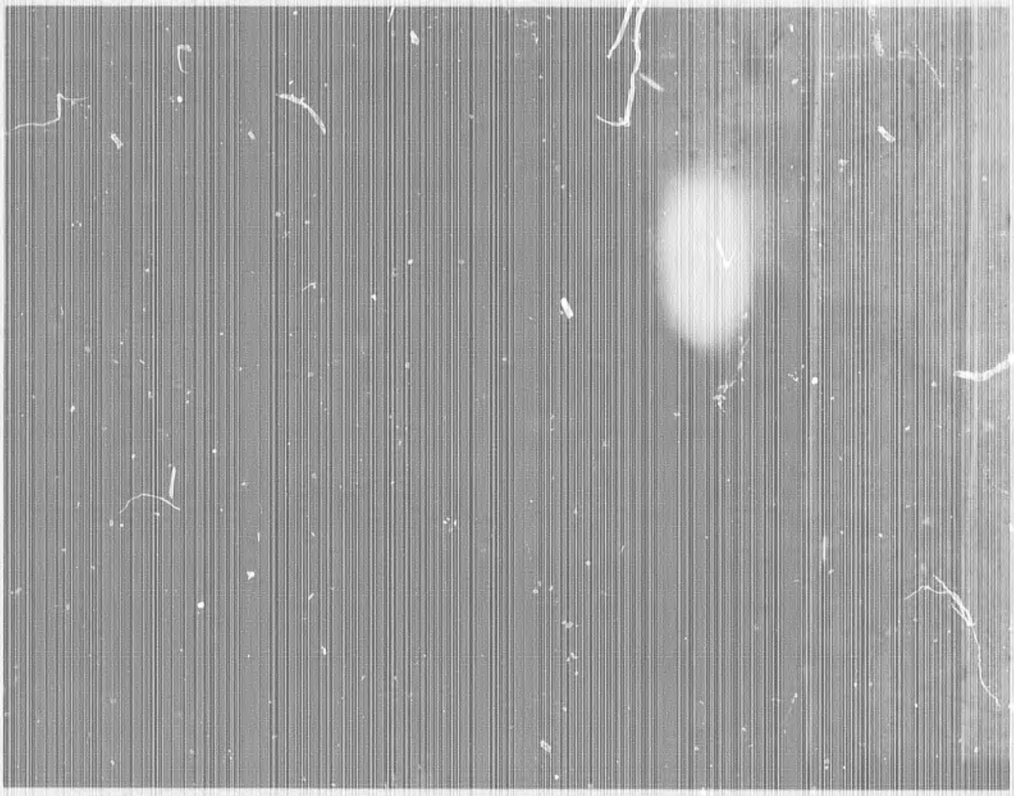

F. $M_s = 3.96$ (RUN 776)

FIG. A-14 TWO-SPARK SHADOW PHOTOGRAPHS OF THE SHOCK INTERACTION FIELD; 30° CONE AT FREE-STREAM MACH 5.1 (CONTINUED)

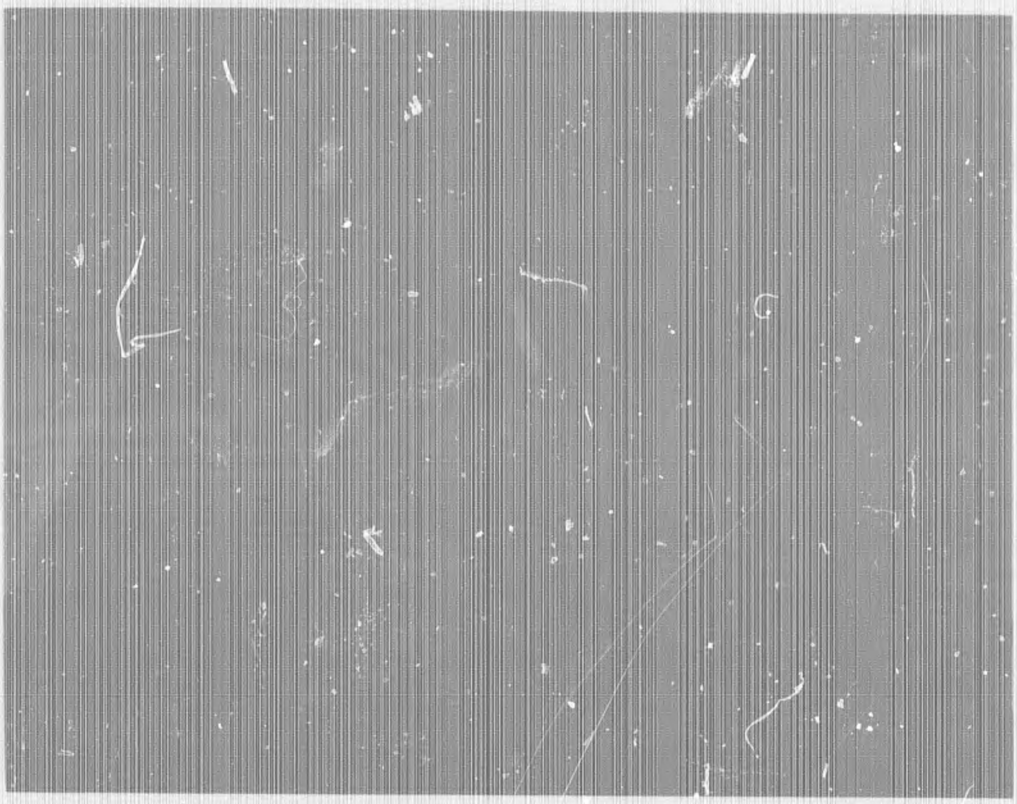

G. $M_s = 3.97$ (RUN 366)

H. $M_s = 4.02$ (RUN 370)

FIG. A-14 TWO-SPARK SHADOW PHOTOGRAPHS OF THE SHOCK INTERACTION FIELD; 30° CONE AT FREE-STREAM MACH 5.1 (CONTINUED)

I. $M_s = 4.89$ (RUN 661)

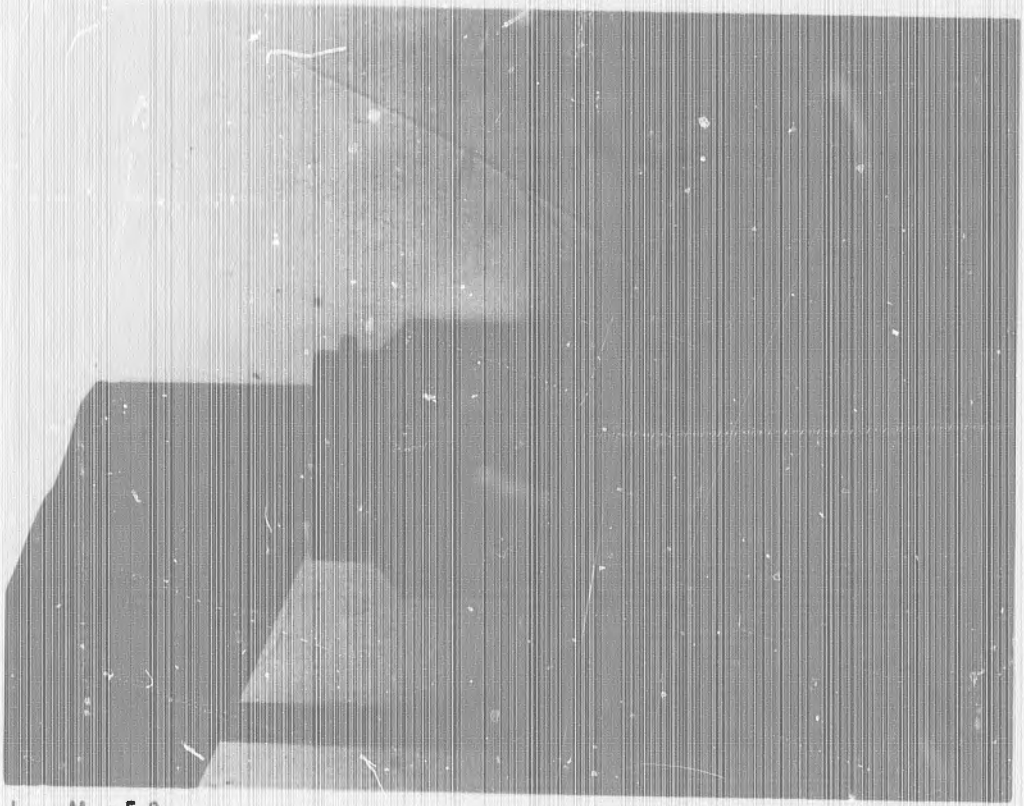

J. $M_s = 5.0$ (RUN 663)

FIG. A-14 TWO-SPARK SHADOW PHOTOGRAPHS OF THE SHOCK INTERACTION FIELD; 30° CONE AT FREE-STREAM MACH 5.1 (CONTINUED)

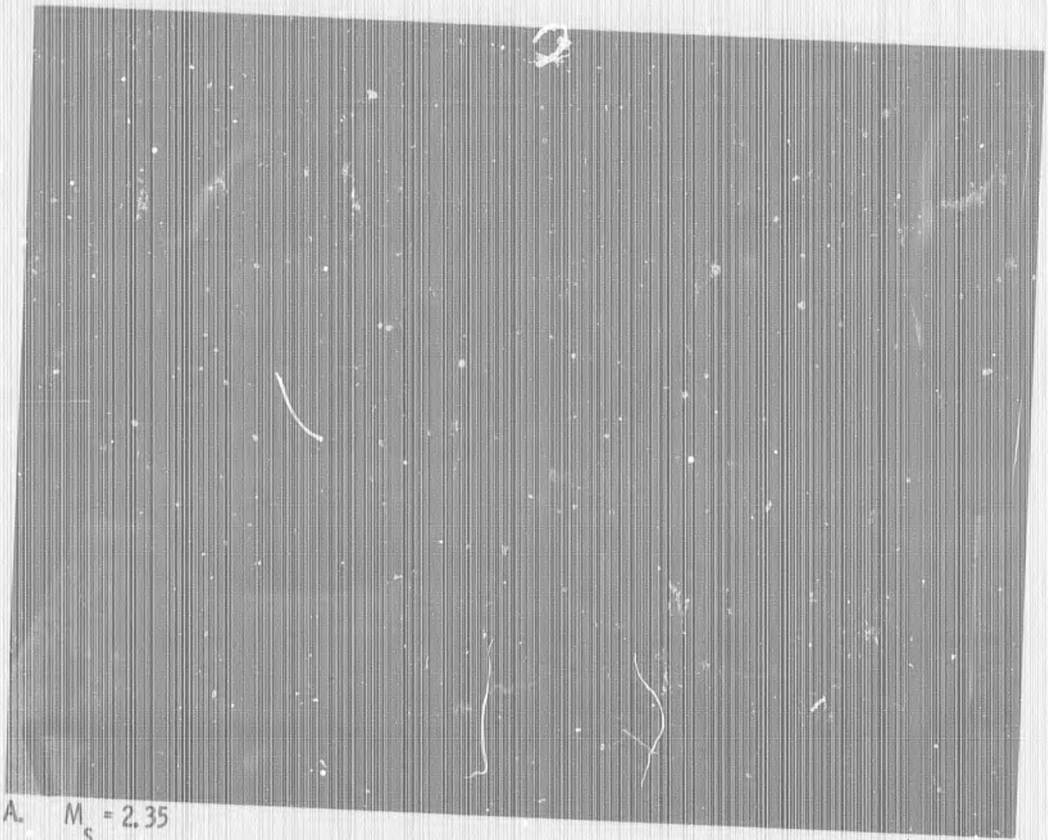

A. $M_s = 2.35$

(RUN 417)

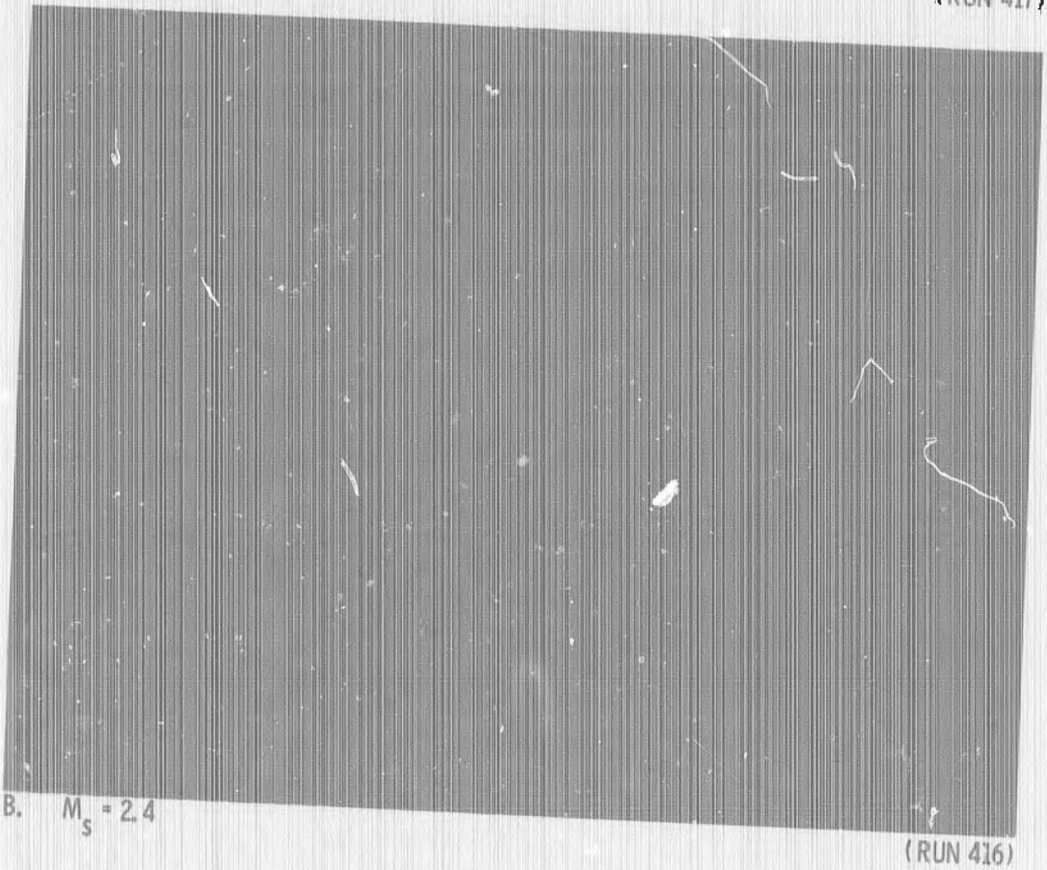

B. $M_s = 2.4$

(RUN 416)

FIG. A-15 TWO-SPARK SHADOW PHOTOGRAPHS OF THE SHOCK INTERACTION FIELD; SPHERICALLY BLUNTED 9° CONE AT FREE-STREAM MACH 5.1

C. $M_s = 4.25$ (RUN 739)

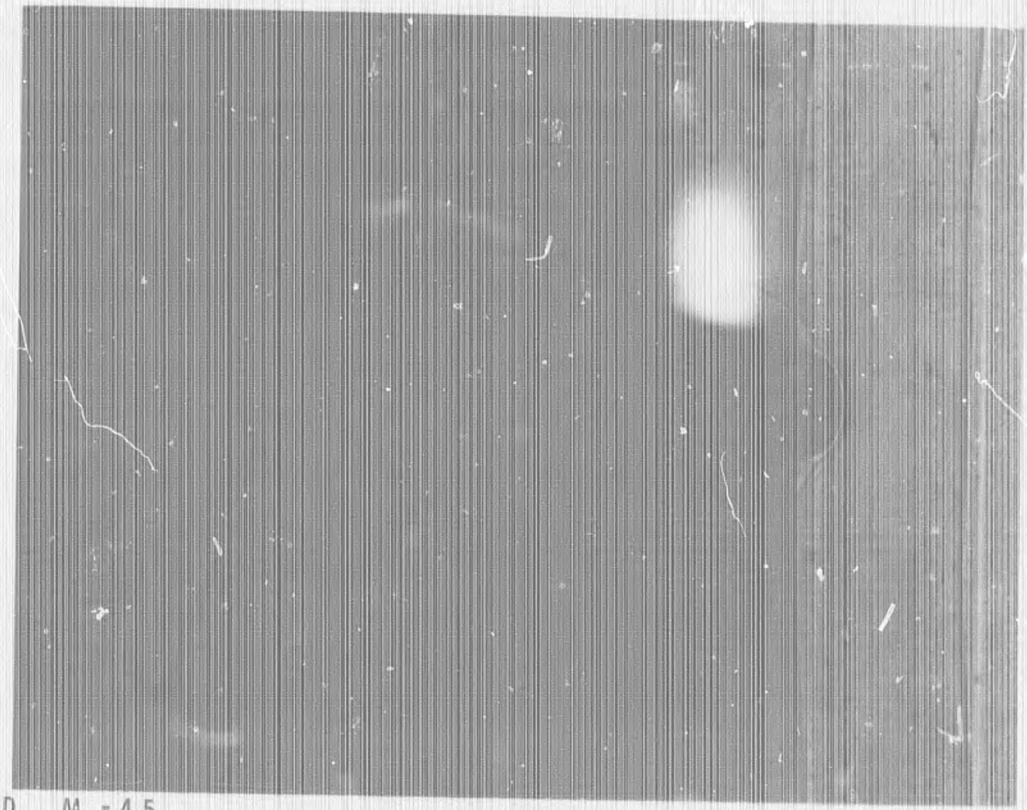

D. $M_s = 4.5$ (RUN 766)

FIG. A-15 TWO-SPARK SHADOW PHOTOGRAPHS OF THE SHOCK INTERACTION FIELD; SPHERICALLY BLUNTED 9° CONE AT FREE-STREAM MACH 5.1 (CONTINUED)

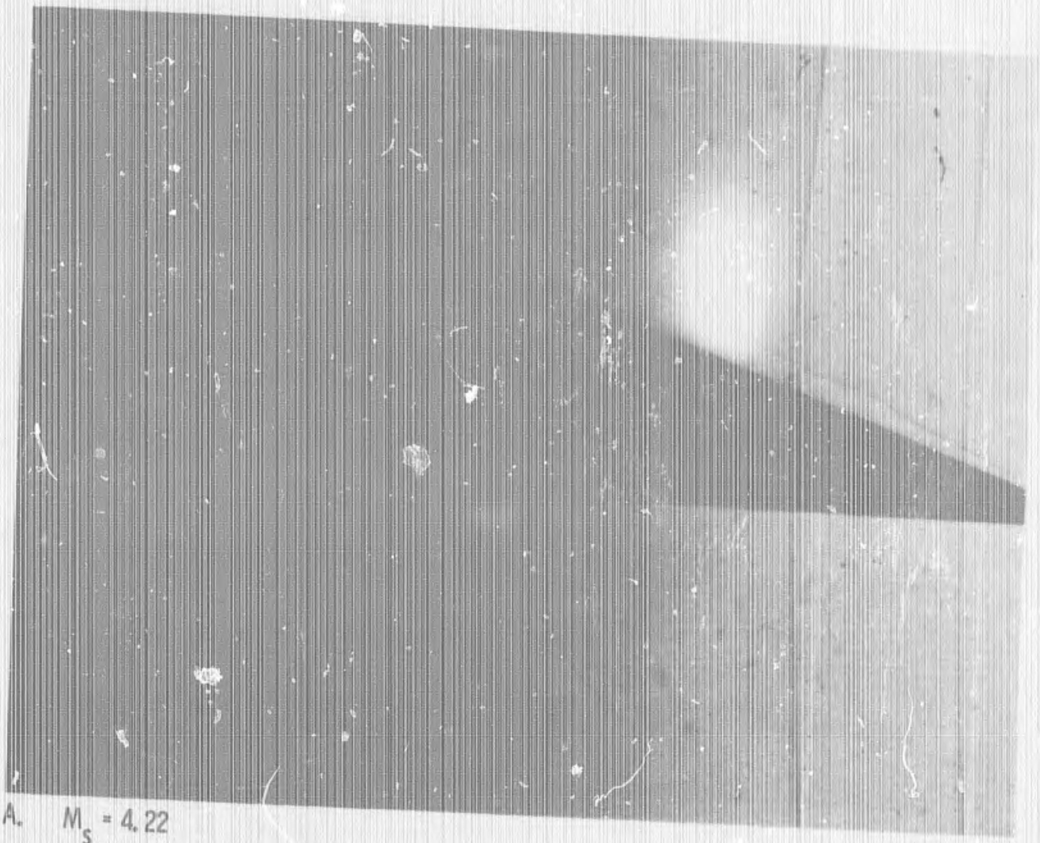

A. $M_s = 4.22$

(RUN 744)

B. $M_s = 4.27$

(RUN 741)

FIG. A-16 TWO-SPARK SHADOW PHOTOGRAPHS OF THE SHOCK INTERACTION FIELD; 9^o CONE AT 10^o INCIDENCE ANGLE AT FREE-STREAM MACH 5.1

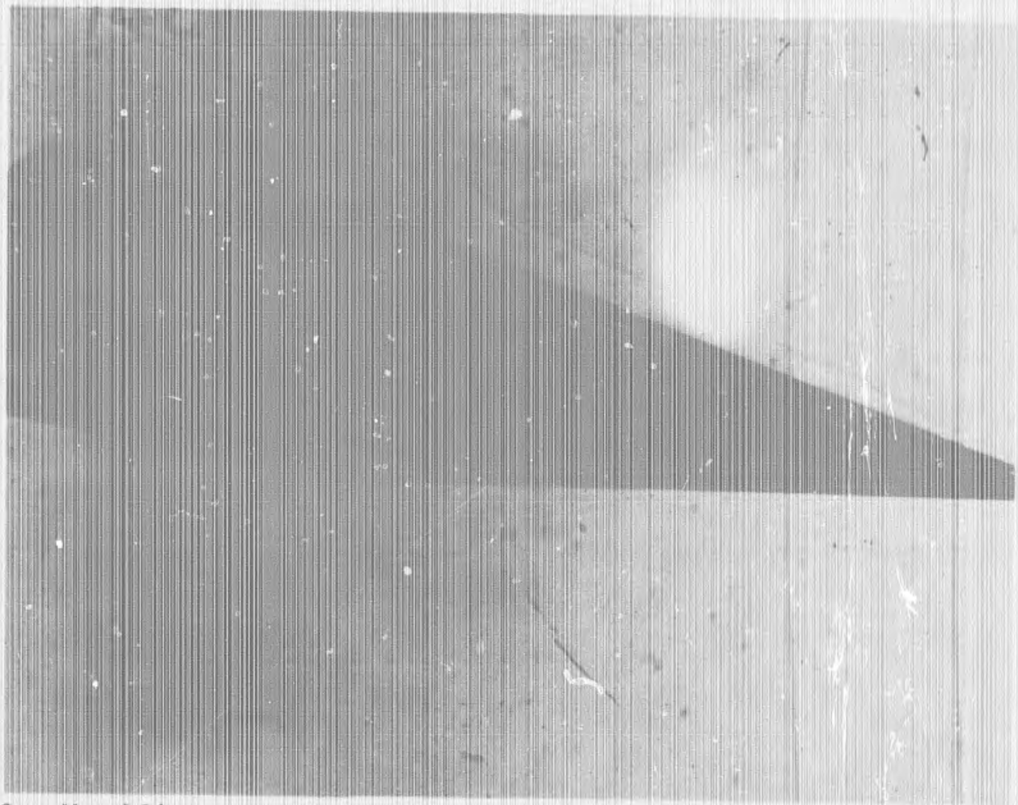

C. $M_s = 4.34$ (RUN 742)

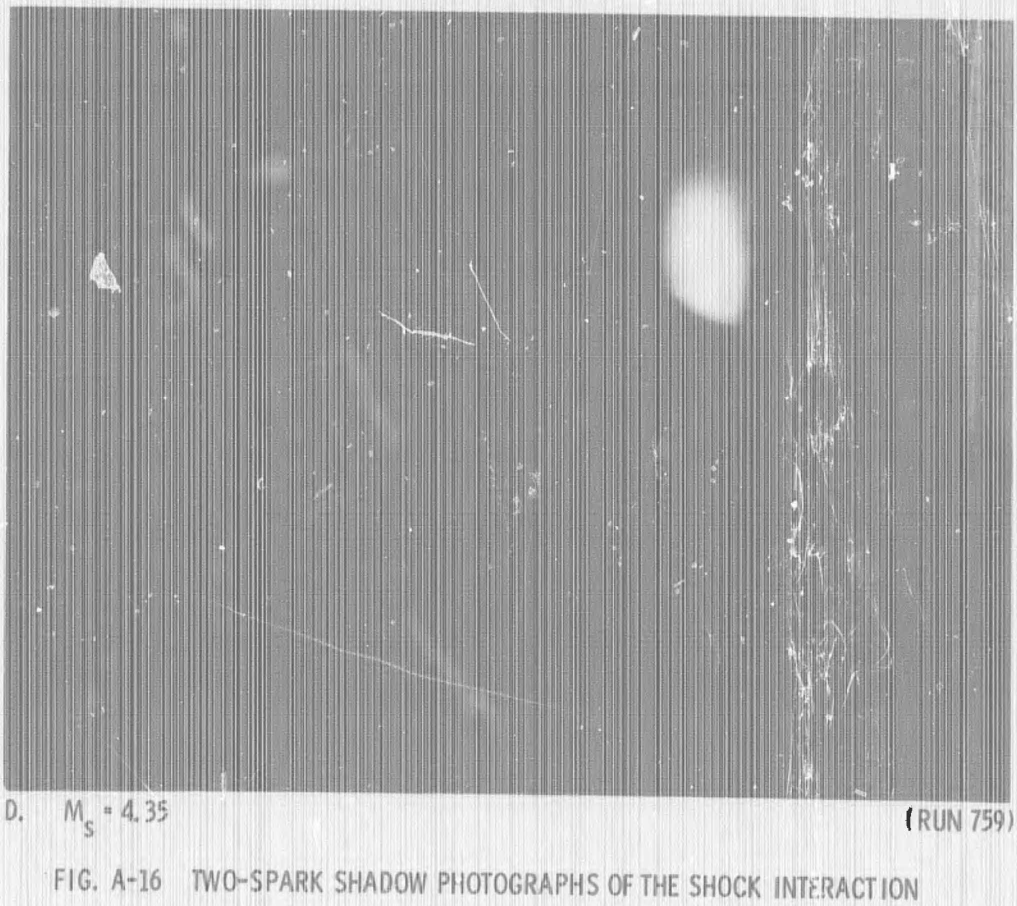

D. $M_s = 4.35$ (RUN 759)

FIG. A-16 TWO-SPARK SHADOW PHOTOGRAPHS OF THE SHOCK INTERACTION FIELD; 9^0 CONE AT 10^0 INCIDENCE ANGLE AT FREE-STREAM MACH 5.1 (CONTINUED)

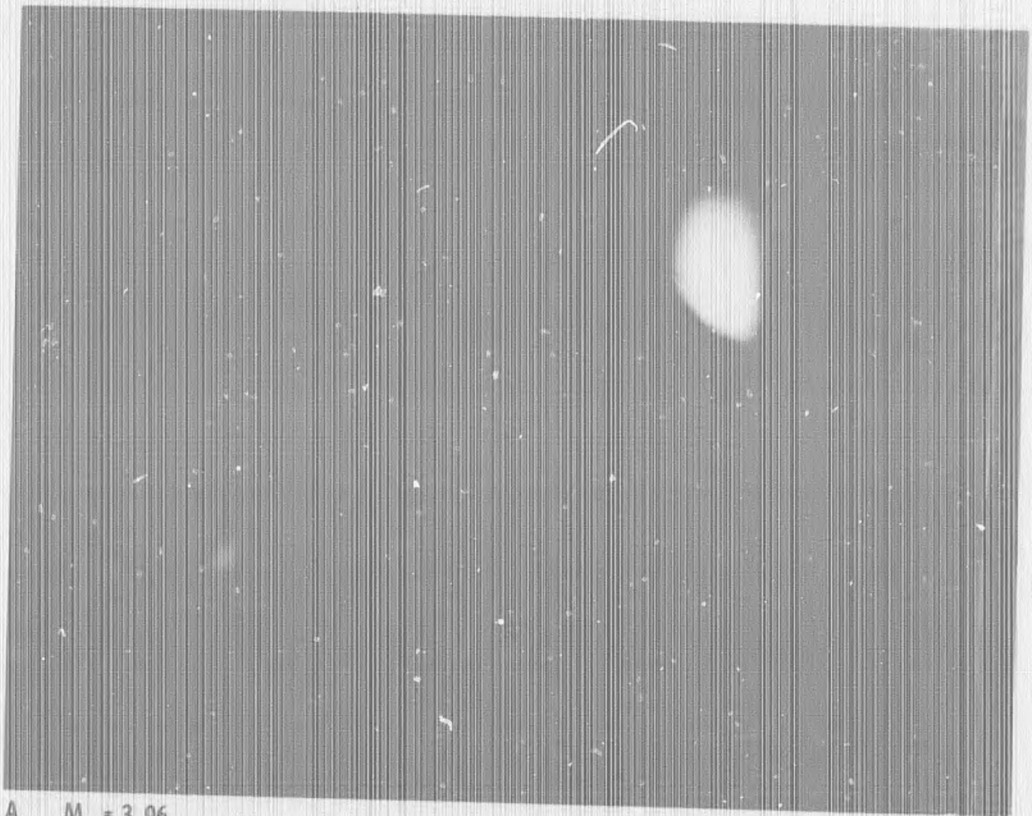

A. $M_s = 3.96$ (RUN 754)

B. $M_s = 4.16$ (RUN 749)

FIG. A-17 TWO-SPARK SHADOW PHOTOGRAPHS OF THE SHOCK INTERACTION FIELD: 9^0 CONE AT 20^0 INCIDENCE ANGLE AT FREE-STREAM MACH 5.1

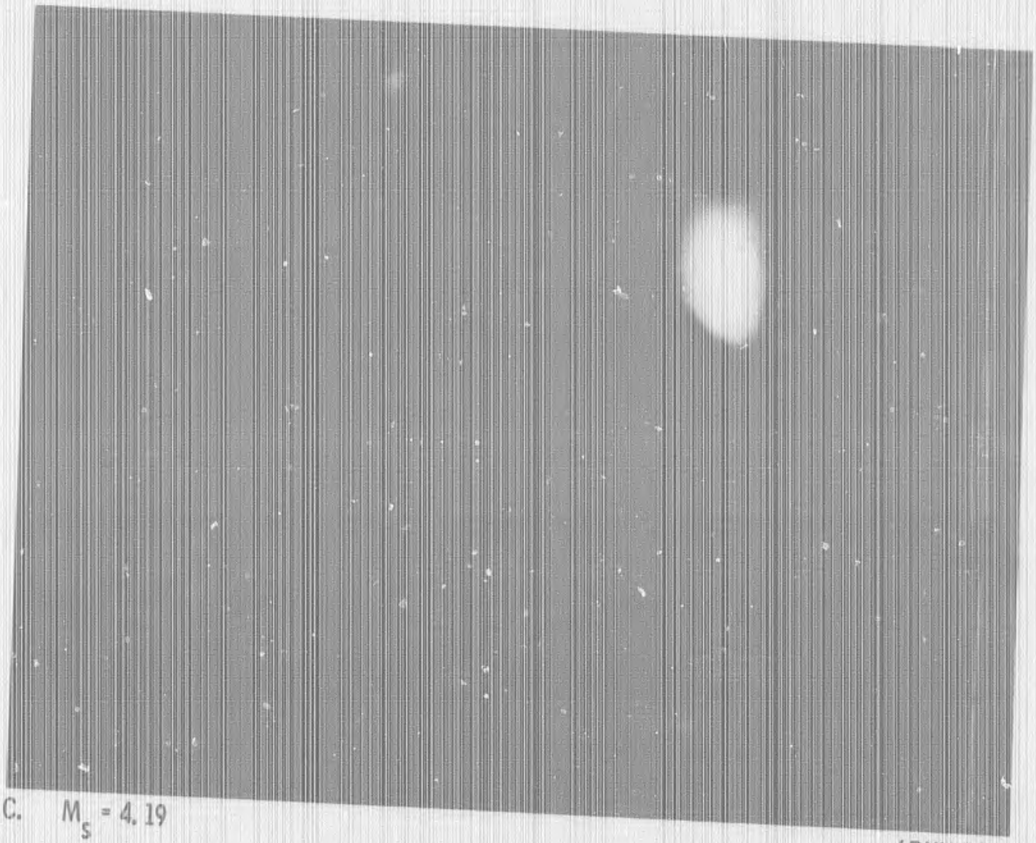

C. $M_s = 4.19$

(RUN 748)

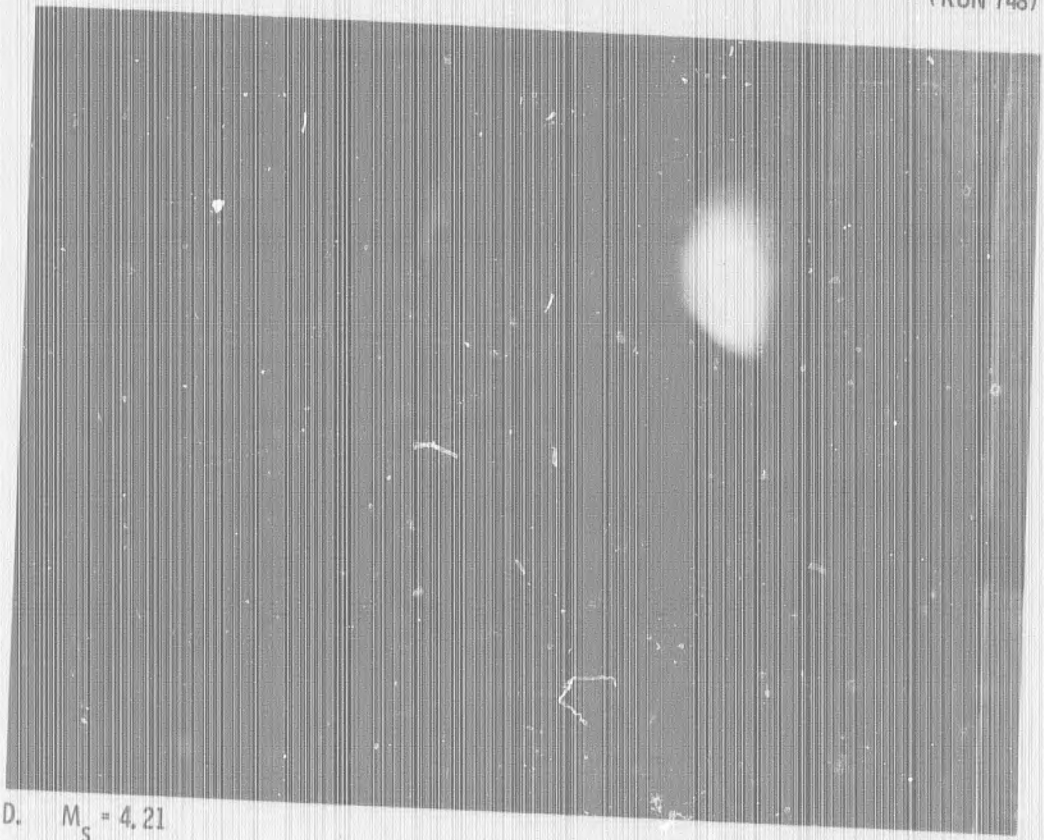

D. $M_s = 4.21$

(RUN 761)

FIG. A-17 TWO-SPARK SHADOW PHOTOGRAPHS OF THE SHOCK INTERACTION FIELD; 9^0 CONE AT 20^0 INCIDENCE ANGLE AT FREE-STREAM MACH 5.1 (CONTINUED)

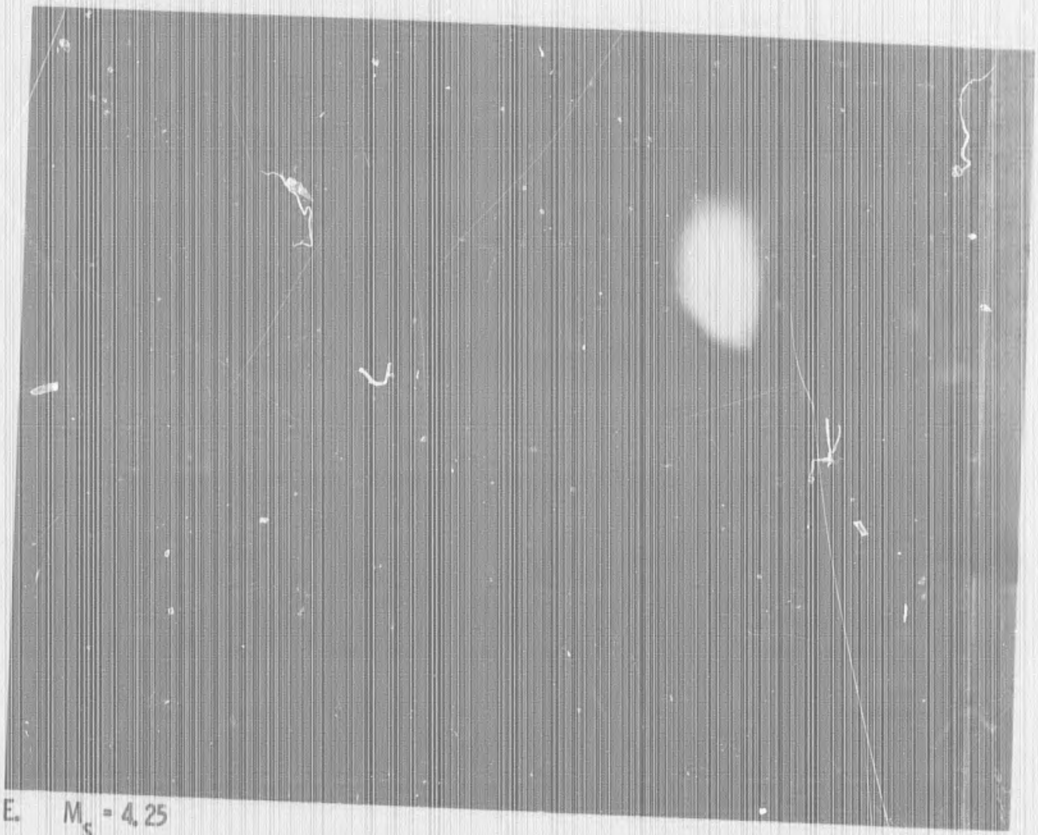

E. $M_s = 4.25$

(RUN 756)

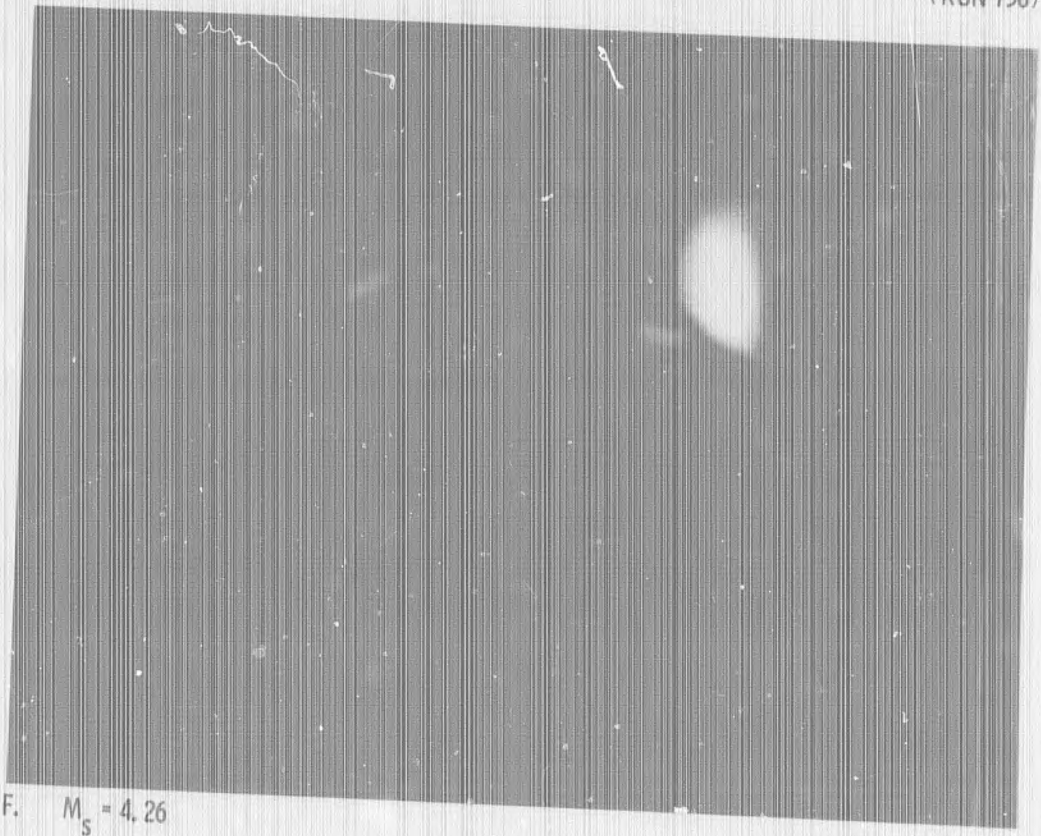

F. $M_s = 4.26$

(RUN 763)

FIG. A-17 TWO-SPARK SHADOW PHOTOGRAPHS OF THE SHOCK INTERACTION FIELD; 9° CONE AT 20° INCIDENCE ANGLE AT FREE-STREAM MACH 5.1 (CONTINUED)

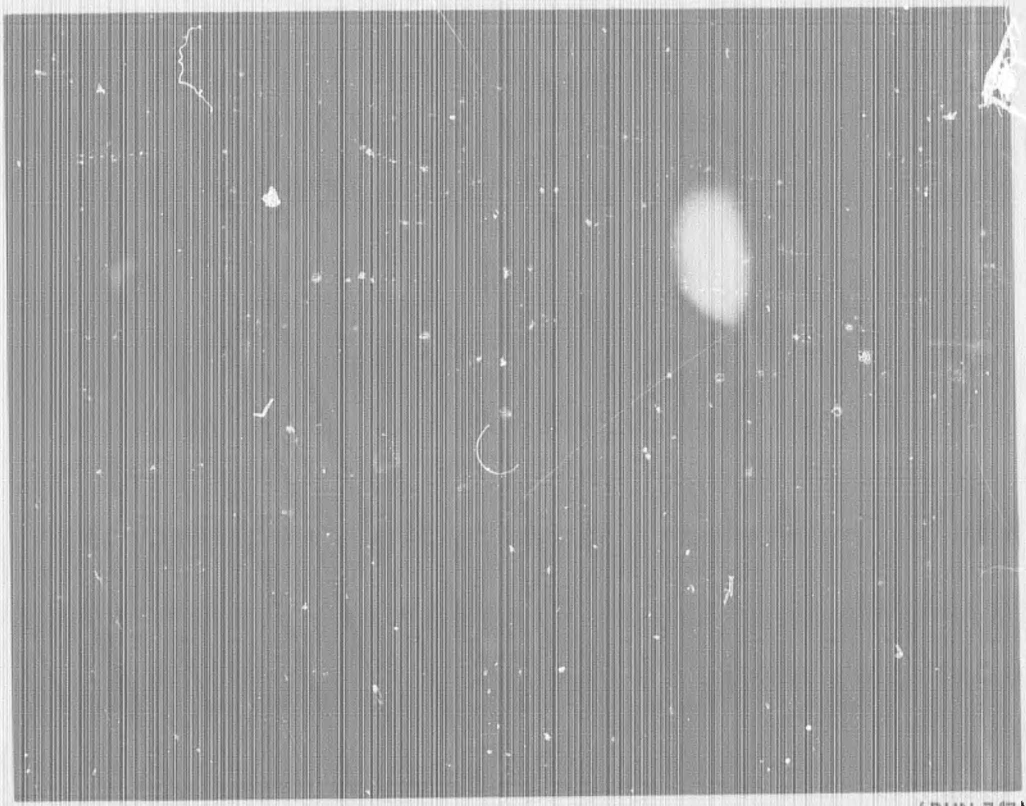

G. $M_s = 4.37$ (RUN 747)

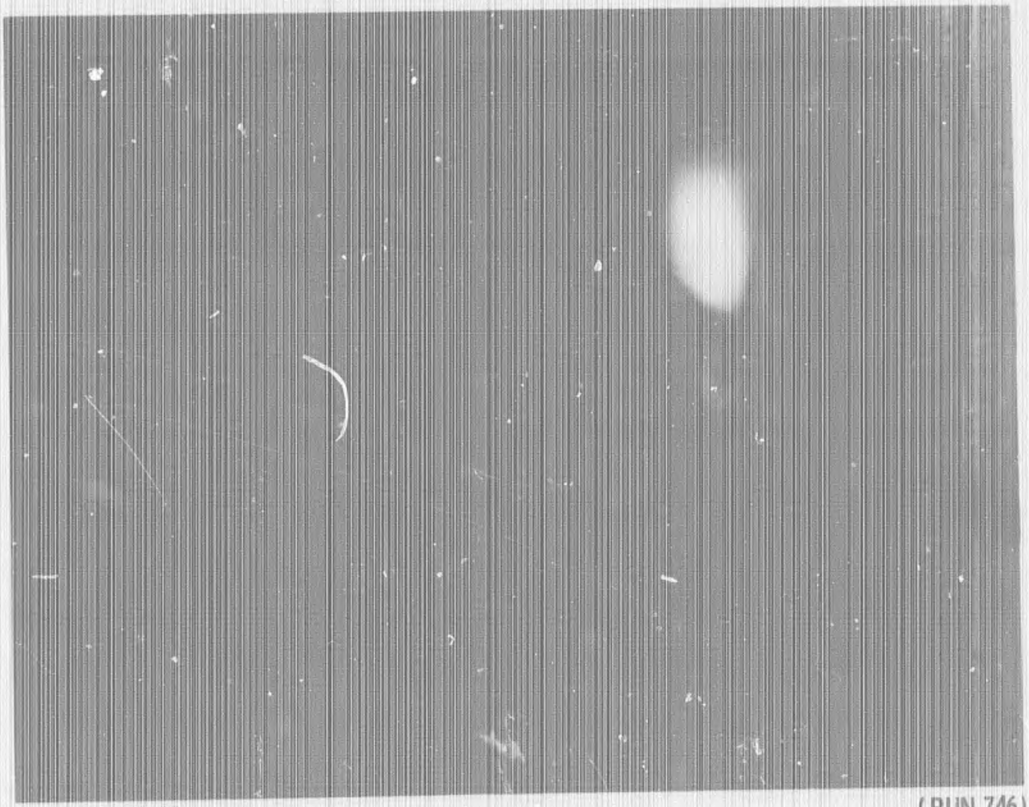

H. $M_s = 4.39$ (RUN 746)

FIG. A-17 TWO-SPARK SHADOW PHOTOGRAPHS OF THE SHOCK INTERACTION FIELD; 9^0 CONE AT 20^0 INCIDENCE ANGLE AT FREE-STREAM MACH 5.1 (CONTINUED)

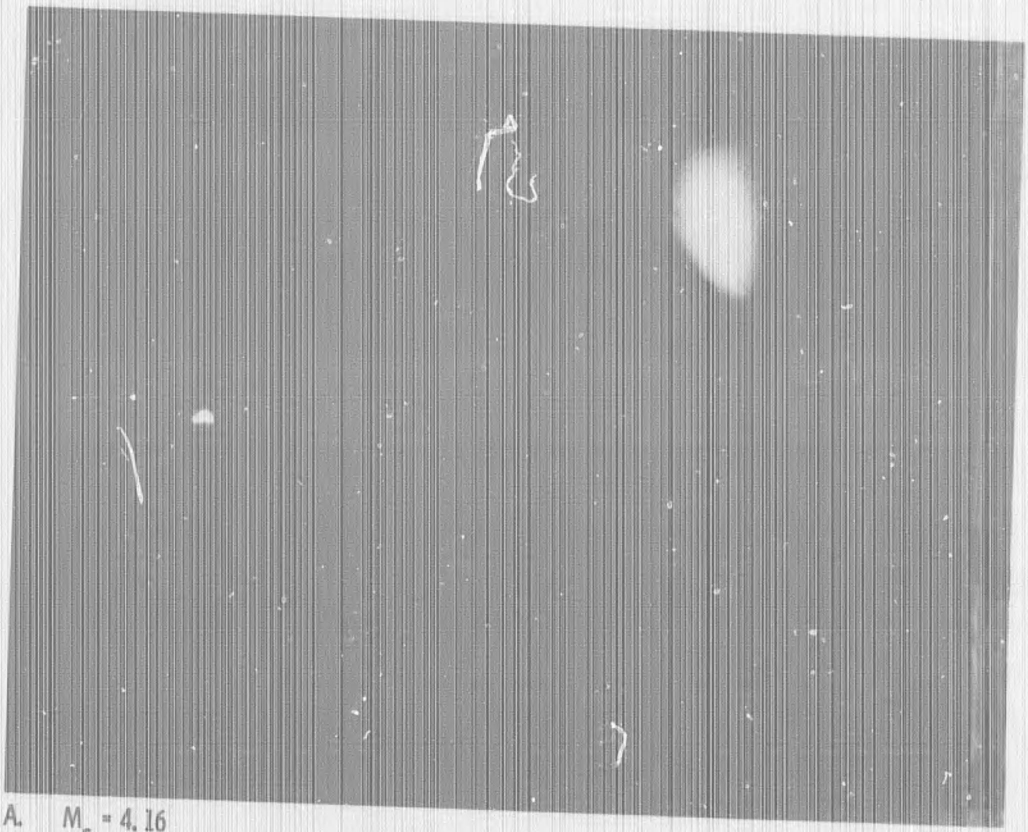

A. $M_s = 4.16$

(RUN 750)

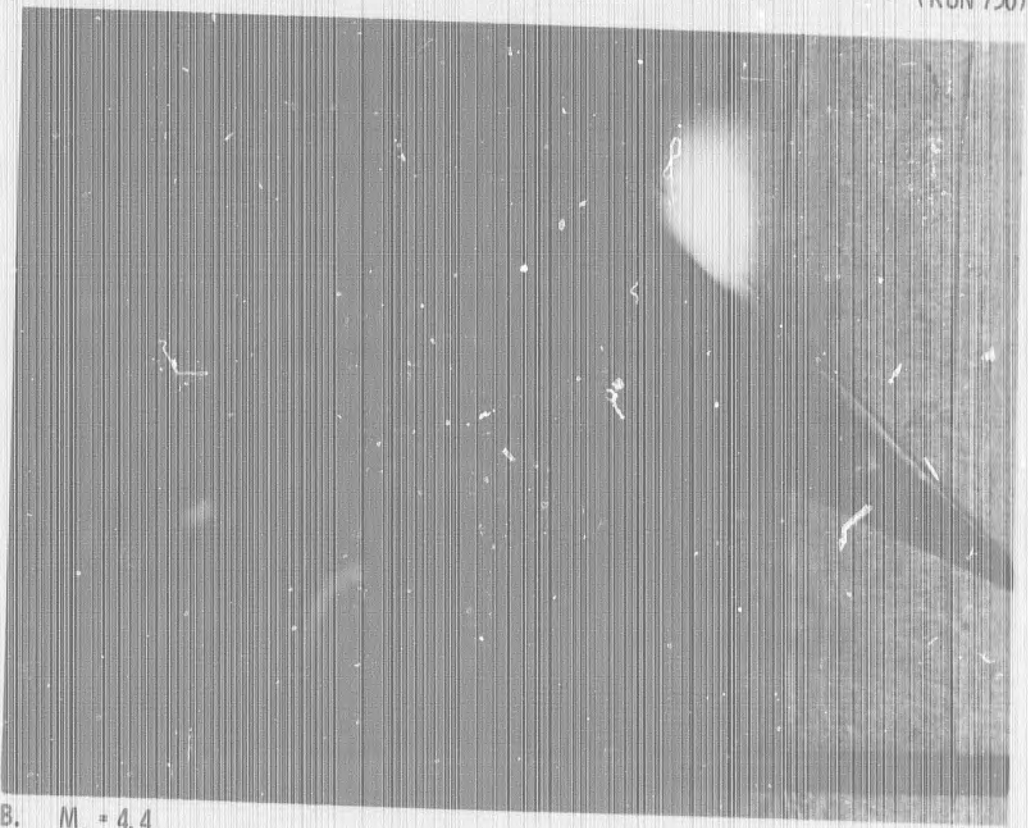

B. $M_s = 4.4$

(RUN 751)

FIG. A-18 TWO-SPARK SHADOW PHOTOGRAPHS OF THE SHOCK INTERACTION FIELD; 9° CONE AT 30° INCIDENCE ANGLE AT FREE-STREAM MACH 5.1

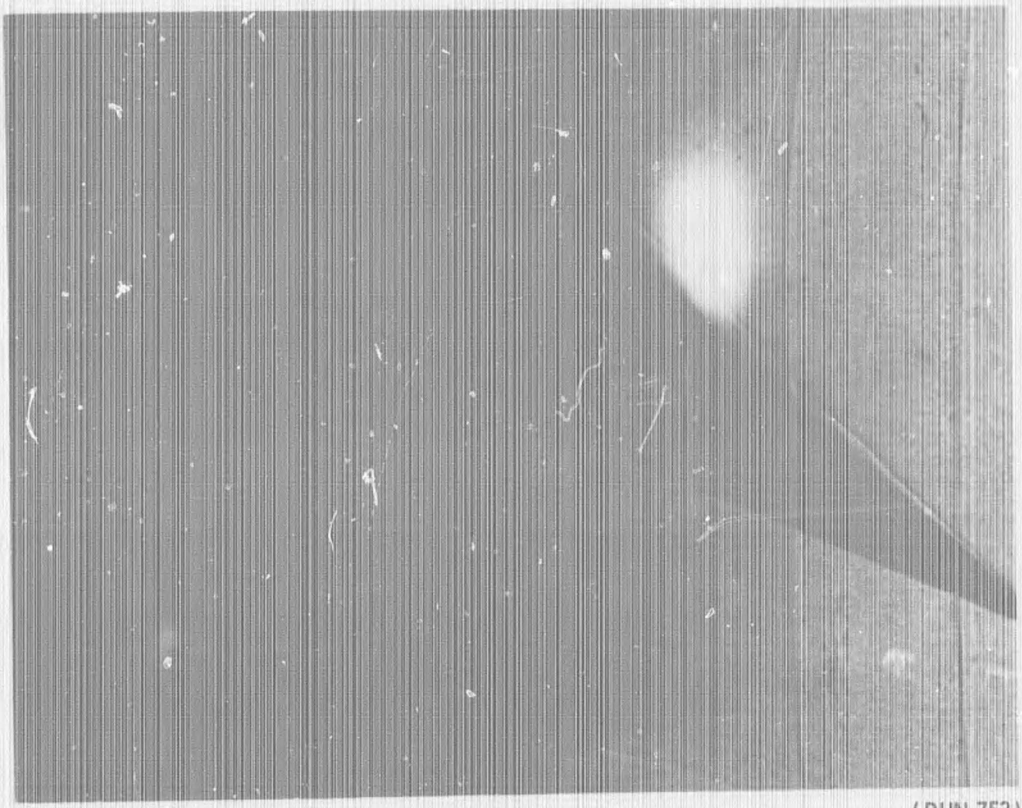

C. $M_s = 4.5$ (RUN 753)

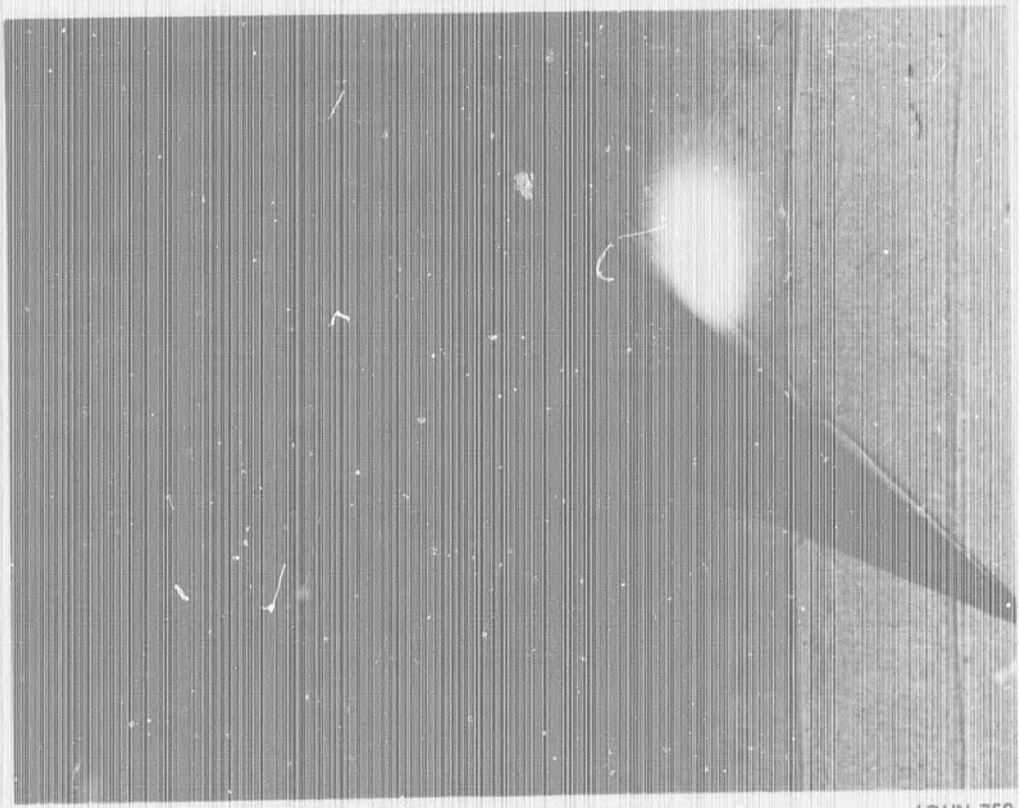

D. $M_s = 4.51$ (RUN 752)

FIG. A-18 TWO-SPARK SHADOW PHOTOGRAPHS OF THE SHOCK INTERACTION FIELD; 9^0 CONE AT 30^0 INCIDENCE ANGLE AT FREE-STREAM MACH 5.1 (CONTINUED)

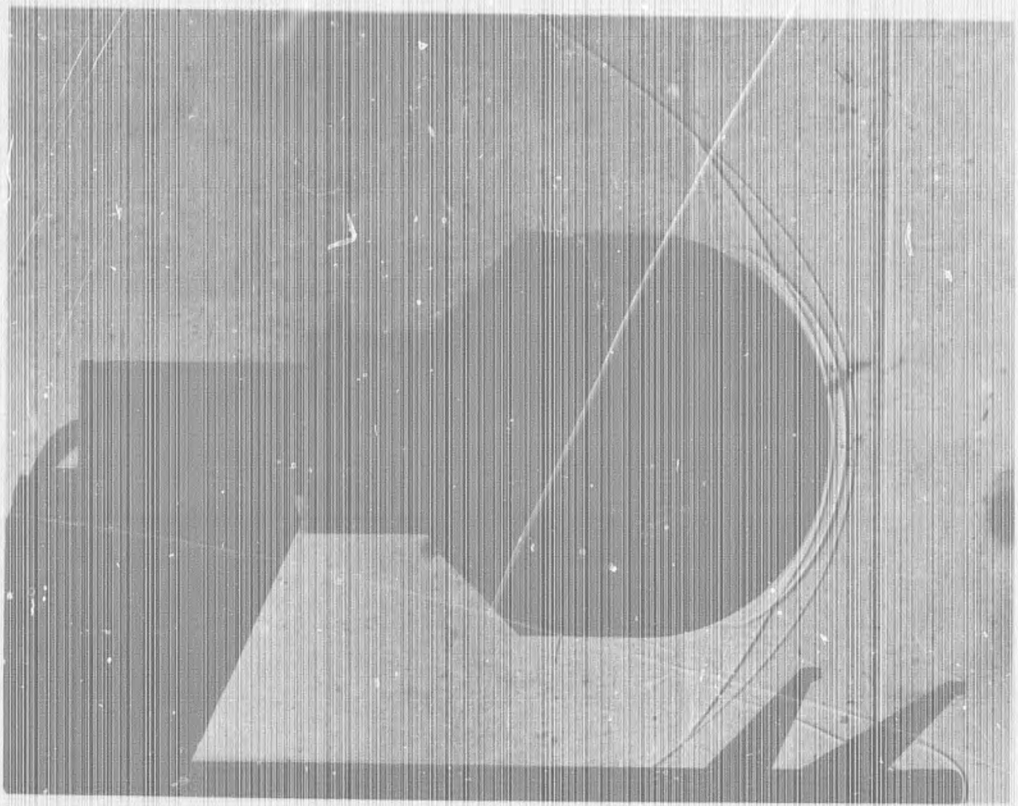

A. $M_1 = 5.07$ $M_s = 2.2$ (RUN 504)

B. $M_1 = 5.07$ $M_s = 2.35$ (RUN 502)

FIG. A-19 TWO-SPARK SHADOW PHOTOGRAPHS OF THE SHOCK INTERACTION FIELD FOR A HEMISPHERE

C. $M_1 = 5.07$ $M_s = 2.5$ (RUN 505)

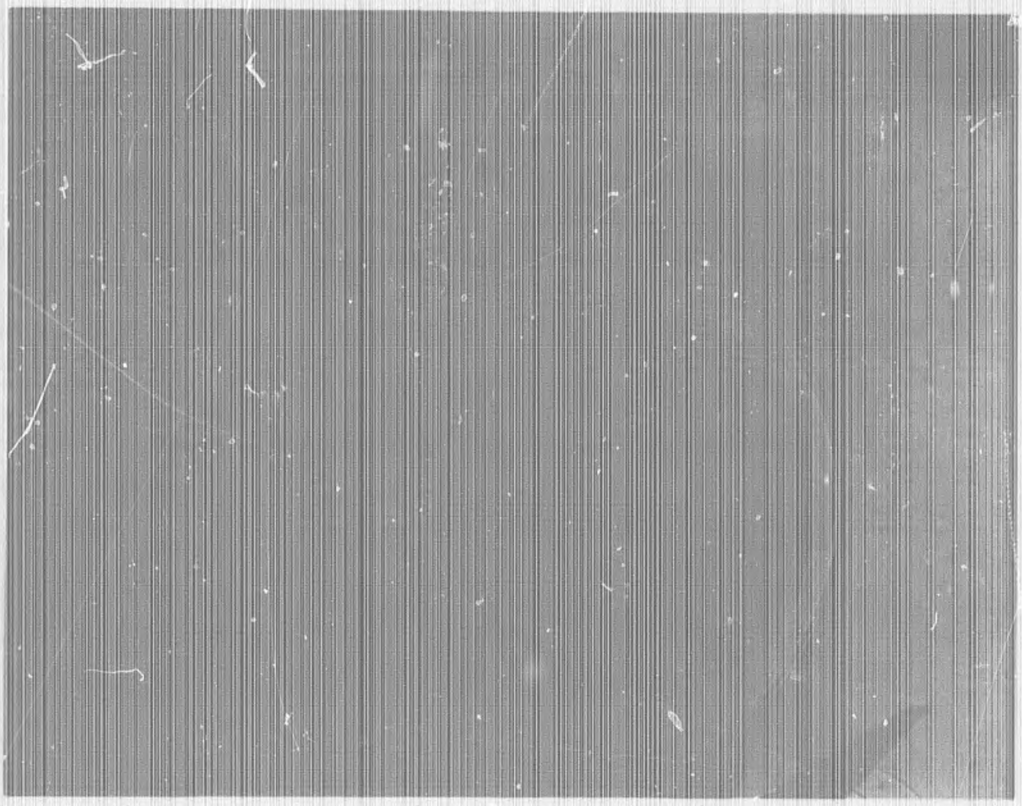

D. $M_1 = 5.07$ $M_s = 2.5$ (RUN 448)

FIG. A-19 TWO-SPARK SHADOW PHOTOGRAPHS OF THE SHOCK INTERACTION FIELD FOR A HEMISPHERE (CONTINUED)

E. $M_1 = 5.07$ $M_s = 3.5$ (RUN 511)

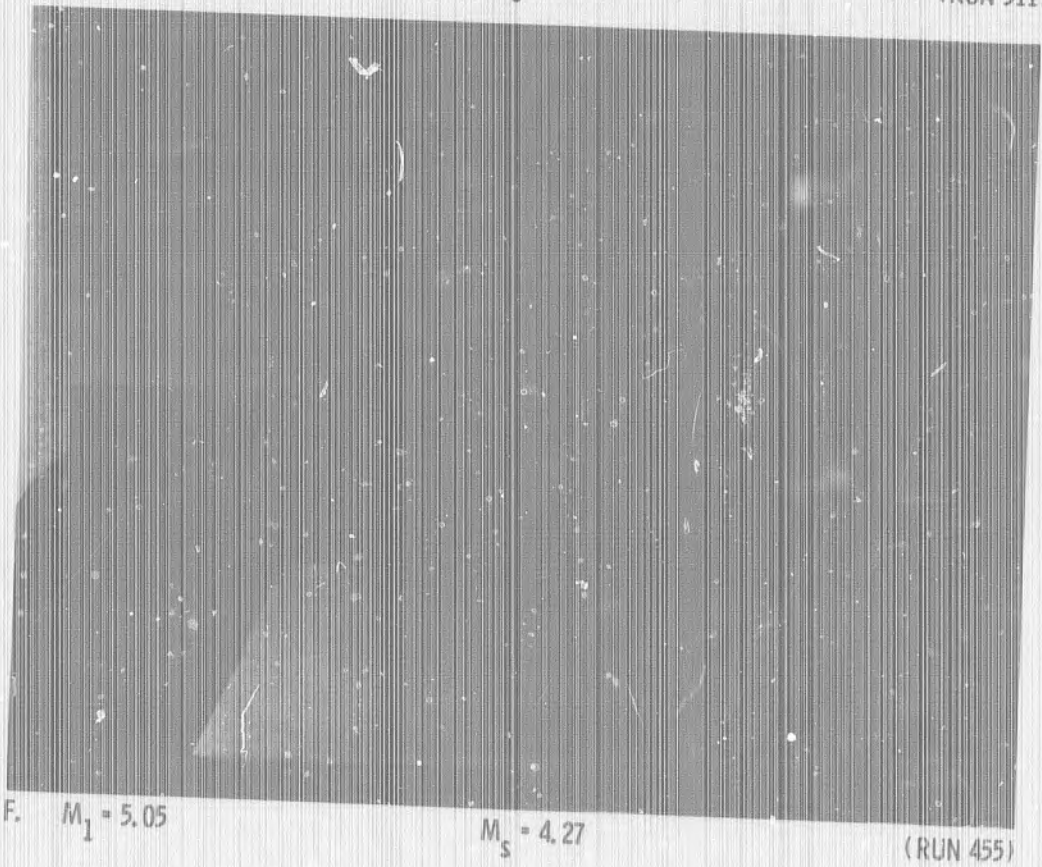

F. $M_1 = 5.05$ $M_s = 4.27$ (RUN 455)

FIG. A-19 TWO-SPARK SHADOW PHOTOGRAPHS OF THE SHOCK INTERACTION FIELD FOR A HEMISPHERE (CONTINUED)

G. $M_1 = 5.05$ $M_s = 4.44$ (RUN 456)

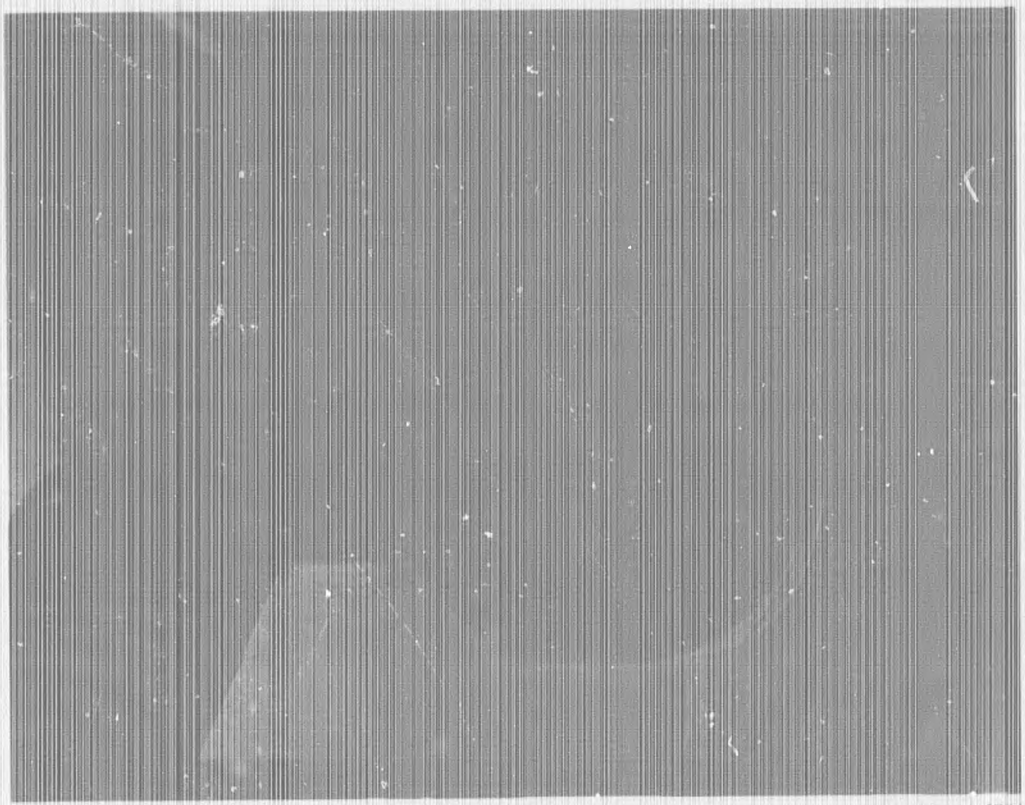

H. $M_1 = 5.05$ $M_s = 4.45$ (RUN 457)

FIG. A-19 TWO-SPARK SHADOW PHOTOGRAPHS OF THE SHOCK INTERACTION. FIELD FOR A HEMISPHERE (CONTINUED)

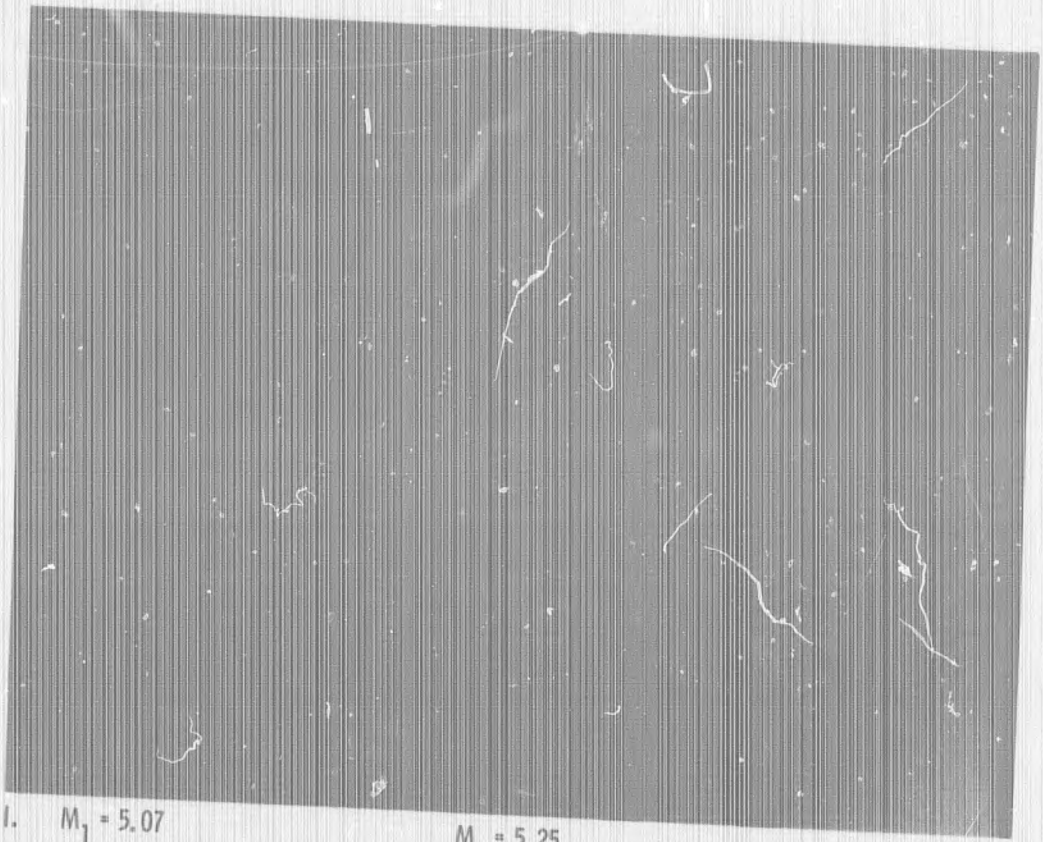

I. $M_1 = 5.07$ $M_s = 5.25$ (RUN 127)

J. $M_1 = 5.07$ $M_s = 5.85$ (RUN 129)

FIG. A-19 TWO-SPARK SHADOW PHOTOGRAPHS OF THE SHOCK INTERACTION FIELD FOR A HEMISPHERE (CONTINUED)

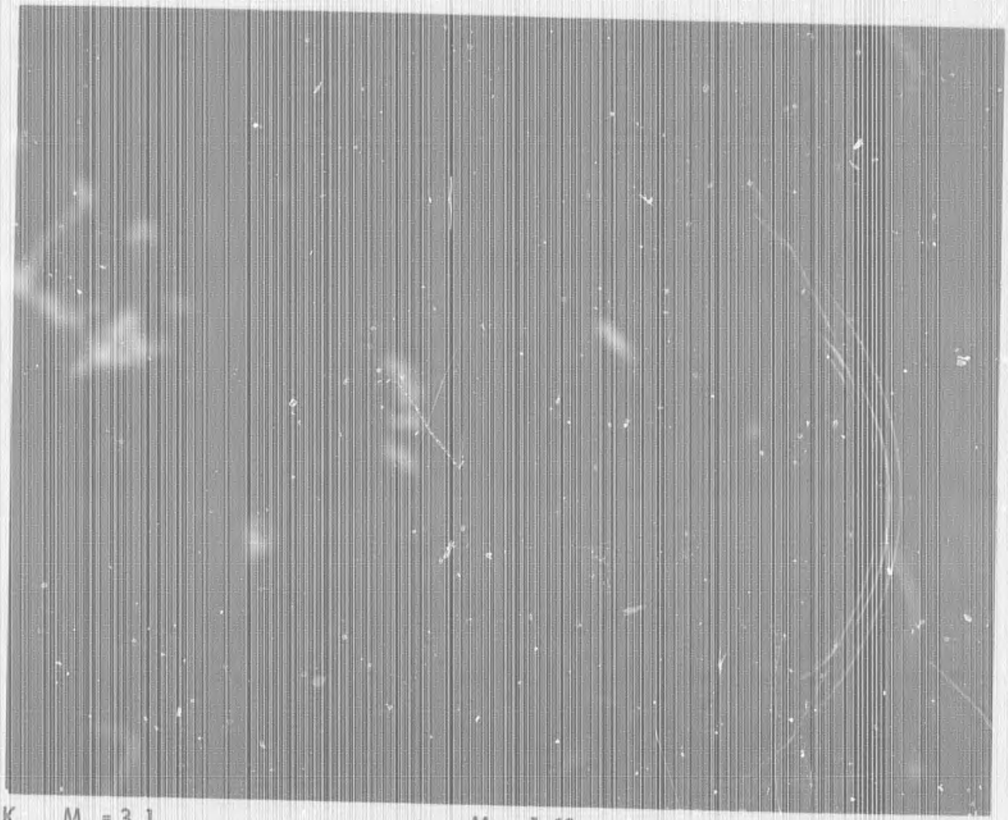

K. $M_1 = 3.1$ $M_s = 1.68$ (RUN 95)

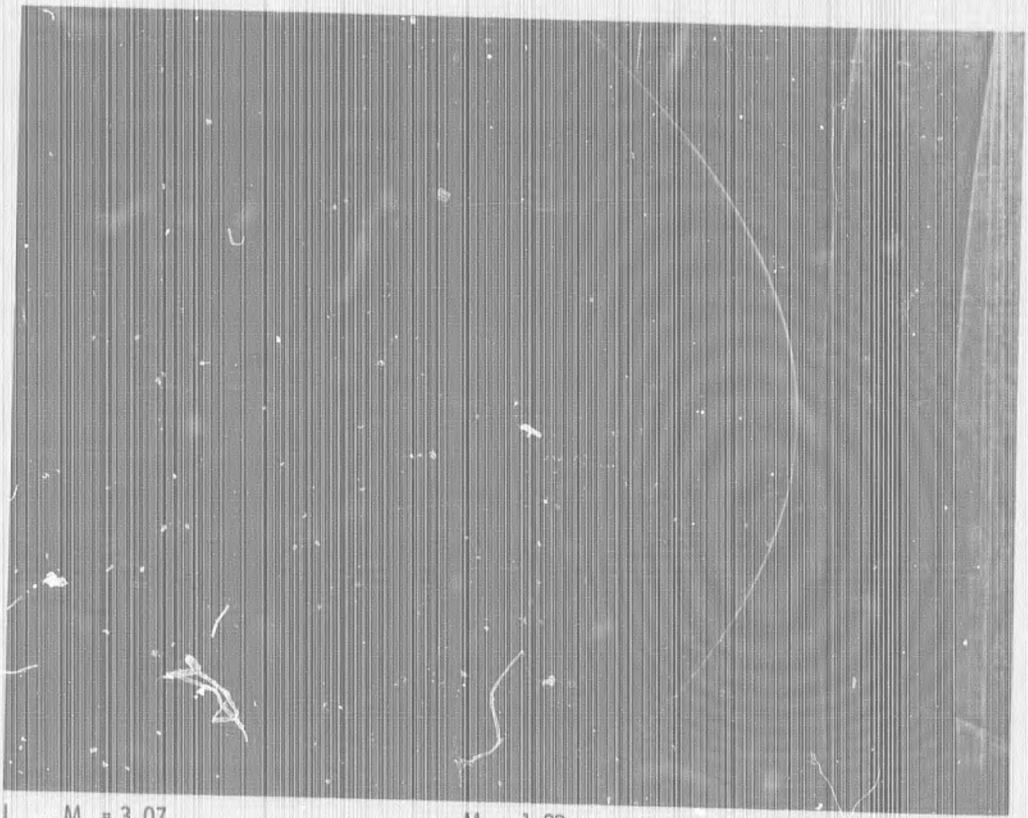

L. $M_1 = 3.07$ $M_s = 1.83$ (RUN 793)

FIG. A-19 TWO-SPARK SHADOW PHOTOGRAPHS OF THE SHOCK INTERACTION FIELD FOR A HEMISPHERE (CONTINUED)

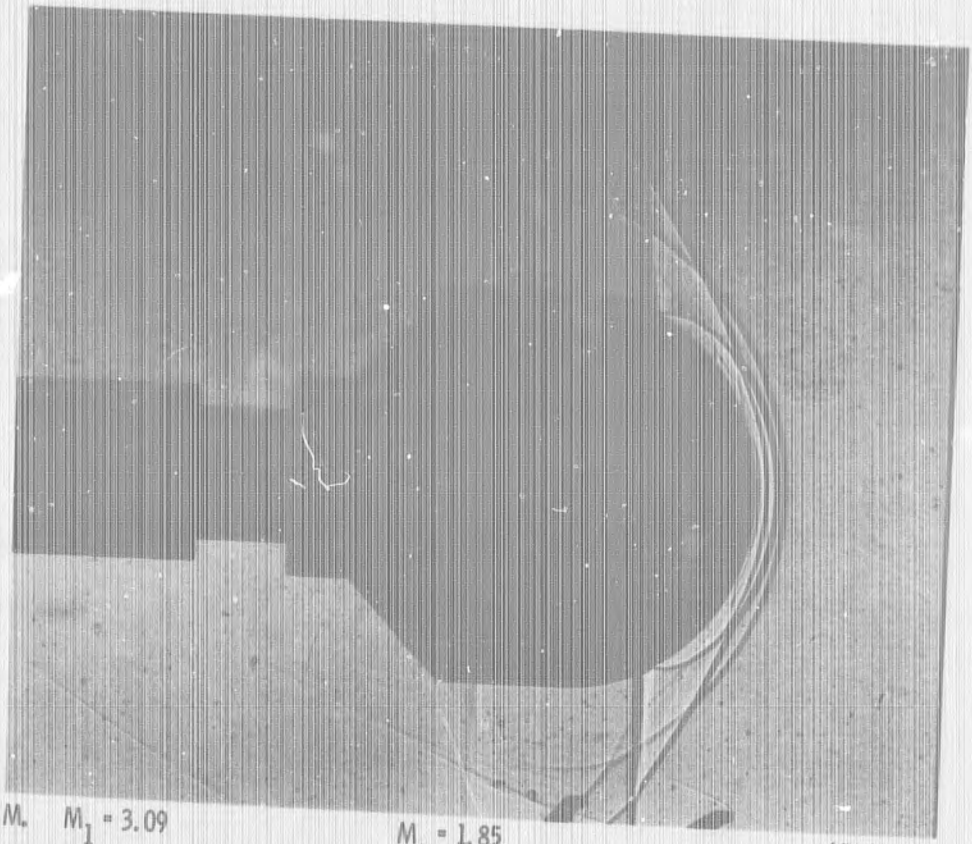

M. $M_1 = 3.09$ $M_s = 1.85$ (RUN 135)

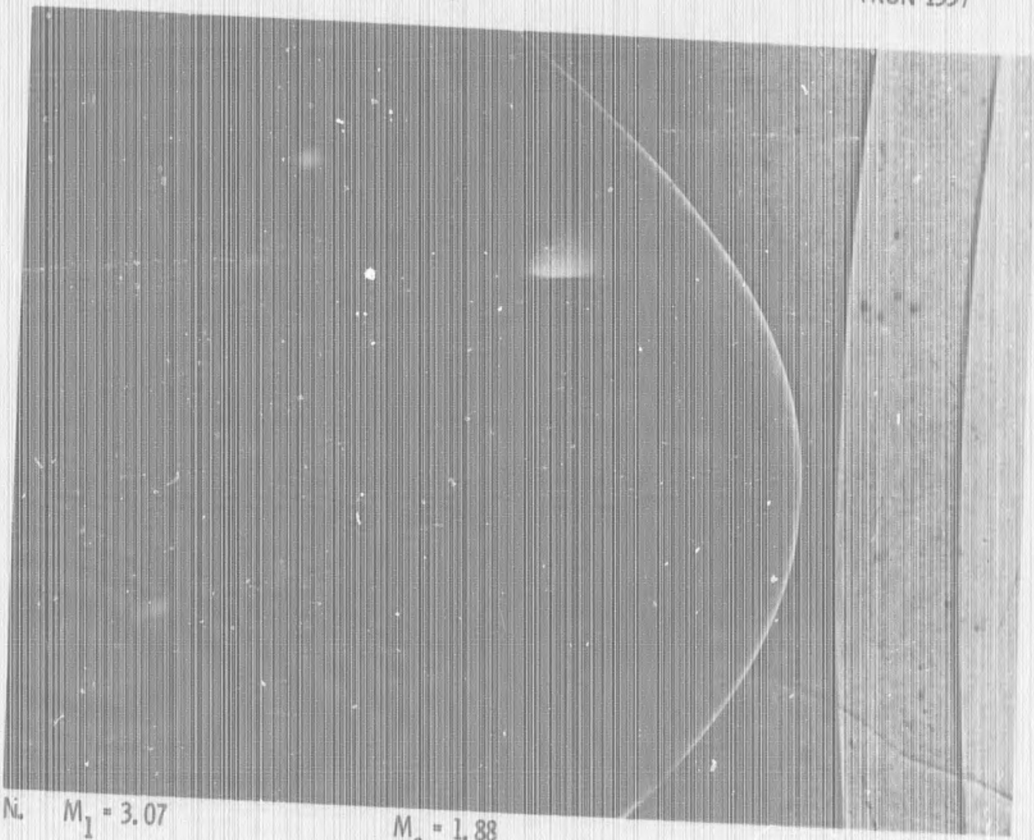

N. $M_1 = 3.07$ $M_s = 1.88$ (RUN 795)

FIG. A-19 TWO-SPARK SHADOW PHOTOGRAPHS OF THE SHOCK INTERACTION FIELD FOR A HEMISPHERE (CONTINUED)

DOCUMENT CONTROL DATA - R & D

(Security classification of title, body of abstract and indexing annotation must be entered when the overall report is classified)

1. ORIGINATING ACTIVITY (Corporate author) Naval Ordnance Laboratory Silver Spring, Maryland 20910	2a. REPORT SECURITY CLASSIFICATION UNCLASSIFIED 2b. GROUP

3. REPORT TITLE

Shock Interaction Surface Pressures for Hemispherical and Conical Bodies

4. DESCRIPTIVE NOTES (Type of report and inclusive dates)

5. AUTHOR(S) (First name, middle initial, last name)

Frank P. Baltakis

6. REPORT DATE 16 February 1971	7a. TOTAL NO. OF PAGES 115	7b. NO. OF REFS 10

8a. CONTRACT OR GRANT NO.	9a. ORIGINATOR'S REPORT NUMBER(S) NOLTR 71-27
b. PROJECT NO.	
c. Task No. NOL 814/DASA (DASA MIPR 528-67 and 504-68) d.	9b. OTHER REPORT NO(S) (Any other numbers that may be assigned this report)

10. DISTRIBUTION STATEMENT

This document is subject to special export controls and each transmittal to foreign governments or foreign national may be made only with prior approval of NOL.

11. SUPPLEMENTARY NOTES	12. SPONSORING MILITARY ACTIVITY Defense Atomic Support Agency

13. ABSTRACT

Transient pressures, induced by wind-tunnel simulated head-on blast wave interactions, have been measured on a hemisphere and on cones of 9-, 15- and 30-degree semivertex angles. Blast wave Mach numbers of 1.6 to 2.2, 2.2 to 5.85 and 2.7 to 4.4 were simulated at the free-stream Mach numbers of 3.1, 5.1 and 7, respectively. Measured pressure-time histories for the hemisphere were compared and found in agreement with histories predicted by McNamara's FLAME code. Peak overpressures for the cones were found to be in agreement with values predicted by a simple theoretical method in which an assumption is made that the blast wave forms a Mach stem moving along the surface at a velocity whose axial component equals the velocity of the main blast wave. The effects of angle of attack and of nose blunting were also investigated with the nine-degree cone at a free-stream Mach number of 5.1.

14 KEY WORDS	LINK A		LINK B		LINK C	
	ROLE	WT	ROLE	WT	ROLE	WT
Shock-on-Shock Interaction						
Transient Pressure						
Cone						
Hemisphere						
Wind Tunnel - Shocktube technique						

DD FORM 1 NOV 65 1473 (BACK)
(PAGE 2)